



INDIUM PARTITIONING BETWEEN FERROMAGNESIAN PHASES AND  
FELSIC MELTS: SIGNIFICANCE FOR ORE FORMATION AND  
EXPLORATION

by

Austin Michael Gion

Thesis submitted to the Faculty of the Graduate School of the  
University of Maryland, College Park, in partial fulfillment  
of the requirements for the degree of  
Masters of Science  
2017

Advisory Committee:

Dr. Philip A. Candela, Professor, Co-Chair

Dr. Philip M. Piccoli, Senior Research Scientist, Co-Chair

Dr. William F. McDonough, Professor

© Copyright by  
Austin Michael Gion  
2017

# Dedication

To Danielle and my family. Thank you for your support.

## Acknowledgements

This work is supported by NSF grant EAR 1348010. I would like to thank the members the Laboratory for Mineral Deposits Research (LMDR) including Dr. Phil Candela, Dr. Phil Piccoli, John Nance, John Hollingsworth, and former members Dr. Brian Tattitch, and Dr. Adam Simon for their support, assistance, and communications throughout the duration of this project. I would also like to thank the Plasma Mass Spectrometry Laboratory at the University of Maryland, which includes Dr. Richard Ash, who assisted with analyses and data interpretation, and Dr. William McDonough, who provided an outside perspective and review of this project. I would also like to acknowledge financial assistance for travel to national and international conferences from the Earth System Science Interdisciplinary Center (ESSIC) at the University of Maryland, the Geological Society of America (GSA), and the Prospectors and Developers Association of Canada (PDAC).

# Table of Contents

Dedication.....	ii
Acknowledgements.....	iii
Table of Contents.....	iv
List of Tables.....	vi
List of Figures.....	vii
Chapter 1: Introduction.....	1
1.1. Motivation.....	1
1.2. Background.....	3
1.2.1. General Characteristics of Magmatic-Hydrothermal Systems.....	5
1.2.2. Porphyry and Vein-Stockwork Deposits.....	9
1.2.3. Volcanogenic Massive Sulfide (VMS) Deposits.....	12
1.2.4. Skarn Deposits.....	13
1.2.5. Epithermal Deposits.....	14
1.2.6. Indium Deposits.....	16
1.3. Hypothesis.....	20
Chapter 2: Experimental Techniques.....	21
2.1. Introduction to Experimental Techniques.....	21
2.2. Cold-Seal Pressure Vessels and Tube Furnaces.....	21
2.3. Experimental Charges.....	22
2.3.1. General Design.....	22
2.3.2. Biotite/Melt Experimental Design.....	26
2.3.3. Amphibole/Melt Partitioning Experimental Design.....	27
2.3.4. Vapor/Melt Partitioning Experimental Design.....	28
2.4. Experimental Controls and Theory.....	28
2.4.1. Fugacity.....	28
2.4.2. Activity of the Annite Component of Biotite.....	30
2.4.3. Activity of the Sanidine Component of Alkali Feldspar.....	32
2.4.4. Activity of the Magnetite Component of Spinel.....	32
2.4.5. Water Fugacity.....	32
2.5. Aluminum Saturation Index (ASI).....	33
Chapter 3: Analytical Techniques.....	33
3.1. Sample Preparation.....	33
3.2. Optical Microscopy.....	34
3.3. Electron Probe Microanalysis (EPMA).....	34
3.4. Laser Ablation Inductively Coupled Plasma Mass Spectrometry (LA-ICP-MS) and Solution Inductively Coupled Plasma Mass Spectrometry (ICP-MS).....	37
3.5. Comparison of EPMA to LA-ICP-MS.....	39
3.6. Data Reduction.....	39
3.6.1. EPMA.....	39
3.6.2. LA-ICP-MS and ICP-MS.....	40
3.6.3. Uncertainty and Propagation of Errors.....	42
Chapter 4: Results.....	44
4.1. Biotite/Melt Experiments.....	44
4.1.1. Diffusion of Indium into Biotite.....	44

4.1.2. Biotite/Melt Partitioning .....	45
4.2. Amphibole/Melt Experiments.....	62
4.3. Vapor/Melt Experiments.....	77
4.4. Indium Silicates .....	78
Chapter 5: Discussion .....	79
5.1. Substitution of Indium into Biotite and Amphibole .....	79
5.2. Effect of Oxygen Fugacity on Biotite Composition .....	81
5.3. Thermodynamics of Indium Partitioning between Biotite and Melt .....	82
5.4. Thermodynamics of Indium Partitioning between Amphibole and Melt .....	84
5.5. Indium Silicates .....	88
5.6. Demonstration of Equilibrium .....	91
5.6.1. Biotite Equilibrium .....	91
5.6.2. Amphibole Equilibrium .....	92
5.7. Disequilibrium in Partitioning Experiments .....	92
5.8. Henry's Law.....	93
5.9. Indium Sequestration Model.....	97
5.10. Exploration Vectors .....	107
Chapter 6: Conclusions .....	112
Appendix A: Co-Pd Oxygen Fugacity Sensors .....	113
Appendix B: Composition of NBS 610 .....	115
Appendix C: EPMA of Starting Materials.....	116
Appendix D: Masses of Experimental Charges .....	119
Appendix E: EPMA of Run Products .....	120
Appendix F: Gauss-Jordan Method for Reduction of Equilibria.....	137
Bibliography .....	145

## List of Tables

Table 1: Partition Coefficients for Indium from Literature .....	19
Table 2: Characterization of Starting Materials.....	25
Table 3: Operating Conditions for EPMA .....	35
Table 4: Standard Used for EPMA .....	35
Table 5: X-ray Lines Used in EPMA.....	36
Table 6: Detection Limits of EPMA.....	37
Table 7: EPMA and LA-ICP-MS Comparison.....	38
Table 8: First Pass EPMA Filter of Analyses .....	40
Table 9: Composition of Biotite/Melt Run Product Glass.....	48
Table 10: Composition of Biotite/Melt Run Product Biotite.....	51
Table 11: Mineral Formulas of Biotite/Melt Run Product Biotite.....	55
Table 12: Partition Coefficients for Biotite/Melt.....	58
Table 13: Composition of Amphibole/Melt Run Product Glass.....	64
Table 14: Composition of Amphibole/Melt Run Product Amphibole.....	66
Table 15: Mineral Formulas of Amphibole/Melt Run Product Amphibole .....	69
Table 16: Partition Coefficients for Amphibole/Melt.....	72
Table 17: Composition and Partition Coefficients for Vapor/Melt .....	77
Table 18: Composition of Experimental In-Silicates.....	78
Table 19: Fictive Oxygen Fugacities .....	81
Table 20: Mass Balance of Indium in Run Products .....	90
Table 21: Parameters Used in Lattice Strain Model .....	95
Table 22: Parameters and Results of Indium Ore Models .....	101
Table B: Composition of NBS 610.....	115
Table C: EPMA of Starting Materials .....	116
Table D: Mass of Starting Materials.....	119
Table E: EPMA of Run Products.....	120
Table F.1: Biotite Phase Components.....	139
Table F.2: Biotite System Components .....	140
Table F.3: Reduced Biotite System Components .....	140
Table F.4: Reduced Biotite Phase Components.....	141
Table F.5: Amphibole Phase Components.....	142
Table F.6: Amphibole System Components .....	143
Table F.7: Reduced Amphibole System Components .....	143
Table F.8: Reduced Amphibole Phase Components.....	144

## List of Figures

Figure 1: World Production of Indium .....	1
Figure 2: World Production and Reserves by Country .....	2
Figure 3: Phase Assemblage for Granodiorite According to Naney (1983).....	7
Figure 4: Cross Section of Magmatic Ore Forming Environment.....	8
Figure 5: Configuration of Biotite and Amphibole Experiments .....	27
Figure 6: Indium vs. $X_{\text{Annite}}^{\text{Bt}}$ .....	59
Figure 7: Biotite/Melt Partition Coefficients vs. $X_{\text{Annite}}^{\text{Bt}}$ .....	59
Figure 8: Indium vs. Silicon of Experimental Biotite.....	60
Figure 9: Biotite/Melt Partition Coefficients vs. Silicon .....	60
Figure 10: Indium vs. Titanium of Experimental Biotite .....	61
Figure 11: Biotite/Melt Partition Coefficients vs. Titanium.....	61
Figure 12: Indium vs. Aluminum of Experimental Amphibole.....	73
Figure 13: Indium vs. Titanium of Experimental Amphibole .....	73
Figure 14: Indium vs. Potassium + Sodium of Experimental Amphibole.....	74
Figure 15: Indium vs. Iron of Experimental Amphibole .....	74
Figure 16: Amphibole/Melt Partition Coefficients vs. Aluminum .....	75
Figure 17: Amphibole/Melt Partition Coefficients vs. Titanium.....	75
Figure 18: Amphibole/Melt Partition Coefficients vs. Potassium + Sodium .....	76
Figure 19: Amphibole/Melt Partition Coefficients vs. Iron.....	76
Figure 20: Vapor/Melt Partition Coefficients vs. Chlorine .....	77
Figure 21: Biotite/Melt Partition Coefficients vs. Oxygen Fugacity .....	82
Figure 22: Residual of Biotite/Melt Partition Coefficients vs. Run Time .....	92
Figure 23: Amphibole/Melt Partition Coefficients vs. Run Time .....	93
Figure 24: Example of Henry's Law Zone .....	94
Figure 25: Biotite Onuma Diagram .....	96
Figure 26: Amphibole Onuma Diagram .....	97
Figure 27: Ternary of Indium Potential .....	107
Figure 28: Relationship of Oxidation and Color Index to Indium-Ore Potential .....	108

# Chapter 1: Introduction

## 1.1. Motivation

Indium, used primarily as indium-tin oxide, is a common element in 21<sup>st</sup> century technologies. The most common technologies that utilize indium-tin oxides are smart phone screens, LCD displays, solar cells, infrared detectors, and alloys. These uses have recently increased the demand (Figure 1), which in turn has increased indium prices. The world indium price was ~\$1,000/ per kilogram in 2005 (U.S. Geological Survey, 2010), which was followed by a series of rises and falls (U.S. Geological Survey, 2016). The average price of indium in 2015 was \$460 per kilogram (U.S. Geological Survey, 2016) and was \$240 in 2016 (U.S. Geological Survey, 2017b). Variability in indium price is directly related to the supply chain.

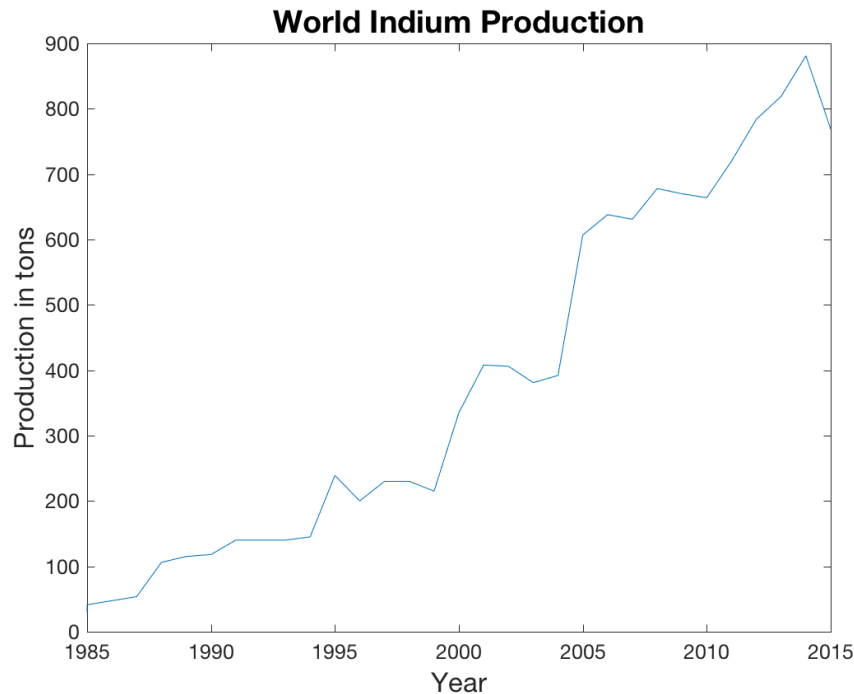


Figure 1: World production of indium by year from 1985 to 2015. Data from U.S. Geological Survey (2017a).

Over 90% of indium production occurs in four countries (Figure 2) (U.S. Geological Survey, 2017b) meaning supply and demand changes in one of these countries can affect world prices. For example, it has been suggested that the drop in indium price after 2015 was a result of the closure of the Fanya Metal Exchange Co. Ltd (China), which increased the supply (U.S. Geological Survey, 2017b). The varying price, lack of stable supply chain, and growing usage within the energy sector all suggest, indicate that over a long-term time scale, indium availability is at risk (Jaffe et al., 2011).

In order to increase supply and minimize supply chain disruptions, an increase in indium exploration is warranted. However, the occurrence of indium in magmatic-hydrothermal ore deposits is poorly understood. Although, indium is known to be associated with sulfides, its behavior in sulfur-poor, felsic magmatic systems is not well understood. Kayser (2013) determined that during crystallization of a melt sequestration of indium by sulfides (pyrrhotite) is insignificant. Therefore, the

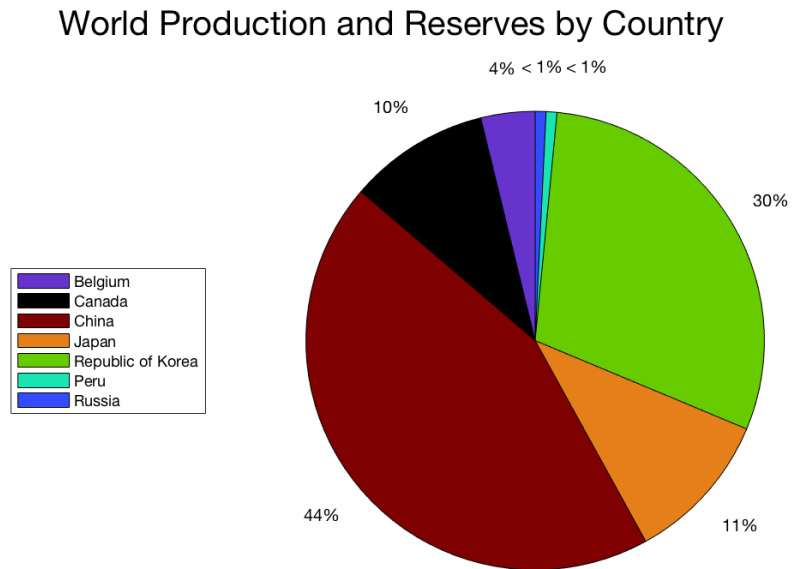


Figure 2: World production and reserves of top indium producing countries. Data from U.S. Geological Survey (2017a).

primary goal of this study is to characterize the behavior of indium in sulfur-poor experimental systems by measuring partition coefficients for the partitioning of indium between ferromagnesian minerals and a felsic melt. For the purposes of this study the partition coefficient is defined as:

$$D_{\text{In}}^{\text{Mineral/Melt}} = \frac{C_{\text{In}}^{\text{Mineral}}}{C_{\text{In}}^{\text{Melt}}}, \quad \text{Eq. (1)}$$

where  $D_{\text{In}}^{\text{Mineral/Melt}}$  is the partition coefficient of indium between mineral and melt,  $C_{\text{In}}^{\text{Mineral}}$  is the concentration (in ppm (ppm is parts per million by weight)) of indium in the mineral (biotite or amphibole), and  $C_{\text{In}}^{\text{Melt}}$  is the concentration (in ppm) of indium in the melt. After determining the partition coefficient for individual phases in a magma, a bulk partition coefficient can be defined as:

$$\bar{D}_i = \sum x_i D_i, \quad \text{Eq. (2)}$$

where  $\bar{D}_i$  is the bulk partition coefficient for phase  $i$ ,  $x_i$  is the mass fraction of phase  $i$ , and  $D_i$  is the partition coefficient between phase  $i$  and melt. The bulk partition coefficient can be used to describe the partitioning behavior of indium during the crystallization of a melt containing multiple coexisting phases. Using this bulk partition coefficient, the behavior of indium can be constrained, creating a knowledge base for indium exploration.

## 1.2. Background

Indium is a rare element within the Earth, having an estimated concentration of 0.05 ppm in the continental crust (Rudnick and Gao, 2003) and 0.01 ppm in bulk silicate Earth (McDonough and Sun, 1995). Additionally, indium is a chalcophile and relatively incompatible during mantle melting (Sun, 1982). Indium is associated

with base metals (zinc, lead, tin, and bismuth) (Schwarz-Schampera and Herzig, 2002), suggesting that deposits enriched in base metals may also be enriched in indium. Due to its affinity for sulfur, minerals such as sphalerite (ZnS), stannite (Cu<sub>2</sub>FeSnS<sub>4</sub>), chalcopyrite (CuFeS<sub>2</sub>), and other base metal sulfides are potential indium ore minerals. Indium rarely is an essential constituent of minerals, but is known to form the sulfides roquesite (CuInS<sub>2</sub>) (Picot and Pierrot, 1963), indite (FeIn<sub>2</sub>S<sub>4</sub>) (Genkin and Murav'eva, 1963), and sakuraiite ((Cu,Fe,Zn)<sub>3</sub>(In,Sn)S<sub>4</sub>) (Ohta, 1989).

Deposits containing significant concentrations of indium (greater than hundreds of ppm) are rare, making indium a secondary target during mining. An exception was the Toyoha epithermal-vein deposit in Japan (closed in 2006), wherein indium was mined along with lead, zinc, copper, and silver (Schwarz-Schampera and Herzig, 2002). Other deposits that are indium-bearing include: sulfide-veins, breccias, and replacement zones at Mount Pleasant, New Brunswick; the Volcanogenic Massive Sulfide (VMS) deposit of Kidd Creek, Ontario; and skarn deposits in Dachang, Gaungxi, China; and the epithermal San Roque deposit of Argentina (Dill et al., 2013; Ishihara et al., 2011a; Schwarz-Schampera and Herzig, 2002; Sinclair et al., 2006). In the majority of deposits, indium is recovered as a byproduct during zinc mining and refining (Tolcin, 2016). Indium recovered post mining is leached from slag, residue, and alloys produced during smelting by hydrochloric or sulfuric acid (Stevens and White, 1990).

Currently, the model for the formation of indium-bearing deposits is incomplete; however, there are models for the formation of base-metal deposits that

contain elevated indium concentrations. These deposits include porphyry, vein-stockwork, VMS, skarn, and epithermal types. What follows are summaries of existing models for each deposit type.

### *1.2.1. General Characteristics of Magmatic-Hydrothermal Systems*

Magmatic-hydrothermal ore deposits are commonly associated with shallow, water-rich, felsic magmas (Candela and Holland, 1986; Candela and Piccoli, 2005; Hedenquist and Lowenstern, 1994). Felsic magmas can be sourced from a variety of domains including partial melts of mantle material, subducting slabs, and/or the crust (Candela and Piccoli, 2005; Hedenquist and Lowenstern, 1994). Likewise, ore metals are sourced from the same regions as the felsic magma (Hedenquist and Lowenstern, 1994). The metals are transported and concentrated via an ore-forming fluid, known as the magmatic volatile phase (MVP), which can be a supercritical gas, vapor, or brine (Candela and Piccoli, 2005). Whether the MVP is a vapor or brine is dependent on the Cl/H<sub>2</sub>O ratio (Candela, 1989b; Webster, 2004; Webster et al., 1999). The formation of the MVP is a function of the volatile content of the melt. The mass of volatiles needed to saturate the melt is a function of the pressure and temperature conditions during ascent and emplacement, as well as the composition of the melt phase; generally, the deeper the level of emplacement the higher the solubility of water (Candela and Holland, 1986).

During ascent through the crust the magma decompresses, cools, and is emplaced. The MVP can exsolve from the melt portion of the magma by decompression, crystallization, or both of these processes, where decompression-driven boiling is termed first boiling and crystallization-driven boiling is termed

second boiling (Bowen, 1928). Emplacement of ore related magmas generally occurs between 4-10 km (Annen et al., 2006). At an emplacement depth of ~4 km, the pressure is on the order of 100 MPa. For a rhyolitic melt, these pressures result in a water solubility of ~4 wt%, assuming there is insignificant concentrations of CO<sub>2</sub> ( $\leq 1$  ppm), F (<1000 ppm), or Li (<1%) in the melt (Dingwell et al., 1997; Holtz et al., 1993; Papale et al., 2006; Yamashita, 1999). The addition of CO<sub>2</sub> (ppm level or greater) to the melt will result in volatile saturation at lower water contents (for example see Candela (1997) and Papale et al. (2006)). Opposite the effect of CO<sub>2</sub> is the effect of F or Li. Both F and Li will increase the solubility of water (Dingwell et al., 1997; Holtz et al., 1993), as well as lower liquidus temperatures (Manning, 1981; Martin, 1983). Interestingly, the water solubility reaches a minimum in slightly peraluminous melts (ASI = ~1.1) (Dingwell et al., 1997), where ASI is the Aluminum Saturation Index defined as the ratio of molar Al<sub>2</sub>O<sub>3</sub> to K<sub>2</sub>O + Na<sub>2</sub>O + CaO. For granitic melts at 800°C and 100 MPa this minimum is ~2.9 wt% and will increase as melts become more peralkaline or peraluminous (Dingwell et al., 1984).

Dominantly anhydrous crystallization of a melt prior to volatile saturation concentrates volatiles in the remaining melt. For example, at 200 MPa and 800°C, a felsic melt will saturate with volatiles at ~6 wt% water (Papale et al., 2006). If this melt has an initial volatile content of 4 wt% water, one-third of the melt, assuming all crystallization products are anhydrous, will need to crystallize for volatile saturation to be reached. If hydrous phases crystallize, the amount of crystallization needed to reach volatile saturation will increase.

The crystallization products of a melt are determined by the water content, temperature, and the concentration of anhydrous components of the melt. Naney (1983) determined phase relations, described below, and volatile saturation for a granite and granodiorite at 200 and 800 MPa (Figure 3). For example, a granodiorite melt at 200 MPa with 4 wt% water begins to crystallize at ~1000°C and reaches

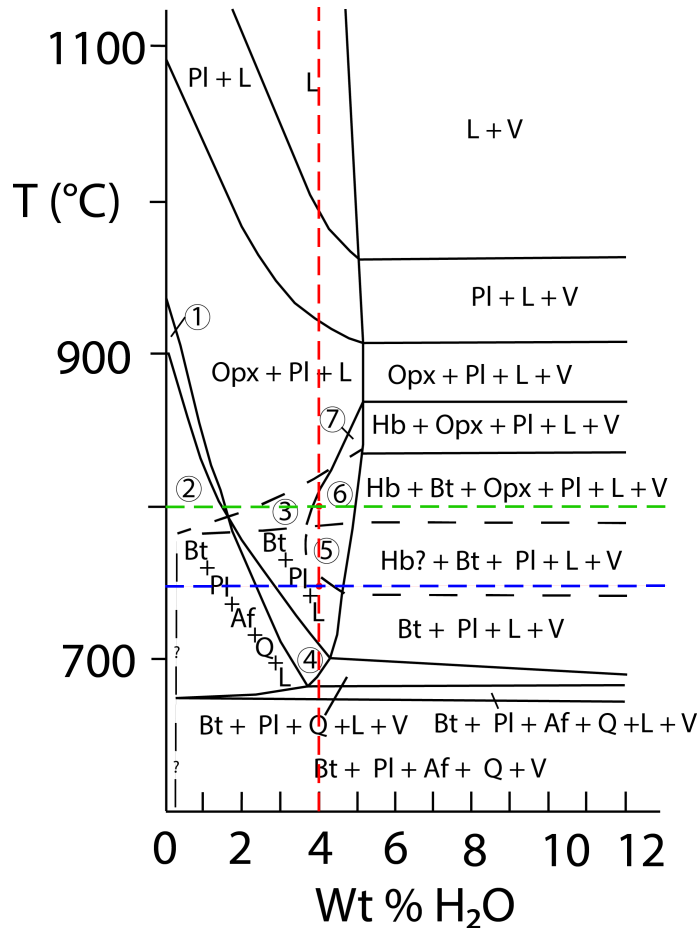


Figure 3: Phase relations for synthetic granodiorite as a function of temperature and water concentration at 200 MPa modified from Naney (1983). Red dashed line indicates 4 wt% H<sub>2</sub>O, blue dashed line indicates temperature of biotite experiments, green dashed line indicates amphibole experiments performed as part of this work. Black dashed line indicates uncertainty in the position of the stability limits for a phase assemblage.

Numbered assemblages are:

1. Opx + Pl + Af + L
2. Opx + Pl + Af + Q + L
3. Opx + Bt + Pl + L
4. Bt + Pl + Q + L
5. Hb(?) + Bt + Pl + L
6. Hb + Bt + Opx + Pl + L
7. Hb + Opx + Pl + L

Opx = orthopyroxene  
 Bt = biotite  
 Af = alkali feldspar  
 L = silicate liquid

Pl = plagioclase  
 Hb = hornblende  
 Q = quartz  
 V = aqueous vapor

volatile saturation at  $\sim 700^{\circ}\text{C}$ . The crystallization sequence of this melt will be as follows: plagioclase, orthopyroxene, followed by hornblende and biotite together. Once hornblende is stable, the orthopyroxene will begin to convert to hornblende and hornblende crystallization will be second to biotite crystallization. At  $\sim 750^{\circ}\text{C}$  hornblende will be a minor phase and crystallization products will contain mostly plagioclase and biotite. At temperatures of  $\sim 700^{\circ}\text{C}$  quartz will begin to crystallize. After volatile saturation and below  $700^{\circ}\text{C}$  alkali feldspar will stabilize and the magma will contain a coexisting volatile phase.

As the melt reaches volatile saturation and the MVP nucleates and grows, ore-related elements remaining in the melt (those that are incompatible in the crystal phases) may partition into the MVP and become available for ore formation. If the

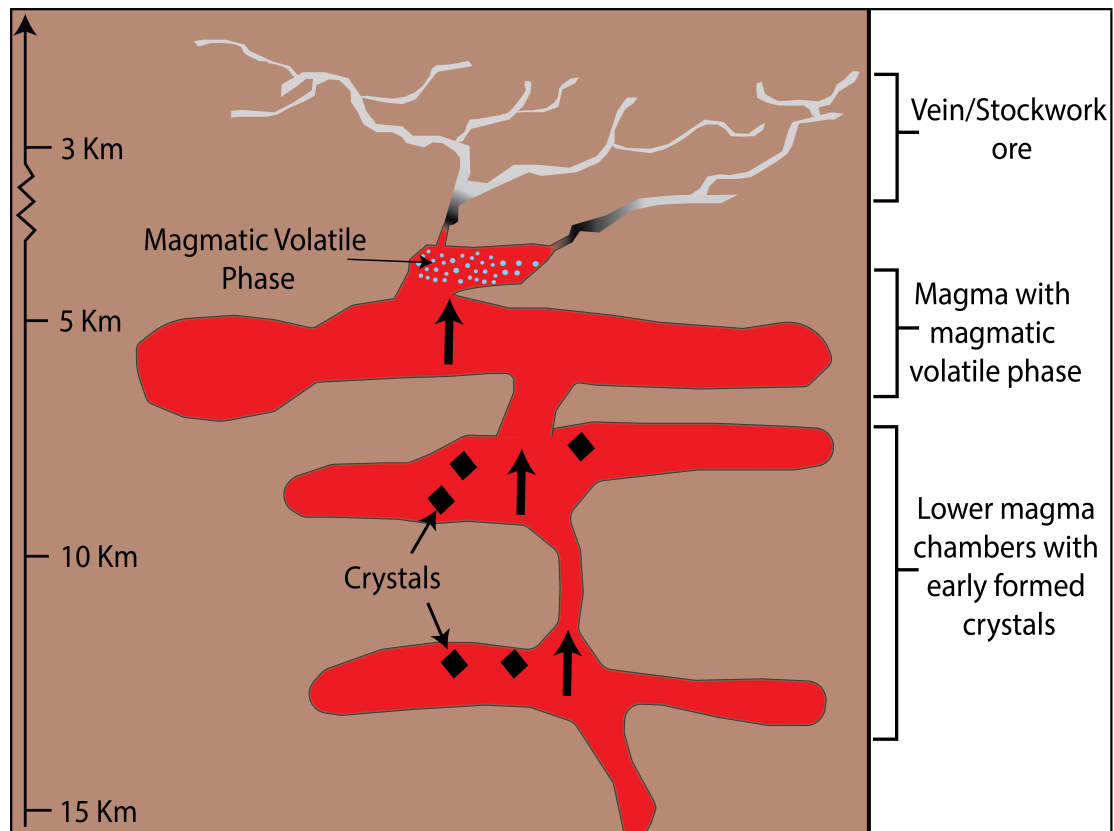


Figure 4: Cross section showing a general magmatic ore-forming environment. Arrows indicate magma rising through the chamber. The magma partially crystallizes until water saturation, at which point a magmatic volatile phase forms.

compatible elements enter the crystalline phases prior to MVP formation, they are sequestered and may be unavailable for ore formation. The proportion of the elements sequestered depends on the phases present, the mass fraction of those phases, and the  $D_i^{\text{Mineral/Melt}}$ . The magnitude of partitioning between vapor and melt can depend significantly on the amount of CO<sub>2</sub>, Cl, S, and H<sub>2</sub>O in the volatile and melt (Candela and Holland, 1984; Candela and Piccoli, 2005; Frank et al., 2011; Hedenquist and Lowenstern, 1994; Holland, 1972; Simon et al., 2005; Tattitch et al., 2015; Zajacz et al., 2011). Various ligands allow for speciation and complexing of metals, and thus transport via the ore fluid. For a general cross section of a magmatic ore-forming environment depicting the processes described above see Figure 4.

#### *1.2.2. Porphyry and Vein-Stockwork Deposits*

Arc-related magmatism is associated with a range of porphyry deposits including the porphyry copper and porphyry molybdenum variants. Porphyry deposits are genetically related to vein-stockwork deposits, generally showing a gradational relationship from porphyry to vein-stockworks (Sinclair, 1996). During subduction, the down-going plate releases volatiles into the overlying mantle wedge causing partial melting and the formation of magma. Partial melting may also occur in the subducting slab, or in the lower and upper crust. The partial melts can also act as a source for metals, such as Cu, Mo, Sn, and W (Sillitoe, 2010), and ligands such as chlorine (Candela and Piccoli, 2005). The partial melts originate at a depth of 15-20 km and are volatile-undersaturated (Sinclair, 1996; Strong, 1981), which are ultimately emplaced at depths of 5 to 15 km (Sillitoe, 2010) to as shallow as 0.6 to 3 km (White et al., 1981). Upon volatile saturation, ore bearing MVP can exsolve from

the melt and localize near the roof of the magma chamber being sporadically released into the overlying country rock (Sillitoe, 2010). The style of mineralization varies as a function of fluid pressure and the confining pressure of the overburden rock.

Sinclair (1996) states four possible scenarios: low confining pressure, resulting in vein deposits along existing fractures; high confining pressure and high fluid pressure, resulting in a stockwork with veins; high confining pressure with low fluid pressure, resulting a marginal pegmatite and greisen; and high fluid pressure, resulting in explosive fracturing and formation of brecciated pipes.

Porphyry deposits form as a result of arc magmatism or extensional/rifting, but differ in source material, metals, and volatiles. Of particular interest to this study is the formation of Climax-type porphyry molybdenum deposits, which will be compared to porphyry copper deposits. Climax-type deposits are associated with high-silica, alkali-rich rhyolites that contain fluorine-bearing phases, such as topaz, apatite, fluorite, and F-enriched biotite (White et al., 1981). The ore mineralogy of Climax deposits consists of quartz-molybdenite veins, wolframite (var. hübnerite), cassiterite, stannite, and rare chalcopyrite (White et al., 1981). Porphyry copper deposits are often associated with calc-alkaline felsic magmas with ore mineralogy most commonly consisting of chalcopyrite and bornite (Sillitoe, 2010). Porphyry copper deposits generally form coeval with subduction (Sillitoe, 2010) and Climax-type deposits form post-subduction in rift-type environments (Audétat and Li, 2017; Sinclair, 2007; White et al., 1981). Porphyry copper deposits are invariably associated with I-type granite (*sensu lato (s.l.)*) suites (Sillitoe, 2010), that is, those with igneous source materials (Chappell and White, 1974), that are undifferentiated

(Westra and Keith, 1981). Climax-type deposits have source material similar to A-type granite (*s.l.*) suites (Collins et al., 1982; Whalen et al., 1987) and are highly differentiated (Westra and Keith, 1981). Volatiles play a vital role in the formation of copper or molybdenum deposits: Candela (1989a) suggests that the ratio of initial water in the melt to the amount of water in the melt at water saturation  $\left(\frac{C_{H_2O}^{\circ}}{C_{H_2O}^s}\right)$  affects the potential ore budget of a copper or molybdenum deposit. A high  $\frac{C_{H_2O}^{\circ}}{C_{H_2O}^s}$  would result in early water saturation and formation of a MVP. Early volatile saturation would prevent copper, considered compatible, from being sequestered into crystalline phases resulting in a high copper content in the MVP and formation of a porphyry copper deposit (Candela, 1989a). Conversely, a low  $\frac{C_{H_2O}^{\circ}}{C_{H_2O}^s}$  would result in late stage MVP formation, the sequestration of a significant proportion of the copper initially present in the melt, and a higher concentration of molybdenum in the MVP resulting in the formation of a molybdenum-rich deposit (Candela, 1989a). A low  $\frac{C_{H_2O}^{\circ}}{C_{H_2O}^s}$  may be the result of a previously melted source material (Burt et al., 1982) or a source rock that has been dehydrated during metamorphism (Holloway, 1977) resulting in a dryer melt (Candela, 1989a). Water saturation can be further delayed by the presence of fluorine in the melt, which increases water solubility (Holtz et al., 1993), furthering the sequestration of Cu relative to Mo. Furthermore, if the deposit displays a high F/H<sub>2</sub>O ratio and low copper grades, as Climax deposits do, the oxidation state of the system may control the Mo/W ratio (Candela, 1989a). A more oxidized system will have a higher Mo/W ratio, whereas a reduced system will have a lower Mo/W ratio

(favoring the enrichment of W) (Candela, 1989a). The presence of Sn in reduced systems may be explained in a similar manner if  $\text{Sn}^{2+}$  behaves incompatibly compared to  $\text{Sn}^{4+}$  (Ague and Brimhall, 1988; Candela, 1989a; Taylor and Wall, 1992)

### 1.2.3. Volcanogenic Massive Sulfide (VMS) Deposits

Volcanogenic Massive Sulfide (VMS) deposits are large, polymetallic lens-shaped deposits containing >40% sulfides and are hosted in volcanic or sedimentary rocks (Franklin et al., 2005; Galley et al., 2007). VMS deposits are major sources of Zn, Cu, Pb, Ag, and Au with various trace elements including Sn, In, Te, Ga, Ge, and Co (Franklin et al., 2005; Galley et al., 2007). VMS deposits form on or under the seafloor during rifting or extensional episodes in an overall arc environment (Galley et al., 2007). Rifting in an arc environment occurs during slab rollback, mantle plume development, and back-arc extension (Franklin et al., 2005). During extension, magma from the mantle or partial melts of crust rise to within 12 km of the surface and act as a heat source driving the formation of the deposit (Franklin et al., 2005). As seawater descends through ocean sediments and into the volcanic stratigraphy, it is heated in a reaction zone, which strips metals from the surrounding rock, and then rises (Franklin et al., 2005). Faults and other fractures create pathways, which can focus metal-bearing waters and cause sulfides to precipitate on the seafloor in a cycle of chimney growth and collapse and/or by subseafloor replacement (Galley et al., 2007). Precipitation of sulfides occurs at temperatures of 300 to 400°C (Franklin et al., 2005). During the growth of the orebody, zone refining occurs through remobilization of ore minerals and results in two distinct ore zones: an inner chalcopyrite zone and an outer sphalerite zone (Franklin et al., 2005; Galley et al.,

2007). The size of the orebody is a function of the permeability of the host rock and the duration of the heat source (Barrie and Hannington, 1999). Deposits that are permeable (due to the presence of a clastic/turbidite component) and long-term heat sources are generally larger (Barrie and Hannington, 1999). Although the reaction zone between the ore body and the magma chamber is the main source of ore metals, it has been suggested that the magma body can act as a source of metals and sulfur, similar to porphyry copper systems (Franklin et al., 2005).

There are a multitude of VMS deposit types, each varying in metal content and host rocks. More recent classifications of VMS deposits have been restricted to classifying deposits solely based on host rocks. Barrie and Hannington (1999) defined five types of VMS deposits: mafic, bimodal-mafic, mafic-siliciclastic, bimodal-felsic, and bimodal-siliciclastic. The classifications are determined based on the proportions of mafic, felsic, and siliciclastic components, such that mafic types are >75% mafic, <1% felsic, and <10% siliciclastic or ultramafic components; bimodal-mafic types are >50% mafic and >3% felsic components; mafic-siliclastic types are equal proportions of mafic and siliciclastic with minor felsic components; bimodal-felsic types are >50% felsic, <15% siliciclastic, and the remainder mafic components; and bimodal-siliciclastic types are equal proportions of volcanic (felsic>mafic) and siliclastic components (Barrie and Hannington, 1999).

#### *1.2.4. Skarn Deposits*

Skarn deposits form as a result of high degrees of alteration due to interactions of fluid and rock (Meinert et al., 2005). The term skarn is most commonly associated with deposits hosted in carbonate rocks, such as limestone or marble; however, skarns

can occur over a variety of rock types (Meinert et al., 2005). The term skarn more accurately describes the mineralogy associated with alteration resulting in calc-silicate minerals, such as garnet and pyroxene (Meinert et al., 2005). The term was first used as such by Törnebohm (1875) to describe a deposit not associated with limestone (Meinert et al., 2005). The gangue mineralogy of skarn deposits includes zonation of proximal garnet, distal pyroxene, and a pyroxenoid, wing ore mineralogy including magnetite, cassiterite, chalcopyrite, and other oxides and sulfides (Meinert, 1995; Meinert et al., 2005). The fluids responsible for the metasomatism of the protolith, as well as carrying ore metals, can be meteoric, marine, metamorphic or magmatic, with the latter being the most prominent and resulting in larger deposits (Meinert et al., 2005). Meinert (1995) described seven types of skarn deposit, Au, Cu, Zn, W, Mo, and Sn, which form as a function of tectonic setting, magma type, oxidation state, and trace element chemistry. Skarns that occur in arc or volcanic settings are Fe, Au, Cu, and Zn have I-type magma signatures, conversely W, Mo, and Sn skarns occur in intraplate or extensional settings and have S- or A- type signatures (Meinert, 1995). Of the seven types listed above, in order from Fe to Sn, Fe skarns are the most primitive and Sn skarns are the most evolved (Meinert, 1995). Meinert (1995) states that, along the spectrum of primitive to evolved skarns, MgO decreases and ASI, SiO<sub>2</sub>, and K<sub>2</sub>O increase. Along with these characteristics, Au and Sn skarns are reduced and Cu, Zn, and Mo skarns are oxidized (Meinert, 1995).

#### *1.2.5. Epithermal Deposits*

Epithermal deposits form in high-temperature shallow systems, such as volcanic arcs and geothermal sites (Simmons et al., 2005). Generally, these deposits

form between 50 and 1500 m below the water table as both magmatic and subvolcanically heated meteoric water interact with host rocks causing extensive alteration and the deposition of ore minerals at temperatures of 150° to 300°C (Simmons et al., 2005). There are a variety of classifications of epithermal deposits (see Simmons et al. (2005) and references therein for complete listing), but perhaps the most common is the division of high-sulfidation and low-sulfidation deposits (Sillitoe, 1993). High-sulfidation deposits are defined by the following characteristics: minerals with high sulfur to metal ratios, advanced argillic alteration, oxidized fluids, abundant sulfides, association with andesitic to rhyolitic rocks, and are subduction related (Sillitoe, 1993). In contrast, low-sulfidation deposits have low sulfidation minerals, intermediate argillic or sericitic alteration, reduced fluid, and form in extensional terrains that are post subduction (Sillitoe, 1993). Low-sulfidation deposits can be divided into 3 subgroups: sulfide poor associated with subalkalic rocks, sulfide base metal rich associated with subalkalic rocks, and sulfide poor associated with alkali rocks (Sillitoe, 1993). The high sulfidation deposits and some low sulfidation deposits are known to form above and around porphyry copper deposits, while low sulfidation deposits associated with rhyolites may be the result of Climax-type deposit formation at depth (Sillitoe, 1993). A low-sulfidation Mo, Ag, and base-metal deposit was found in an active geothermal site and was interpreted to form from Climax-type deposit at depth (Hulen et al., 1987). Although subvolcanic intrusions and epithermal deposits are spatially and temporally related, determining a direct connection is problematic as there is typically an unmineralized gap between epithermal and subvolcanic ores (Sillitoe, 1993).

Ore formation in epithermal deposits is a function of hydrothermal, structural, and lithological controls (Sillitoe, 1993). Notably, hydrothermal controls such as boiling, mixing, and interaction of magmatic and meteoric fluids influence metal transport and deposition (Simmons et al., 2005). In order for ore fluids to flow upward, faults and fractures must be present to act as conduits for fluid flow (Sillitoe, 1993). Many of these conduits occur as a result of extensional tectonic regimes or fluid pressure (Sibson, 1987). In terms of lithology, the permeability of the host rock affects the size the deposit, with higher permeability promoting larger tonnage (Sillitoe, 1993). Conversely, a reduction in permeability can result in ore deposition, which is found at unconformity bound deposits where a permeable layer is capped by an impermeable layer (Sillitoe, 1993).

#### *1.2.6. Indium Deposits*

To explore for indium-bearing deposits, one must consider the source, transport, and sink of the ore metals. For deposits with a magmatic input the source will be a partial melt of some upper to middle crustal or upper mantle material. The transport of the ore metal will be primarily through the formation of a MVP. The sinks will include crystallization products of the melt and ore minerals. In order to constrain how an indium deposit may form, understanding how indium partitions between crystallization products, melt, and MVP is fundamental. Studies first attempting to characterize indium in rocks and minerals and include, for example: Ahrens and Liebenberg (1950), Ottemann (1940), Shaw (1952), Shaw (1957), Wager et al. (1958), Smales et al. (1957). These early studies concluded that indium was most commonly found in sulfide, but could be partitioned into ferromagnesian

phases. Recent studies have begun looking at indium in granitic systems and determined indium was found in higher concentration in the more evolved systems (e.g. Breiter et al., 2015; Moura et al., 2014; Piccoli et al., 2015; Simons et al., 2017). In the granitic systems, indium in mica concentrations ranged from 0.1 to ~1.1 ppm (Breiter et al., 2015; Piccoli et al., 2015; Simons et al., 2017). Interestingly, Piccoli et al. (2015) found that in the Tuolumne Intrusive Suite hornblende contained three to four time greater indium than biotite. A variety of studies also examined indium in ore minerals including sphalerite, chalcopyrite, stannite, and roquesite, across a multiple deposits from VMS, skarn, vein, and porphyry deposits (for example see Cook et al. (2009), Cook et al. (2011), Dill et al. (2013), Ishihara et al. (2006), Ishihara and Endo (2007), Ishihara et al. (2011a), Ishihara et al. (2011b), Murakami and Ishihara (2013), Sinclair et al. (2006), Valkama et al. (2016), and Zhang et al. (2006)). Although the indium concentration of partial melts (via melt inclusions) has not been measured, it could be estimated that the melt of the average continental crust would contain ~0.05 ppm In, i.e. the estimated indium concentration of the continental crust from Rudnick and Gao (2003). The concentration of indium in fluid inclusions was measured by Zhang et al. (2006) at the Meng'entaolgai deposit in Mongolia, China and ranges from 0.8 to 3.5 ppm. However, it is unclear if these values are representative of indium bearing deposits. Additionally, the controls on the indium concentration of the crystallization products, melt, and MVP have not been constrained. In this study, indium crystal/melt and vapor/melt partition coefficients will be used to model ore forming processes of felsic-magmatic systems. Given that biotite and amphibole are the most common ferromagnesian phases in

granitic systems, they will play the primary role in the sequestration of indium prior to the formation of the MVP.

Experimentally determined partition coefficients for indium between crystal and melt, in felsic melts are sparse. Partition coefficients do exist for indium between crystal and melt; however, the pressure, temperature, melt composition, and crystalline phases differ from magmatic-felsic conditions. Matsui (1977) reported partition coefficients between various phenocryst-groundmass combinations including olivine-basalt, bronzite-basalt, augite-basalt, hornblende-basalt, hornblende-andesite, and biotite-dacite. Onuma et al. (1968) reported phenocryst-groundmass partition coefficients for an augite-basalt pair. Adam and Green (2006) investigated trace element partitioning of 35 elements, including indium, between mica, amphibole, garnet, clinopyroxene, orthopyroxene, olivine and a basaltic melt at 1 to 3.5 GPa and 1,025 to 1,190°C. Hill et al. (2000) also reported partition coefficients for multiple elements, focusing on a Ca-Tschermak exchange, including indium between clinopyroxene and a silicate (high CaO (17-27%) low SiO<sub>2</sub> (43-53%)), melt at 0.1 MPa and 1,218°C. Westrenen et al. (1999) reports indium partitioning, along with other trace elements, between garnet and an anhydrous silicate melt (40 to 48% SiO<sub>2</sub>) at 3 GPa and 1,530 to 1,565°C. Kayser (2013) determined partition coefficients for indium between pyrrhotite and a rhyolitic melt at 100 MPa and 800° C. Table 1 contains a list of the partition coefficients determined in the studies mentioned.

Table 1

Partition coefficients for indium between crystalline phases and melt compiled from literature data

	Crystalline Phase	Melt	Partition Coefficient	Pressure (MPa)	Temperature (°C)
Kayser (2013)					
	Pyrrhotite	High Silica Rhyolite	4	100	800
Matsui (1997)					
	Olivine (Phenocryst)	Basalt (Groundmass)	0.016	n.a.	n.a.
	Bronzite (Phenocryst)	Basalt (Groundmass)	0.45	n.a.	n.a.
	Augite (Phenocryst)	Basalt (Groundmass)	1.67	n.a.	n.a.
	Hornblende (Phenocryst)	Basalt (Groundmass)	2.16	n.a.	n.a.
	Hornblende (Phenocryst)	Andesite (Groundmass)	3.1	n.a.	n.a.
	Biotite (Phenocryst)	Dacite (Groundmass)	3.9	n.a.	n.a.
Adam and Green (2006)					
	Mica	Basanitic	0.13 to 0.3	1,000 to 3,500	1,025 to 1,190
	Amphibole	Basanitic	1.09 to 2.54	1,000 to 3,500	1,025 to 1,190
	Garnet	Basanitic	10 to 87	1,000 to 3,500	1,025 to 1,190
	Clinopyroxene	Basanitic	0.4 to 3.0	1,000 to 3,500	1,025 to 1,190
	Orthopyroxene	Basanitic	0.24	1,000 to 3,500	1,025 to 1,190
	Olivine	Basanitic	0.09 to 0.2	1,000 to 3,500	1,025 to 1,190
Hill et al. (2000)					
	Clinopyroxene	High Calcium Low Silica	1.33 to 2.77	0.1	1,218
Onuma et al. (1968)					
	Augite (Phenocryst)	Basalt (Groundmass)	1.67	n.a.	n.a.
Westerenen et al. (1999)					
	Garnet	Low Silica	2.1 to 2.5	3,000	1,530 to 15,650

See text for details of experimental studies. All partition coefficients determined by Onuma et al. (1968) and Matsui (1997) are of natural samples of Phenocryst/Groundmass and P-T conditions are not available (n.a.) for those samples analyzed.

### 1.3. Hypothesis

Primary scientific working hypothesis: In felsic magmas indium behaves as a compatible element in the ferromagnesian minerals relative to the silicate melt, i.e.

$$D_{\text{In}}^{\text{Mineral/Melt}} > 1.$$

Alternate hypothesis 1: In felsic magmas indium behaves as an incompatible element in the ferromagnesian minerals relative to the silicate melt, i.e.  $D_{\text{In}}^{\text{Mineral/Melt}} < 1$ .

Alternate hypothesis 2: In felsic magmas indium behaves as neither compatible nor incompatible element in the ferromagnesian minerals relative to the silicate melt, i.e.  $D_{\text{In}}^{\text{Mineral/Melt}} = 1$ .

To test these hypotheses experiments were performed at magmatic conditions (750° C to 800° C and 100 MPa) for durations of 1 to 8 weeks to measure  $D_{\text{In}}^{\text{Bt/Melt}}$  and  $D_{\text{In}}^{\text{Am/Melt}}$ . If data are consistent with either the primary scientific working hypothesis or alternate hypothesis 1 a secondary scientific working hypothesis can be formulated.

Secondary working hypothesis: When indium behaves compatibly or incompatibly, the proportion of indium removed from the melt is a function of the proportion of ferromagnesian minerals in the crystallization products of the melt. Thus, indium may be sequestered by ferromagnesian phases, precluding the formation of a MVP, and preventing the formation of an indium deposit.

Alternate hypotheses: The proportion of ferromagnesian minerals crystallizing from a melt is not large enough to influence the proportion of indium

removed from the melt, and thus has no affect on the formation of an indium ore deposit.

These hypotheses will be tested by conceptual modeling the efficiency of removal of indium from the melt and into the coexisting volatile phase. The efficiency of removal will be evaluated on the basis of the proportion of ferromagnesian phase and timing of volatile saturation relative to the crystallization of the melt.

## **Chapter 2: Experimental Techniques**

### *2.1. Introduction to Experimental Techniques*

The primary scientific working hypothesis was tested through a series of cold-seal pressure vessel experiments conducted at the University of Maryland. Experiment comprises three parts, the cold-seal vessel, tub furnace, and experimental charge. Each part is described below.

### *2.2. Cold-Seal Pressure Vessels and Tube Furnaces*

The cold-seal pressure vessels used in this study are originally described by Tuttle (1949). They are made of René 41 (Ni-based) superalloy, with each vessel having a 1 inch outer diameter and a 0.25 inch diameter center borehole drilled to ~1 inch from the vessel end. Each vessels also has a thermocouple well, which is 0.125 inch diameter hole (that does not penetrate the center borehole) at end of the vessel. The vessels are pressurized via an air-driven water pump connected to a series of high-pressure tubing and a Bourdon tube gauge. Vessels are in direct communication with the gauge, allowing pressure to be monitored and adjusted during heating, run

time, and on quench. Each vessel can be isolated from the pressure system, enabling multiple experiments to be performed simultaneously. Vessels are externally heated in sub-horizontal furnaces. The hot end of the furnace is tilted upwards  $8^\circ$  degrees, to limit convection and decrease the thermal gradient across the capsule. Each furnace comprises a double winding of Kanthal A-1 wire wrapped around a ceramic core and surrounded by a silica insulation blanket. The “primary” Kanthal winding is the main heat source for the furnace and runs the length of the ceramic core. The primary winding has a resistance of  $\sim 15$  ohms and draws  $\sim 8$  A. The “secondary” Kanthal winding is wrapped around the back of the core near the hot spot of the furnace. This winding is connected to a variAC that restricts the voltage and can be adjusted to an output of between 0 and 120 V. This winding is used to fine tune the location of the hotspot and eliminate a thermal gradient across capsules. The temperature of the furnace is monitored by a type-K (chromel-alumel) thermocouple placed at the back of the furnace and adjusted by an external, digital temperature controller. During experimental runs the temperature of the vessel is monitored by type-K thermocouple placed inside of the vessel well.

### 2.3. *Experimental Charges*

#### 2.3.1. *General Design*

Each experimental charge is contained inside a sealed gold or platinum capsule. Preparation of capsules starts by cutting a piece of gold (outer diameter of 5 mm, wall thickness of 0.127 mm) or platinum (outer diameter of 2 or 3 mm, wall thickness of 0.127) tubing to the desired length (10 mm for platinum and  $\sim 17$  mm for gold). Gold capsules were tri-crimped and welded at one end and platinum capsules

were crimped along one direction and welded at one end. After welding, capsules were cleaned in distilled water followed by an acetone bath. Each starting material was individually weighed ( $\pm 0.1\%$ ) and loaded into the capsule. Starting solutions were electronically pipetted and weighed. After capsules were loaded they were crimped at the open end, welded shut, and weighed. Each sealed capsule is placed in an oven at  $110^{\circ}\text{C}$  for a minimum of 4 hours to check for leaks. Capsules were then removed from the oven and weighed to assess the loss of volatiles. Capsules that show no loss of volatiles ( $\pm 0.5\text{ mg}$ ) were loaded into the cold-seal vessel with the charge side placed into the hot end of the vessel. After placing a capsule in the vessel, a filler rod was inserted to reduce the total volume of water needed to reach run pressures. The filler rods in a majority of experiments were alumina rods. These rods experienced extensive breakdown during longer runs and were abandoned in favor of nickel rods to prevent damage to vessels. At the end of each experiment vessels were removed from the furnace and quenched in air. Vessels reached  $<300^{\circ}\text{C}$  in 3 minutes or less. Capsules were then removed from the vessel, weighed to check for any changes in mass, and then opened to inspect run products. Capsules experiencing less than a 2 mg weight change are deemed successful runs. Any capsule experiencing greater than a 2 mg weight change was closely inspected for signs of failure. Capsules showing a gain in weight were inspected for punctures and signs of pressure medium water entering the capsule. If no signs of pressure medium water entering the capsules was observed, i.e. no flooding of the capsule is present, capsules were deemed successful. In some instances, metal debris from the cold-seal vessel precipitated on the capsule causing weight gain. If flooding was present the

capsule was discarded. Weight loss is attributed to a loss of aqueous starting solution or loss of gold from the capsule. If capsules show a loss of weight but presences of hydrous crystalline phases and no signs of pressure medium water entering the capsule, capsules were interpreted to have failed on quench and deemed successful.

The starting materials used varied depending on the type of experiment being conducted and include a combination of the following: Bishop Tuff from the Long Valley Caldera, California (Laboratory for Mineral Deposits Research (LMDR) collection); biotite and biotite seeds (from Yosemite sample Y-14 from Piccoli, 1992), and amphibole seeds from the Half Dome Equigranular unit in Yosemite, California (sample Y-4 Piccoli, 1992); sanidine hand-picked from the Bishop Tuff; magnetite (88  $\mu\text{m}$  in size) from Mineville, Essex County, New York (LMDR collection); enstatite (150  $\mu\text{m}$  in size) from Bamble, Norway (Smithsonian sample R2958); and a basalt glass (75  $\mu\text{m}$  in size) from the Juan de Fuca MORB (sample JdF MORB from Arevalo and McDonough, 2008). Composition of starting materials is given in Table 2. Between experiments, two starting materials are ubiquitous, the aqueous chloride solution (0.5 KCl, 0.5 NaCl, 0.01 HCl) and InAu (5 wt% In, 95 wt% Au) alloy, both made at the Laboratory for Mineral Deposits Research, University of Maryland.

Table 2

Composition of starting material in wt%

	Bishop Tuff Rhyolite (N=20)	Bishop Tuff Sanidine (N=10)	Y-14 Biotite (N=6)	Mineville Magnetite (N=5)	Bamble Enstatite (N=5)	Juan de Fuca Basalt (N=28)*	Half Dome Equigranular Amphibole (N=36)**	GRI <sup>a</sup>
SiO <sub>2</sub>	74.0 ± 0.4	65.89 ± 0.2	38.5 ± 0.3	0.08 ± 0.02	58.2 ± 0.2	51.01 ± 0.05	50.5 ± 0.9	75.2
Al <sub>2</sub> O <sub>3</sub>	14.9 ± 0.4	18.90 ± 0.1	13.9 ± 0.1	0.30 ± 0.01	0.20 ± 0.02	13.95 ± 0.03	5.6 ± 0.9	11.1
TiO <sub>2</sub>	0.06 ± 0.01	0.03 ± 0.02	2.5 ± 0.1	0.61 ± 0.02	0.05 ± 0.02	1.92 ± 0.01	0.63 ± 0.09	0.03
FeO	0.85 ± 0.03	0.13 ± 0.02	15.9 ± 0.3	91.0 ± 0.1	2.5 ± 0.1	11.99 ± 0.03	13.3 ± 0.9	0.04
MgO	0.05 ± 0.01	0.01 ± 0.01	13.5 ± 0.1	0.02	39.3 ± 0.2	7.06 ± 0.02	14 ± 1	0.1
MnO	0.07 ± 0.02	0.04 ± 0.03	0.62 ± 0.02	0.13 ± 0.01	0.03 ± 0.01	0.203 ± 0.004	0.62 ± 0.05	0.01
CaO	0.5 ± 0.02	0.27 ± 0.02	b.d.	b.d.	0.05 ± 0.02	11.25 ± 0.02	11.8 ± 0.9	0.2
Na <sub>2</sub> O	2.8 ± 0.02	3.8 ± 0.1	0.17 ± 0.03	0.04 ± 0.01	0.03 ± 0.01	2.7 ± 0.01	1.1 ± 0.3	3.7
K <sub>2</sub> O	4.7 ± 0.03	10.27 ± 0.1	8.96 ± 0.3	b.d.	0.01 ± 0.01	0.084 ± 0.001	0.46 ± 0.07	4.40
Cl	0.022 ± 0.004	b.d.	b.d.	b.d.	0.04 ± 0.01	n.a.	0.02 ± 0.01	-
In <sub>2</sub> O <sub>3</sub>	b.d.	b.d.	b.d.	b.d.	b.d.	n.a.	n.a.	n.a.
Total	98 ± 1	99.3 ± 0.2	94.1 ± 0.5	92.2 ± 0.1	100.4 ± 0.3	100.2 ± 0.1	98 ± 2	95

Analyses carried out via Electron Microprobe Analysis (EPMA).

b.d. indicates below the detection of EPMA

n.a. is not analyzed

\* Analysis performed by John Nance (LMDR)

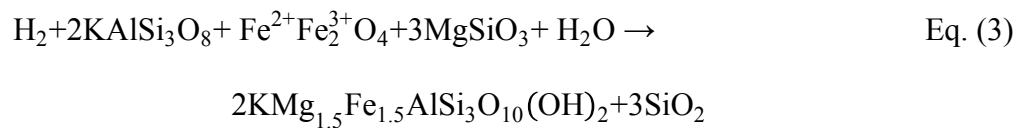
\*\* Analysis performed by Caroline Webber (LMDR)

<sup>a</sup>Analysis from Frank (2001)

### 2.3.2. *Biotite/Melt Experimental Design*

Biotite/melt partitioning experiments were conducted in three sets. Initial experiments were run at temperatures of 800° C; however, later experiments were conducted at 750° C. Lower temperature experiments were performed to promote the growth of biotite. According to Naney (1983) (Figure 3), a run temperature of 750° C will have the crystallization assemblage of biotite + plagioclase + liquid; however, a run temperature of 800° C will stabilize hornblende. Using a run temperature of 750° C ensures biotite is the primary ferromagnesian mineral crystallizing. It should be noted that phase assemblages according to Naney (1983) were determined at 200 MPa and experiments conducted in this study were conducted at 100 MPa. The pressure difference between 200 and 100 MPa affects the solubility of water in the melt (Papale et al., 2006), thus shifting the vapor saturation line in Figure 3 to the left. This affect should not change the crystalline phases present.

The first set of experiments was performed in gold capsules by using the starting materials: 1) Bishop Tuff + biotite + In<sub>5</sub>Au<sub>95</sub> alloy + aqueous chloride solution (0.5 KCl, 0.05 NaCl, 0.01 HCl). This design was abandoned in favor of set two (Figure 5), which was conducted in gold capsules comprising the starting materials Bishop Tuff + sanidine + magnetite + enstatite + In<sub>5</sub>Au<sub>95</sub> alloy + aqueous chloride solution (0.5 KCl, 0.05 NaCl, 0.01 HCl) + biotite seed crystal. Experimental set two results in the nucleation and growth of biotite according to equation 3.



The third set of biotite experiments were conducted in platinum capsules by using the same starting materials as set two. These experiments included a CoPd  $f_{O_2}$  sensor described in Appendix A after Taylor et al. (1992). The  $f_{O_2}$  sensor in these experiments failed due problems with Pd metal used (Appendix A). The Bishop Tuff in sets two and three were separated from the sanidine + magnetite + enstatite by a gold foil barrier to prevent contamination of the melt. The InAu alloy is loaded into a 3 mm diameter gold tube prior to being loaded into the outer capsule to prevent alloying with the outer capsule. Biotite seeds are placed on the inner capsule and held by a small (<0.1 mg) drop of superglue. If all superglue is converted to CO<sub>2</sub>, ~700 ppm of CO<sub>2</sub> is created and distributed throughout the charge. This amount of CO<sub>2</sub> is not expected to affect results.

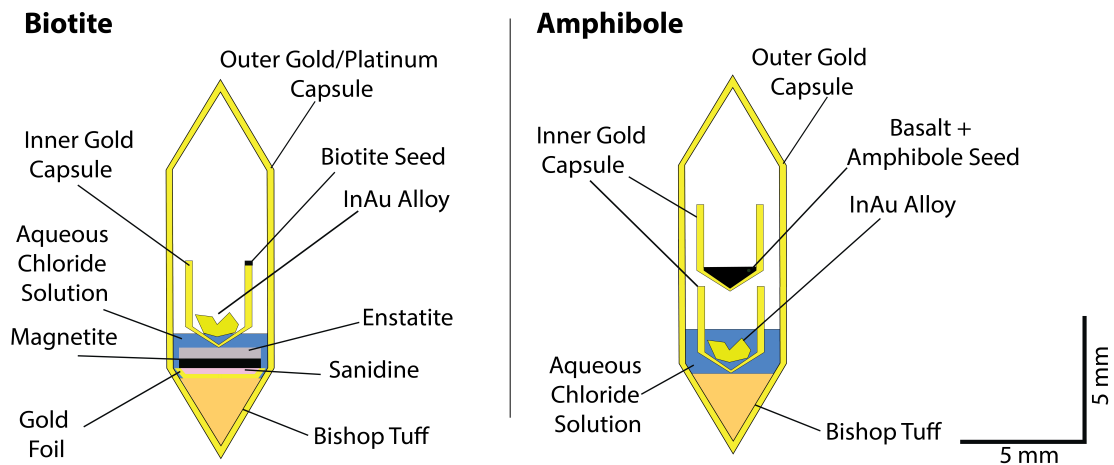


Figure 5: Configuration of biotite and amphibole experiments

### 2.3.3. Amphibole/Melt Partitioning Experimental Design

Experiments designed to nucleate and grow amphibole were conducted in gold capsules at 800° C and 100 MPa. Similar to biotite experiments, a run

temperature of 800°C was chosen to promote the growth of amphibole (Figure 3). These experiments comprised the assemblage Bishop Tuff + Juan de Fuca basalt glass + InAu alloy + aqueous chloride solution (0.5 KCl, 0.05 NaCl, 0.01 HCl) + amphibole seeds (Figure 5). The ratio of Bishop Tuff to Juan de Fuca basalt varied from 3:1 to 6:1. Creating a felsic dominated system results in the breakdown of the basalt and the crystallization of amphibole.

#### *2.3.4. Vapor/Melt Partitioning Experimental Design*

In select biotite/melt and amphibole/melt experiments the aqueous chloride solution was recovered after quench using a glass microcapillary. The aqueous fluid recovered could then be used to obtain a vapor/melt partition coefficient.

### *2.4. Experimental Controls and Theory*

#### *2.4.1. Fugacity*

Fugacity is a master variable in nature and in experiments that mimic natural conditions. Oxygen fugacity ( $f_{O_2}$ ) affects the partitioning behavior of various metals (e.g. Candela and Bouton (1990) and Jugo et al. (1999)), which in turn affects their efficiencies of removal during ore forming processes (Candela, 1989a). Controlling  $f_{O_2}$  is done by applying a known  $f_{H_2O}$  to a capsule made of a hydrogen permeable membrane. Capsules comprise a noble metal, such as Pd, Pt, and Au, which are permeable to hydrogen at  $T > 650^\circ C$  (Chou, 1986). In principle, if one knows the  $f_{H_2O}$  inside of the capsule and the  $f_{H_2}$  outside of the capsule, thus the  $f_{H_2}$  inside the capsule, then the  $f_{O_2}$  inside the capsule can be calculated.

Another technique utilizes a solid oxygen fugacity buffer. This technique was first described by Eugster (1957) using a double capsule. This technique uses an outer capsule containing the  $f_{O_2}$  buffer assemblage (e.g. hematite or nickel powder and water) with an inner capsule containing the experimental charge. The technique allows the  $f_{O_2}$  to be fixed at a given buffer assemblage, so long as the  $f_{H_2}$  of the vessel is near the  $f_{H_2}$  of the buffer assemblage. In vessels with a water pressure medium, the intrinsic  $f_{O_2}$  of the vessel may dominate the buffer assemblage due to the high  $f_{H_2}$  created by the water. This is the case when using René 41 cold-seal. The alloy is primarily Ni and in the presence of water, oxidizes forming NiO ( $2Ni + 2H_2O = 2NiO + 4H$ ), thus the  $f_{O_2}$  should approximate the Nickel-Nickel Oxide (NNO) buffer. The intrinsic  $f_{O_2}$  of the vessel was measured by CoPd sensors as described in Appendix A. Four sensors were used in separate runs with no experimental charges present, two at 750°C with an alumina filler rod and two at 800° C with a Ni filler rod, all runs were at 100 MPa. The two 750° C sensors gave intrinsic  $f_{O_2}$  values of  $NNO + 1.33 \pm 0.01$  and  $NNO + 1.26 \pm 0.04$ . The two 800° C sensors gave intrinsic  $f_{O_2}$  values of  $NNO + 0.88 \pm 0.05$  and  $NNO + 2.0 \pm 0.2$ .

In biotite/melt experiments containing the assemblage annite + sanidine + magnetite the intrinsic  $f_{O_2}$  may be affected by the assemblage or the assemblage may serve as an  $f_{O_2}$  sensor. Wones and Eugster (1965) first described a geohygrometer to calculate the  $f_{H_2O}$  of a system based on the annite + sanidine + magnetite assemblage. This was improved upon by Mueller (1972) and Wones (1972) and later updated and calibrated by Czamanske and Wones (1973) to yield equation 4:

$$\log(f_{\text{H}_2\text{O}}) = \left(\frac{7409}{T}\right) + 4.25 + \frac{1}{2} \log(f_{\text{O}_2}) + 3 \log(X_{\text{Fe}^{2+}}^{\text{Bt}}) + 2 \log(X_{\text{OH}}^{\text{Bt}}) \quad \text{Eq. (4)}$$

$$- \log(a_{\text{KAlSi}_3\text{O}_8}) - \log(a_{\text{Fe}^{2+}\text{Fe}_2^{3+}\text{O}_4}) \quad ,$$

which can be rearranged to yield equation 5:

$$\log(f_{\text{O}_2}) = 2 \left( \frac{\log(f_{\text{H}_2\text{O}}) + \log(a_{\text{KAlSi}_3\text{O}_8}) + \log(a_{\text{Fe}^{2+}\text{Fe}_2^{3+}\text{O}_4}) - 2 \log(X_{\text{OH}}^{\text{Bt}}) - 3 \log(X_{\text{Fe}^{2+}}^{\text{Bt}}) - 4.25 - \left(\frac{7409}{T}\right)}{\quad} \right) \quad \text{Eq. (5)}$$

where  $a_{\text{KAlSi}_3\text{O}_8}$  is the activity of the sanidine component of alkali feldspar,  $a_{\text{Fe}^{2+}\text{Fe}_2^{3+}\text{O}_4}$  is the activity of the magnetite component of spinel,  $X_{\text{OH}}^{\text{Bt}}$  is the mole fraction of OH in biotite,  $X_{\text{Fe}^{2+}}^{\text{Bt}}$  is the mole fraction of ferrous iron in the octahedral site of biotite, and T is temperature in Kelvin. The activities of sanidine, magnetite, and annite components are discussed below. By using this assemblage in experimental charges a potential  $f_{\text{O}_2}$  sensor is built into the experimental design. The use of this low variance assemblage as an  $f_{\text{O}_2}$  sensor was tested and will be discussed in Chapter 5.

#### 2.4.2. Activity of the Annite Component of Biotite

Using biotite as an indicator of  $f_{\text{H}_2\text{O}}$  or  $f_{\text{O}_2}$  can be problematic when using equations such as those given by Czamanske and Wones (1973), mainly due to multiple substitutions in the octahedral site, and to an extent the hydroxyl site. Wones and Eugster (1965) noted this in their original work stating that the molecular (equation 6) or ionic (equation 7) models

$$\frac{\text{Fe}}{(\text{Fe}+\text{Mg})} \quad \text{Eq. (6)}$$

$$\left[ \frac{\text{Fe}^{2+}}{\text{Fe}^{2+}+\text{Mg}} \right]^3 \quad \text{Eq. (7)}$$

were insufficient to describe the activity of the annite component of biotite, as the biotite were non-ideal. Mueller (1972) came to the conclusion that in biotite with low (less than a few wt%)  $\text{Fe}^{3+}$  the ionic model (equation 8) is sufficient.

$$a_{\text{annite}} = (X_{\text{Fe}^{2+}}^{\text{Bt}})^3 \quad \text{Eq. (8)}$$

Wones (1972) recalibrated the equation of Wones and Eugster (1965), accepting the ideas of Mueller (1972). Czamanske and Wones (1973) explored the ionic model further when applying the equation of Wones (1972) to Finnmarka Complex biotite, which has large concentrations of fluorine, filling up to 65% of the hydroxyl site. Czamanske and Wones (1973) suggested an updated ionic model (equation 9 and 10) and updated the equation of Wones (1972) to equation 4.

$$a_{\text{annite}} = (X_{\text{Fe}^{2+}}^{\text{Bt}})^3 (X_{\text{OH}}^{\text{Bt}})^2 \quad , \quad \text{Eq. (9)}$$

$$\log(a_{\text{annite}}) = 3\log(X_{\text{Fe}^{2+}}^{\text{Bt}}) + 2\log(X_{\text{OH}}^{\text{Bt}}) \quad , \quad \text{Eq. (10)}$$

Another possible estimation of the activity of the annite component was presented by Bohlen et al. (1980) who use a completely ionic model (equation 11):

$$a_{\text{annite}} = \frac{(X_{\text{Fe}^{2+}}^{\text{Bt}})^3 (X_{\text{Al}}^{\text{Bt}})(X_{\text{Si}}^{\text{Bt}})^3 (X_{\text{OH}}^{\text{Bt}})^2}{(X_{\text{Al}}^0)(X_{\text{Si}}^0)^3} \quad , \quad \text{Eq. (11)}$$

where  $X_{\text{Al}}^0$  is the mole fraction of aluminum in pure annite and  $X_{\text{Si}}^0$  is the mole fraction of silicon in pure annite. Bohlen et al. (1980) states this provides the lower limit of  $f_{\text{H}_2\text{O}}$  (upper  $f_{\text{O}_2}$  in this study), whereas the molecular model of Wones and Eugster (1965) (equation 6) provides an upper limit of  $f_{\text{H}_2\text{O}}$  (lower  $f_{\text{O}_2}$  in this study). When comparing estimations of activity to the experimental data presented here, given a fixed  $f_{\text{H}_2\text{O}}$ , the partly ionic model of Czamanske and Wones (1973) provides the best estimate of  $f_{\text{O}_2}$ . Comparing the  $f_{\text{O}_2}$  calculated by the various activity models can be

done by substituting the activity calculated from the respective model into equation 5. It should be noted that to properly apply this calculation, the amount of  $\text{Fe}^{3+}$  in the octahedral site must be estimated during the calculation of the biotite formula. The method outlined by Dymek (1983) is preferred here.

#### *2.4.3. Activity of the Sanidine Component of Alkali Feldspar*

The activity of the sanidine component of alkali feldspar is a function of  $X_{\text{KAlSi}_3\text{O}_8}$  and was determined by Waldbaum and Thompson (1969) to be non-ideal. The starting sanidine has a  $X_{\text{KAlSi}_3\text{O}_8}$  of 0.62, thus the activity of sanidine was approximated to be 0.6 following Waldbaum and Thompson (1969).

#### *2.4.4. Activity of the Magnetite Component of Spinel*

The activity of the starting magnetite component of spinel was calculated using the MELTS supplementary calculator, which is based on the model of Sack and Ghiorso (1991) and determined to be  $\sim 0.97$ . The magnetite formula was calculated on the basis of 4 oxygen and the amount of  $\text{Fe}^{2+}$  and  $\text{Fe}^{3+}$  per formula unit was determined by the method of Droop (1987).

#### *2.4.5. Water Fugacity*

Water fugacity ( $f_{\text{H}_2\text{O}}$ ) was calculated using the online “Thermodynamic Properties of Fluid Mixtures” calculator ([http://fluid-eos.web.psi.ch/EOS/calculator\\_simple.html](http://fluid-eos.web.psi.ch/EOS/calculator_simple.html)), which is based on Churakov and Gottschalk (2003a, 2003b). For experiments at 100 MPa and 750° C the  $f_{\text{H}_2\text{O}}$  is 80 MPa and for experiments at 100 MPa and 800° C is 84 MPa.

### 2.5. Aluminum Saturation Index (ASI)

The Aluminum Saturation Index (ASI) is defined as the ratio of molar  $\text{Al}_2\text{O}_3$  to  $\text{K}_2\text{O} + \text{Na}_2\text{O} + \text{CaO}$ . The ASI of the starting Bishop Tuff is  $\sim 1.4 \pm 0.2$ . The target ASI for each experiment was between 1 and 1.2. The slightly peraluminous ASI was chosen to maximize the effect of partitioning of indium into the crystalline phases. Dingwell et al. (1997) determined that at an ASI of  $\sim 1.1$  the solubility of  $\text{H}_2\text{O}$  is at a minimum. Likewise, melts with higher ASIs tend to produce higher partition coefficients between mineral/melt (Prowatke and Klemme, 2005), thus providing a limiting case for trace element partitioning.

## **Chapter 3: Analytical Techniques**

### 3.1. Sample Preparation

After capsules have been opened, the run products (glasses and mineral phases) were extracted and prepared for analysis. Sample preparation for glasses was done by mounting samples in one-inch epoxy rounds using Buehler© EpoFix or Struers EpoFix epoxy and optically polished until perpendicular to the electron beam. Polishing takes place in the following steps: 600 grit (15  $\mu\text{m}$ ) SiC sand paper, 9  $\mu\text{m}$ , 3  $\mu\text{m}$ , 1  $\mu\text{m}$  diamond polish on paper, and finally a 0.05  $\mu\text{m}$  Linde B™ alumina polish on a felt pad. Biotite samples were mounted differently due to their small surface area and thickness. Initial mounting involved placing biotite on carbon or double-sided Scotch tape, but was abandoned due to problems in obtaining a flat and incident sample surface. As an alternative, biotite samples were mounted in an “inverted-epoxy mount” in the following manner. Epoxy is poured into a standard one inch

round mount and allowed to harden for ~1-2 hours. After the epoxy is viscous enough to support weight, biotite samples are gently laid on top of the epoxy mount, taking care not to submerge them. Once the biotite is in place, slight pressure is applied to the surface of the biotite depressing the epoxy. This pressure ensures the underside of the biotite is in contact with the epoxy and disturbs its natural state (i.e. there are topographically higher and lower points). The epoxy rebounds, creating a flat surface. Amphibole crystals were mounted using both methods depending on crystal shape. Amphiboles that were small (<100  $\mu\text{m}$ ) in size or displayed a naturally flat side were mounted in same method as biotite. Larger amphiboles or amphiboles with irregular shapes were mounted in the same method as run product glasses. All mounts are coated with a 200-300 Å thick layer of carbon after polishing. Fluids that were extracted from experiments were diluted in 2 w/w% nitric acid to stabilize solution prior to analysis.

### 3.2. Optical Microscopy

A binocular microscope was used to inspect and open gold capsules at the end of each experiment, determine mineral phases present, and mount run products in epoxy.

### 3.3. Electron Probe Microanalysis (EPMA)

EPMA was used to analyze major and minor elements in run products and starting materials. Analyses were done in three stages: standards, major elements, and minor elements. Microprobe conditions for each analytical stage are given in Table 3 and standards used are given in Table 4. Energy Dispersive Spectroscopy was

performed to check mineral phases present, whereas quantitative analysis was performed via Wavelength Dispersive Spectroscopy. The x-ray line used to quantify each element, as well as counting times and respective crystals used are provided in Table 5. Depending on the combination of conditions cited, the analytical depth is between ~1.6 to ~2.6  $\mu\text{m}$  for biotite/amphibole and between ~1.9 to ~2.9  $\mu\text{m}$  for glass, with the analytical volume being between ~30 and ~2000  $\mu\text{m}^3$  as determined by the Monte Carlo simulation program CASINO (Drouin et al., 2007; Drouin et al., 1997; Hovington et al., 1997a; Hovington et al., 1997b).

Table 3  
Operating Conditions for EPMA

	<b>Current (nano-Amps)</b>	<b>Accelerating Voltage (kV)</b>	<b>Beam diameter (<math>\mu\text{m}</math>)</b>
<b>Major Element Standardization</b>	10	15	20 or 30
<b>Minor Element Standardization</b>	25/200	20	20 or 30
<b>Major Element Analysis</b>	10	15	20 to 30
<b>Minor Element Analysis</b>	200	20	2 to 30

Table 4  
Standards used for EPMA analysis

	<b>Glass Analysis</b>	<b>Biotite/Amphibole Analysis</b>
<b>SiO<sub>2</sub></b>	Yellowstone-Rhyolite	Hornblende-Kakanui
<b>Al<sub>2</sub>O<sub>3</sub></b>	Yellowstone-Rhyolite	Hornblende-Kakanui
<b>TiO<sub>2</sub></b>	Makaopuhi -Basalt	Hornblende-Kakanui
<b>FeO</b>	Makaopuhi -Basalt	Hornblende-Kakanui
<b>MgO</b>	Makaopuhi -Basalt	Hornblende-Kakanui
<b>MnO</b>	Rhodonite	Rhodonite
<b>CaO</b>	Makaopuhi -Basalt	Hornblende-Kakanui
<b>Na<sub>2</sub>O</b>	Yellowstone-Rhyolite	Hornblende-Kakanui
<b>K<sub>2</sub>O</b>	Yellowstone-Rhyolite	Microcline
<b>Cl</b>	Scapolite	Scapolite
<b>In<sub>2</sub>O<sub>3</sub></b>	InAs and NIST610	InAs and NIST610

Analyzing indium in both biotite and amphibole proves to be problematic due to the x-ray interferences from both potassium and iron. The  $K\alpha$  x-ray peak of potassium interferes with the  $L\alpha$  peak of indium at the approximately the same L-value. On the PETH crystal the L-value of potassium is 119.86 mm and for indium is 120.85 mm, as determined by  $L=n\lambda(R/d)$ , where R equals 140 mm, 2d equals 8.74 and  $n=1$  according to Bragg's Law,. Similarly, the  $K\beta$  peak of iron overlaps with the  $L\beta$  peak of indium. On the PETH crystal the L-value of iron is 112.54 mm and for indium is 113.88 mm, as determined by  $L=n\lambda(R/d)$  where R equals 140 mm, 2d equal 8.74 and  $n=1$  for indium and  $n=2$  for iron according to Bragg's Law. Fe interference is overcome using a single channel analyzer that filters out the  $K\beta$  x-rays of iron and only accepts wavelengths of a certain energy window at the L-value of indium. This

Table 5  
Summary of count times and crystals used for EPMA analyses

Element	X-ray line	Time counting X-rays On/Off (sec)	Spectrometer	Crystal	Peak Position (mm)	
					n = 1	n=2
Na	$K\alpha$	30/5	1	TAP	129.46	258.92
K	$K\alpha$	20/5	2	PETH	119.86	239.72
Ca	$K\alpha$	30/5	3	PETJ	107.59	215.17
Fe	$K\alpha$	30/5	4	LIF	134.64	n/a
Fe	$K\beta$	n.a.	2	PETH	n/a	112.54
Al	$K\alpha$	20/5	5	TAP	90.64	181.29
Mg	$K\alpha$	20/5	1	TAP	107.50	215.00
Cl	$K\alpha$	30/10	2	PET	151.43	n/a
Ti	$K\alpha$	30/5	3	PETJ	191.15	n/a
Mn	$K\alpha$	30/5	4	LIF	146.24	n/a
Si	$K\alpha$	15/5	5	TAP	77.46	154.92
In	$L\alpha$	n.a.	2	PETH	120.85	241.69
In	$L\beta$	300/150 or 60/30	2	PETH	113.88	227.76

The elements listed with count times of n.a. were not analyzed due to overlaps with indium x-rays (see peak position column). Peak position is in mm and is the L-value of the x-ray according to  $L=n\lambda R/2d$ . The n subheading in the peak position column is the n according to Bragg's Law ( $n\lambda=2d\sin(\theta)$ ). n/a is not available

filter allows the L $\beta$  peak of indium to be resolved on the PETH crystal at L-values of 113.6 mm (background of + 0.65, - 0.85 mm). The detection limit for these analyses are  $3\sigma_m$  and determined by equation 12:

$$D. L. = \frac{1}{\left(\frac{I_{\text{netSTD}}}{\text{wt}\%_{\text{STD}}}\right)} \sqrt{\frac{2 \cdot I_{\text{back}}}{t_{\text{back}}}} \quad , \quad \text{Eq. (12)}$$

where D.L is the detection limit,  $I_{\text{netSTD}}$  is the intensity of the net x-rays of the element of interest in the standard,  $\text{wt}\%_{\text{netSTD}}$  is the concentration of the element of interest in the standard in wt%,  $I_{\text{back}}$  is the average intensity of the background and  $t_{\text{back}}$  is the count time of the

background. Equation 12 is from JEOL (2001). The detection limit for indium is 25 ppm at count times of 300/150 seconds and 50 ppm for count times of 60/30 when utilizing the minor element protocol.

Table 6  
Detection limit of EPMA in ppm

Element	Glass	Biotite	Hornblende
Si	225	250	250
Al	200	220	200
Ti	400	400	400
Fe	500	550	550
Mg	180	200	200
Mn	500	500	500
Ca	200	250	250
Na	180	225	225
K	110	120	120
Cl	80	50	80
In	25-50	25-50	25-50

Detection limits of EPMA analyses for each element. Detection limits are given in ppm. Detection limit of indium varies based on x-ray count times.

Count times were lowered

to reduce total analytical time, without sacrificing analytical resolution.

### 3.4. Laser Ablation Inductively Coupled Plasma Mass Spectrometry (LA-ICP-MS) and Solution Inductively Coupled Plasma Mass Spectrometry (ICP-MS)

Laser ablation inductively coupled plasma mass spectrometry was used to analyze run product biotite that have <25 ppm indium (below detection of EMPA)

and ensure that the indium concentration in starting materials are significantly below 25 ppm. Analyses were done via a UP 213 Nd:YAG laser, coupled with an Element2 mass spectrometer. Laser conditions were as follows: 55  $\mu\text{m}$  diameter spot size, 10 Hz, between 2.5 and 3.5  $\text{J}/\text{cm}^2$ , for an ablation penetration rate of  $\sim 1$   $\mu\text{m}$  per second. The external standard used was NIST610 and Al was used as the internal standard. For all analyses cadmium, tin, and arsenic were monitored to correct for isobaric interferences of  $^{113}\text{Cd}$ ,  $^{115}\text{Sn}$ , and  $^{75}\text{As}^{40}\text{Ar}$ . The lower limit of detection for  $^{113}\text{In}$  ranges from 0.038 to 0.082 ppm and for  $^{115}\text{In}$  ranges from 0.004 to 0.017 ppm.

Aqueous solutions were also analyzed by ICP-MS using the same Element2 mass spectrometer. Solutions are introduced into the mass spectrometer by an Apex nebulizer. Solutions were diluted with 2 w/w% nitric acid until indium concentrations were within the working range, between 1 and 100 ppb, of the mass spectrometer. The standards used for ICP-MS were aqueous solutions doped with 1, 10, 50, and 100 ppb indium. Isobaric interferences for cadmium, tin, and arsenic were also monitored during ICP-MS analyses.

Table 7  
Comparison between EPMA and LA-ICP-MS analytical techniques

	EPMA				LA-ICP-MS				
	In (ppm)	Uncertainty		C.S.	S.D.M.	In (ppm)	Uncertainty		C.S.
±		b.d.	±				b.d.		
<b>Biotite Run 1 (Biotite)</b>	b.d.	±	b.d.	b.d.	24	±	2	3	
<b>Biotite Run 8 (Glass)</b>	730	±	50	50	718	±	1	15	
<b>Biotite Run 13 (Biotite)</b>	b.d.	±	b.d.	b.d.	0.94	±	0.02	0.05	

Detection limits are 25 ppm for EPMA and 0.02 ppm for LA-ICP-MS. b.d. is below detection. C.S. is uncertainty from counting statistics. S.D.M. is standard deviation of the mean.

### 3.5. Comparison of EPMA to LA-ICP-MS

Due to the complexity of analyzing indium in iron- and potassium-bearing phases via the electron microprobe, a comparison of EPMA and LA-ICP-MS was conducted. Two run product biotites, as well as one run product glass were analyzed by both EPMA and LA-ICP-MS. Table 7 compares the results of the EPMA and LA-ICP-MS analyses.

### 3.6. Data Reduction

#### 3.6.1. EPMA

X-ray intensities (counts per second) recorded during analyses were corrected by using the ZAF correction method. After correction, the elements of interest are in their respective oxide forms in weight percent. The data were then run through a first pass filter that determines the quality of analyses. Quality was determined by the following: the point analyzed was the correct and relevant phase, i.e. all points analyzed in a glass are glass and not potassium feldspar or quartz, and that there were no extreme outliers of oxide or analytical totals. Analyses that do not meet the requirements were critically evaluated before rejection, where rejection of an analysis occurred when multiple criteria were not met. The criteria for each filter are given in Table 8. For amphibole experiments, the same filter used for biotite experiments does not apply. In amphibole experiments, the CaO concentration of run product glass was consistently higher than run product glass from biotite experiments, thus analyses failing to meet this criteria are not rejected. For amphibole analyses, given the variability of amphibole compositions and end-members, any analyses with

analytical totals >85% were accepted. After filtering, the mean of each oxide was taken from all points on that sample.

### 3.6.2. LA-ICP-MS and ICP-

#### MS

Data reduction for LA-ICP-MS was conducted by using LAMTRACE data reduction software (Jackson,

2008). The raw data were compiled by LAMTRACE (Jackson, 2008) into spreadsheets. While working with the data reduction software the user is able to define where background and sample signal, start and stop, and where to integrate the signal. In order to distinguish a sample signal from the background signal, the sample signal must be greater than five times that of the background signal. Once the signal and background were defined, the mean counts per second of the background were subtracted from the mean signal of the respective element during ablation. This background corrected counts per second was used to calculate the concentration of the element of interest by equation 13:

$$C_i^{\text{Sam}} = C_{\text{IS}}^{\text{Sam}} \left( \frac{I_i^{\text{Sam}}}{I_{\text{IS}}^{\text{Sam}}} \right) \left( \frac{C_i^{\text{Std}}}{C_{\text{IS}}^{\text{Std}}} \right) \left( \frac{I_{\text{IS}}^{\text{Std}}}{I_i^{\text{Std}}} \right), \quad \text{Eq. (13)}$$

where

$C_i^{\text{Sam}}$  is concentration of element  $i$  in the sample (Sam),

Table 8

Criteria used to as a first pass filter of EPMA data

	<b>Glass</b>	<b>Biotite</b>
<b>Na<sub>2</sub>O</b>	2.75 to 3.8 wt%	b.d. to 0.5 wt%
<b>K<sub>2</sub>O</b>	4 to 6 wt% 0.25 to 0.75	8 to 11 wt%
<b>CaO</b>	wt%	b.d. to 0.03 wt%
<b>FeO</b>	0.2 to 0.8 wt%	Fe number of 0.35 to 0.6
<b>Al<sub>2</sub>O<sub>3</sub></b>	12 to 15 wt%	11 to 15 wt%
<b>MgO</b>	b.d. to 0.2 wt%	Mg number of 0.5 to 0.7
<b>Cl</b>	0.1 to 0.4 wt%	b.d. to 0.5 wt%
<b>MnO</b>	b.d. to 0.2 wt%	b.d. to 0.6 wt%
<b>SiO<sub>2</sub></b>	67 to 74 wt%	36 to 40 wt%
<b>In<sub>2</sub>O<sub>3</sub></b>	-	-
<b>TiO<sub>2</sub></b>	b.d. to 0.2 wt%	1 to 3 wt%
<b>Total</b>	92 to 97 wt%	91 to 96.5 wt%

b.d. is below detection

$C_{IS}^{Sam}$  is the concentration of the internal standard (IS) in the sample,

$I_i^{Sam}$  is the intensity (counts per second minus background) of element  $i$  in the sample,

$I_{IS}^{Sam}$  is the intensity of the internal standard in the sample,

$C_i^{Std}$  is the concentration of element  $i$  in the external standard (Std),

$C_{IS}^{Std}$  is the concentration of the internal standard in the external standard (Std),

$I_{IS}^{Std}$  is the intensity of the internal standard in the external standard, and

$I_i^{Std}$  is the intensity of element  $i$  in the external standard.

Isobaric interferences of indium are corrected for by using the ratio of the natural abundance and equations 14 and 15 for Cd and Sn, respectively.

$$\text{Corrected } ^{113}\text{In (cps)} = \text{Uncorrected } ^{113}\text{In (cps)} - \left( \frac{\text{natural abundance of } ^{113}\text{Cd}}{\text{natural abundance of } ^{112}\text{Cd}} \right) ( ^{112}\text{Cd (cps)}) \quad \text{Eq. (14)}$$

$$\text{Corrected } ^{115}\text{In (cps)} = \text{Uncorrected } ^{115}\text{In (cps)} - \left( \frac{\text{natural abundance of } ^{115}\text{Sn}}{\text{natural abundance of } ^{118}\text{Sn}} \right) ( ^{118}\text{Sn (cps)}) \quad \text{Eq. (15)}$$

These corrected counts rates are used in equation 13 to calculate the concentration of indium in the sample. The isobaric interference of arsenic argides ( $^{75}\text{As}^{40}\text{Ar}$ ) was monitored as well, but did not contribute to the indium signal. Multiple points were analyzed per sample and a mean indium concentration is taken for each sample.

Data for ICP-MS analyses of aqueous run product solutions were reduced using a simple linear relationship of counts per second vs. concentration. The standards used for ICP-MS analyses ranged from 1 to 100 ppb indium. Because the run product aqueous solutions were diluted to between 1 and 100 ppb indium each solution was within the working range of linear relationship. The raw counts per second were corrected for a blank. The cadmium, tin, and arsenic concentration was negligible in run product aqueous solution, thus no correction was made. Blank

corrected count rates were then used to calculate an indium concentration using the linear relationship determined by the standards.

### 3.6.3. Uncertainty and Propagation of Errors

For LA-ICP-MS and ICP-MS uncertainty is calculated from counting statistics by equation 16:

$$Uncertainty = \sqrt{N} \quad , \quad Eq. (16)$$

where N equals the number of counts. For EPMA the standard deviation due to x-ray counting statistics is given in relative percent and is calculated through equation 17 from JEOL (2001):

$$S.D. \% = \frac{100}{I_{net}} \sqrt{\frac{I_{Peak}}{t_{Peak}} + \left(\frac{\overline{L_{PBH}}}{L}\right)^2 \cdot \frac{I_{PBL}}{t_{PBL}} + \left(\frac{\overline{L_{PBL}}}{L}\right)^2 \cdot \frac{I_{PBH}}{t_{PBH}}} \quad , \quad Eq. (17)$$

where

$I_{net}$  is the intensity of the net x-rays at the peak position defined by equation 18,

$$I_{net} = I_{Peak} - \frac{I_{PBH}\overline{L_{PBL}} + I_{PBL}\overline{L_{PBH}}}{\overline{L_{PBL}} + \overline{L_{PBH}}} \quad Eq. (18)$$

$I_{Peak}$  is the intensity of the measured x-rays at the peak position,

$I_{PBH}$  is the intensity of the background x-rays at high angles,

$I_{PBL}$  is the intensity of the background x-rays at low angles,

$\overline{L_{PBL}}$  is the separation of the peak and location of the high angle background measurement,

$\overline{L_{PBH}}$  is the separation of the peak and location of the low angle background measurement,

$t_{Peak}$  is the count time in seconds of the peak,

$t_{PBL}$  is the count time in seconds of the background at low angles,

$t_{PBH}$  is the count time in seconds of the background at high angles, and

$$L = \overline{L_{PBH}} + \overline{L_{PBL}}.$$

A standard deviation of the mean is also taken for each run product and calculated by equation 19:

$$\sigma_m = \frac{\sqrt{\frac{\sum_{i=1}^n (x_i - \bar{x})^2}{n-1}}}{\sqrt{n}}, \quad \text{Eq. (19)}$$

where  $\sigma_m$  is the standard deviation of the mean,  $n$  is the number of points,  $x_i$  is the value of each point, and  $\bar{x}$  is the mean defined by equation 20.

$$\bar{x} = \frac{A_1 + A_2 + \dots + A_n}{n} \quad \text{Eq. (20)}$$

Calculating both standard deviation of the mean and the uncertainty associated with counting statistics allows for the analytical uncertainty and spread in data to be evaluated. In a majority of cases the standard deviation of the mean  $\gg$  uncertainty due to counting statistics.

Error propagation for multiplication and division is done using equation 21:

$$\frac{Un_a}{A} = \sqrt{\left(\frac{Un_b}{B}\right)^2 + \left(\frac{Un_c}{C}\right)^2 \dots + \left(\frac{Un_n}{n}\right)^2}, \quad \text{Eq. (21)}$$

and for addition by equation 22:

$$Un_a = \sqrt{Un_b^2 + Un_c^2 \dots + Un_n^2}, \quad \text{Eq. (22)}$$

where  $Un_{a,b,c}$  is the uncertainty associated with the value a, b, and c, respectively.

## Chapter 4: Results

### 4.1. Biotite/Melt Experiments

#### 4.1.1. Diffusion of Indium into Biotite

Initial experiments containing biotite without the starting materials magnetite + enstatite + sanidine yielded poor results. The indium concentration of biotite in those runs was below the detection limit (25 ppm) of EPMA. It was determined that the incorporation of indium into the structure of pre-crystallized biotite occurs by diffusion. Diffusion occurs at too slow a rate to measure on a laboratory timescale. Therefore, partition coefficients determined without the nucleation and growth of biotite crystals in the presence of indium do not approach the equilibrium  $D_{In}^{Bt/Melt}$ . The time scale needed to diffuse indium into biotite can be estimated on an order of magnitude basis by using equation 23:

$$t \sim \frac{x^2}{k}, \quad \text{Eq. (23)}$$

where  $t$  equals the time for diffusion to occur,  $x$  is the distance to the center of the crystal, and  $k$  is the diffusion coefficient. Indium will diffuse into biotite most rapidly along the smallest length scale of the crystal and will therefore occur parallel to the  $c$  axis. The thinnest possible sheet of biotite is the TOT layer at 1 nm thick (Bower et al., 2015), thus the smallest  $x$  can be equal to is 0.5 nm. The diffusion coefficient for indium in biotite is not available in the literature; in fact relatively few diffusion coefficients for mica are available. In lieu of an indium diffusion coefficient, an estimate is needed based on the available coefficients. Available diffusion coefficients for elements in biotite include K, Rb, and Sr. At 650°C the diffusion

coefficient for both K and Rb is between  $2 \times 10^{-19} \text{ m/s}^2$  and  $7 \times 10^{-20} \text{ m/s}^2$  (Hofmann and Giletti, 1970) and for Sr the diffusion coefficient is  $\sim 6 \times 10^{-22} \text{ m/s}^2$  (Hammouda and Cherniak, 2000). For simplicity the diffusion coefficient used in the following calculations will be  $10^{-20} \text{ m/s}^2$  for simplicity. The time for indium diffusion to take place will take 25 seconds to diffuse through the a single TOT layer. This may seem quick, but the experimental biotite grown are up to  $10 \text{ }\mu\text{m}$  thick. In order for indium to diffuse through the analytical depth, where  $x = \sim 1.9 \text{ }\mu\text{m}$ , it would take  $\sim 11$  years. Taking this calculation a step further, the timescale for indium diffusion in biotite, where  $x$  is  $5 \text{ }\mu\text{m}$ , is  $\sim 80$  years. This greatly exceeds the time available in the laboratory. Even if one assumes that indium diffuses at a rate of  $10^{-19} \text{ m/s}^2$ , similar to the rate of diffusion for Fe or Mg (Usuki, 2002), the timescale for diffusion across the analytical depth is on the order of  $\sim 1$  year. Therefore, in order to measure properly a partition coefficient for indium, biotite must be nucleated and grown from an indium-bearing medium.

#### *4.1.2. Biotite/Melt Partitioning*

Thirteen experiments containing the assemblage magnetite + enstatite + sanidine resulted in biotite nucleation and growth and were deemed successful. Of those experiments, two capsules were interpreted to have experienced minor weight loss on quench and one capsule experienced significant weight gain due to metal precipitation on the capsule. In addition to biotite, phases present in run product assemblages included alkali feldspar, plagioclase, quartz, magnetite, as well as a glass. In five experiments red rhombohedral flakes of hematite were found along the capsule walls near the glass. Also, in five experiments an indium silicate mineral

with the composition  $\text{In}_2\text{Si}_2\text{O}_7$  was found (See below and Chapter 5 for discussion on this phase).

The composition of run product glass from successful experiments is consistent throughout all experiments (Table 9). The ASI of the glass ranges from 0.99 to 1.14, and has a mean of  $1.08 \pm 0.01$  ( $1 \sigma_m$ ). The composition of the run product biotite varies between experiments (Table 10) and is expressed in terms of the mole fraction of annite ( $X_{\text{Annite}}^{\text{Bt}}$ ), which is defined as the fraction of  $\text{Fe}^{2+}$  in the octahedral site. All biotite formulas (Table 11) were calculated by using the method of Dymek (1983), which allows  $\text{Fe}^{3+}$  to be estimated. In two experiments (Biotite Runs 15 and 23) multiple populations of biotite were present (two populations for Run 15 (labeled 15.1 and 15.2) and three populations for Run 23 (labeled 23.1, 23.2, and 23.3)). Subpopulations were determined by significant variations in biotite composition and are evidence for disequilibrium and thus have been excluded from any calculations or regressions. Although experiments 15 and 23 represent disequilibrium  $D_{\text{In}}^{\text{Bt/Melt}}$  was measured for each population and plotted separately for completeness.

The variation in indium concentration and indium per formula unit (p.f.u) correlates with the variation in  $X_{\text{Annite}}^{\text{Bt}}$  (Figure 6). This correlation is the primary control on  $D_{\text{In}}^{\text{Bt/Melt}}$ , which ranges from,  $0.6 \pm 0.1$  ( $1 \sigma_m$ ) to  $16 \pm 3$  ( $1 \sigma_m$ ) (Table 12). As  $X_{\text{Annite}}^{\text{Bt}}$  increases, the amount of indium that partitions into the octahedral site decreases. Thus, a low  $X_{\text{Annite}}^{\text{Bt}}$  (high  $X_{\text{Phlogopite}}^{\text{Bt}}$ ) corresponds to an increase indium in the octahedral site (Figure 7). Likewise, as the silicon p.f.u. in biotite approaches that of an ideal phlogopite ( $X_{\text{Si}}^{\text{IV}} = 3$ ), indium partitioning into the octahedral site

increases increasing the partition coefficient (Figure 8 and 9). Two experiments, Biotite Run 20 and 26, fall off the previously discussed linear trends significantly. At titanium concentrations approaching zero the relationship between  $D_{In}^{Bt/Melt}$  and Ti becomes nonlinear, which corresponds to a deviation from the linear relationship observed in Figures 6-9 (Figure 11). For this reason Biotite Runs 20 and 26 have been excluded from linear regressions of  $D_{In}^{Bt/Melt}$  vs.  $X_{Annite}^{Bt}$ .

All data points, including subpopulations, have been plotted in Figure 7.

Subpopulations are evidence of disequilibrium; however, each population (excluding Biotite Run 15.1) generally follows the linear relationship of  $D_{In}^{Bt/Melt}$  vs.  $X_{Annite}^{Bt}$ .

The linear relationship of  $D_{In}^{Bt/Melt}$  vs.  $X_{Annite}^{Bt}$  results in equation 24:

$$y = -22.3x + 8.9 \quad , \quad \text{Eq. (24)}$$

where y is  $D_{In}^{Bt/Melt}$  and x is  $X_{Annite}^{Bt}$ . The linear relationship only holds for  $X_{Annite}^{Bt} < 0.35$ , where  $X_{Annite}^{Bt} > 0.35$ ,  $D_{In}^{Bt/Melt}$  is  $< 1$  becoming  $\ll 1$  as  $D_{In}^{Bt/Melt}$  approaches  $X_{Annite}^{Bt} = 1$ . The reader can include any data points excluded from this regression to observe variations in this linear relationship if desired.

Table 9  
Composition of run product glass in Biotite Runs determined by Electron Microprobe Analysis (EPMA)

	<b>Biotite Run 1<sup>§</sup></b> (N=39)	<b>Biotite Run 4<sup>**</sup></b> (N=11)	<b>Biotite Run 8</b> (N=3)	<b>Biotite Run 11</b> (N=5)	<b>Biotite Run 12<sup>†</sup></b> (N=7)	<b>Biotite Run 13<sup>*</sup></b> (N=4)
<b>SiO<sub>2</sub></b>	74 ± 2	70.8 ± 0.2	68.8 ± 0.2	69.0 ± 0.5	69.9 ± 0.4	70.5 ± 0.4
<b>Al<sub>2</sub>O<sub>3</sub></b>	12 ± 1	13.8 ± 0.1	13.3 ± 0.4	13.5 ± 0.3	13.2 ± 0.3	13.2 ± 0.3
<b>TiO<sub>2</sub></b>	n.a.	n.a.	b.d.	0.07 ± 0.03	0.07 ± 0.02	0.05 ± 0.02
<b>FeO</b>	b.d.	0.64 ± 0.03	0.6 ± 0.1	0.5 ± 0.1	0.41 ± 0.04	0.39 ± 0.03
<b>MgO</b>	b.d.	0.11 ± 0.01	0.07 ± 0.04	0.11 ± 0.01	0.10 ± 0.01	0.13 ± 0.03
<b>MnO</b>	b.d.	0.05 ± 0.01	b.d.	b.d.	b.d.	0.12 ± 0.04
<b>CaO</b>	b.d.	0.41 ± 0.01	0.38 ± 0.01	0.54 ± 0.07	0.56 ± 0.05	0.56 ± 0.05
<b>Na<sub>2</sub>O</b>	3.48 ± 0.05	3.2 ± 0.1	3.2 ± 0.1	3.24 ± 0.09	3.35 ± 0.08	3.40 ± 0.09
<b>K<sub>2</sub>O</b>	4.6 ± 0.1	5.62 ± 0.02	5.91 ± 0.05	5.6 ± 0.1	5.4 ± 0.1	5.3 ± 0.2
<b>Cl</b>	b.d.	0.22 ± 0.01	0.26 ± 0.01	0.16 ± 0.02	0.16 ± 0.01	0.16 ± 0.02
<b>In<sub>2</sub>O<sub>3</sub></b>	0.046 ± 0.002	0.065 ± 0.004	0.09 ± 0.01	0.057 ± 0.004	0.046 ± 0.002	0.053 ± 0.002
<b>Total</b>	94.1 ± 2.1	94.9 ± 0.2	92.6 ± 0.5	92.7 ± 0.6	93.2 ± 0.5	93.8 ± 0.6
<b>In (ppm)</b>	380 ± 10	540 ± 30	720 ± 50	470 ± 30	380 ± 20	440 ± 20
<b>ASI</b>	1.1 ± 0.1	1.14 ± 0.02	1.07 ± 0.04	1.09 ± 0.05	1.07 ± 0.05	1.07 ± 0.05

All values in weight percent unless otherwise noted. ASI (Aluminum Saturation Index) is dimensionless and defined as the ratio of molar Al<sub>2</sub>O<sub>3</sub> to molar NaO + K<sub>2</sub>O + CaO.

\*Runs that did not exhibit new crystal growth and are excluded from plots

§Runs where starting biotite was the only reactant present

†Runs that exhibited weight loss after removal from furnace, but showed no immediate signs of failure

§Starting material glass was GR1 haplogranite

b.d. indicates below the detection of EPMA

n.a. is not analyzed

Table 9 continued

	<b>Biotite Run 15</b> (N=4)	<b>Biotite Run 20</b> (N=5)	<b>Biotite Run 21*</b> (N=5)	<b>Biotite Run 23</b> (N=8)	<b>Biotite Run 24</b> (N=6)	<b>Biotite Run 26</b> (N=7)
<b>SiO<sub>2</sub></b>	69.5 ± 0.5	70.9 ± 0.3	70.9 ± 0.6	70.9 ± 0.4	70.5 ± 0.5	69.7 ± 0.3
<b>Al<sub>2</sub>O<sub>3</sub></b>	14.0 ± 0.4	12.9 ± 0.4	13.4 ± 0.3	12.6 ± 0.3	12.4 ± 0.5	13.1 ± 0.3
<b>TiO<sub>2</sub></b>	0.06 ± 0.02	0.06 ± 0.03	b.d.	b.d.	0.049 ± 0.005	0.07 ± 0.01
<b>FeO</b>	0.4 ± 0.2	0.41 ± 0.08	0.44 ± 0.02	0.50 ± 0.04	0.55 ± 0.02	0.43 ± 0.02
<b>MgO</b>	0.05 ± 0.02	0.06 ± 0.01	0.09 ± 0.02	0.08 ± 0.01	0.08 ± 0.01	0.07 ± 0.01
<b>MnO</b>	0.10 ± 0.03	0.07 ± 0.03	b.d.	b.d.	b.d.	b.d.
<b>CaO</b>	0.62 ± 0.04	0.51 ± 0.02	0.65 ± 0.04	0.52 ± 0.03	0.52 ± 0.06	0.51 ± 0.04
<b>Na<sub>2</sub>O</b>	3.5 ± 0.1	3.54 ± 0.08	3.5 ± 0.1	3.4 ± 0.06	3.2 ± 0.1	3.82 ± 0.08
<b>K<sub>2</sub>O</b>	5.4 ± 0.1	5.0 ± 0.2	5.30 ± 0.06	4.9 ± 0.1	4.8 ± 0.1	5.5 ± 0.2
<b>Cl</b>	0.11 ± 0.01	0.19 ± 0.01	0.17 ± 0.01	0.17 ± 0.01	0.19 ± 0.01	0.17 ± 0.01
<b>In<sub>2</sub>O<sub>3</sub></b>	0.037 ± 0.002	0.058 ± 0.003	0.049 ± 0.002	0.047 ± 0.002	0.050 ± 0.004	0.030 ± 0.004
<b>Total</b>	93.9 ± 0.7	93.7 ± 0.5	94.5 ± 0.7	93.1 ± 0.5	92.4 ± 0.7	93.3 ± 0.5
<b>In (ppm)</b>	310 ± 20	480 ± 20	400 ± 20	390 ± 20	410 ± 30	250 ± 30
<b>ASI</b>	1.10 ± 0.04	1.10 ± 0.08	1.05 ± 0.04	1.07 ± 0.04	1.1 ± 0.1	0.99 ± 0.04

Table 9 continued

	<b>Biotite Run 27</b> (N=8)	<b>Biotite Run 28</b> (N=10)	<b>Biotite Run 29<sup>§</sup></b> (N=3)	<b>Biotite Run 31</b> (N=6)	<b>Biotite Run 32<sup>†</sup></b> (N=7)
<b>SiO<sub>2</sub></b>	73.5 ± 0.4	74.6 ± 0.3	67.8 ± 0.2	72 ± 1	73.5 ± 0.7
<b>Al<sub>2</sub>O<sub>3</sub></b>	14.1 ± 0.4	12.1 ± 0.2	13.4 ± 0.3	13.7 ± 0.4	13.2 ± 0.3
<b>TiO<sub>2</sub></b>	b.d.	b.d.	0.06 ± 0.02	0.06 ± 0.00	0.08 ± 0.01
<b>FeO</b>	0.61 ± 0.06	0.56 ± 0.02	0.35 ± 0.05	0.5 ± 0.1	0.47 ± 0.04
<b>MgO</b>	0.07 ± 0.01	0.10 ± 0.01	0.06 ± 0.01	0.07 ± 0.01	0.11 ± 0.01
<b>MnO</b>	b.d.	0.06 ± 0.01	b.d.	b.d.	b.d.
<b>CaO</b>	0.69 ± 0.07	0.43 ± 0.02	0.52 ± 0.04	0.54 ± 0.03	0.46 ± 0.07
<b>Na<sub>2</sub>O</b>	3.6 ± 0.1	3.04 ± 0.06	3.26 ± 0.02	3.4 ± 0.1	3.4 ± 0.1
<b>K<sub>2</sub>O</b>	5.09 ± 0.08	5.12 ± 0.05	5.7 ± 0.2	5.8 ± 0.2	5.2 ± 0.2
<b>Cl</b>	0.17 ± 0.01	0.22 ± 0.01	0.15 ± 0.01	0.17 ± 0.01	0.19 ± 0.01
<b>In<sub>2</sub>O<sub>3</sub></b>	0.056 ± 0.004	0.065 ± 0.002	0.049 ± 0.003	0.03 ± 0.00	0.018 ± 0.002
<b>Total</b>	97.9 ± 0.6	95.3 ± 0.4	91.4 ± 0.5	96.5 ± 0.7	96.6 ± 0.8
<b>In (ppm)</b>	470 ± 30	540 ± 10	400 ± 20	250 ± 40	150 ± 20
<b>ASI</b>	1.10 ± 0.05	1.07 ± 0.03	1.08 ± 0.04	1.07 ± 0.04	1.1 ± 0.1

Table 10

Composition of run product biotite determined by Electron Microprobe Analysis (EPMA)

	<b>Biotite Run 1</b> <sup>§</sup> (N=10)	<b>Biotite Run 4</b> <sup>**§</sup> (N=6)	<b>Biotite Run 8</b> (N=10)	<b>Biotite Run 11</b> (N=5)	<b>Biotite Run 12</b> <sup>**†</sup> (N=3)
SiO <sub>2</sub>	40.2 ± 0.2	25.9 ± 0.5	37.4 ± 0.2	38.9 ± 0.4	35.0 ± 0.7
Al <sub>2</sub> O <sub>3</sub>	14.4 ± 0.1	9.8 ± 0.2	14.3 ± 0.1	14.6 ± 0.1	10.9 ± 0.2
TiO <sub>2</sub>	2.7 ± 0.1	n.a.	2.7 ± 0.1	1.71 ± 0.07	0.9 ± 0.1
FeO	16.7 ± 0.1	6.5 ± 0.1	14.8 ± 0.2	13.6 ± 0.4	8.5 ± 0.4
MgO	14.3 ± 0.1	12.5 ± 0.3	14.0 ± 0.2	14.4 ± 0.9	18.3 ± 0.2
MnO	0.52 ± 0.04	b.d.	0.46 ± 0.01	0.42 ± 0.03	b.d. to 0.2
CaO	b.d.	b.d.	b.d.	b.d.	b.d.
Na <sub>2</sub> O	0.24 ± 0.01	0.38 ± 0.01	0.19 ± 0.01	0.27 ± 0.06	0.42 ± 0.04
K <sub>2</sub> O	9.4 ± 0.03	5.7 ± 0.1	9.7 ± 0.02	9.3 ± 0.2	8.36 ± 0.08
Cl	0.020 ± 0.003	0.13 ± 0.01	0.04 ± 0.01	0.23 ± 0.08	0.14 ± 0.02
In <sub>2</sub> O <sub>3</sub>	b.d.	0.24 ± 0.01	0.05 ± 0.01	0.29 ± 0.07	0.24 ± 0.02
<b>Total</b>	98.4 ± 0.3	61 ± 1	94 ± 0.3	94 ± 1	82.7 ± 0.9

<b>H<sub>2</sub>O</b>	4.13 ± 0.02	2.63 ± 0.05	3.92 ± 0.02	3.92 ± 0.03	3.5 ± 0.1
-----------------------	-------------	-------------	-------------	-------------	-----------

<b>In (ppm)</b>	20 ± 20	2000 ± 100	400 ± 100	2400 ± 600	2000 ± 200
-----------------	---------	------------	-----------	------------	------------

All values in weight percent unless otherwise noted. Uncertainties excluding Biotite Run 13 and 20 derived from counting statistics due to small sample size. Subpopulations are noted by [ ] and labeled in plots by value in [ ], see text for details. Indium concentrations for runs 1 and 13 were determined via LA-ICP-MS. Water calculated on the assumption of a filled hydroxyl site.

\* Runs that did not exhibit new crystal growth and excluded from plots

§Runs where starting biotite was the only reactant present

†Runs that exhibited weight loss after removal from furnace, but showed no immediate signs of failure

§Runs exhibiting weight gain due to metal precipitation on the capsule

\*\*Low total run is a result of small biotite grain size and inability to mount grain normal to electron beam

b.d. indicates below the detection of EPMA

n.a. is not analyzed

Indium concentrations for runs 1 and 13 were determined via LA-ICP-MS

Table 10 continued

	<b>Biotite Run 13* (N=2)</b>	<b>Biotite Run 15 [15.1] (N=3)</b>	<b>Biotite Run 15 [15.2] (N=4)</b>	<b>Biotite Run 20 (N=2)</b>	<b>Biotite Run 21* (N=4)</b>
<b>SiO<sub>2</sub></b>	34.9 ± 0.2	38.8 ± 0.4	43.5 ± 0.1	41.2 ± 0.3	37.0 ± 0.6
<b>Al<sub>2</sub>O<sub>3</sub></b>	12.9 ± 0.1	14.4 ± 0.3	12.8 ± 0.1	12.5 ± 0.1	14.0 ± 0.3
<b>TiO<sub>2</sub></b>	2.6 ± 0.1	2.7 ± 0.2	0.7 ± 0.1	0.31 ± 0.05	2.7 ± 0.2
<b>FeO</b>	17.1 ± 0.2	12.0 ± 0.6	8.0 ± 0.1	7.4 ± 0.2	15.8 ± 0.5
<b>MgO</b>	13.3 ± 0.1	17.1 ± 0.5	21.7 ± 0.2	22.1 ± 0.2	13.5 ± 0.5
<b>MnO</b>	0.6 ± 0.3	0.14 ± 0.02	0.07 ± 0.03	b.d.	0.53 ± 0.05
<b>CaO</b>	b.d.	b.d.	b.d.	b.d.	b.d.
<b>Na<sub>2</sub>O</b>	0.07 to 0.37	0.43 ± 0.01	0.41 ± 0.02	0.47 ± 0.04	0.11 ± 0.09
<b>K<sub>2</sub>O</b>	9.50 ± 0.06	8.7 ± 0.1	8.2 ± 0.1	7.30 ± 0.07	9.1 ± 0.1
<b>Cl</b>	0.02 to 0.12	0.29 ± 0.07	0.13 ± 0.01	0.11 ± 0.01	0.03 ± 0.01
<b>In<sub>2</sub>O<sub>3</sub></b>	b.d.	0.7 ± 0.10	0.27 ± 0.04	0.71 ± 0.01	b.d.
<b>Total</b>	91.0 ± 0.5	95 ± 1	95.7 ± 0.4	92.1 ± 0.4	93 ± 1
<b>H<sub>2</sub>O</b>	3.74 ± 0.09	4.00 ± 0.01	4.21 ± 0.01	4.05 ± 0.01	3.88 ± 0.07
<b>In (ppm)</b>	0.9 ± 0.2	5500 ± 800	2300 ± 400	5859 ± 5	b.d.

Table 10 continued

	<b>Biotite Run 23</b> <b>[23.1] (N=2)</b>	<b>Biotite Run 23</b> <b>[23.2] (N=3)</b>	<b>Biotite Run 23 [23.3]</b> <b>(N=3)</b>	<b>Biotite Run 24</b> <b>(N=4)</b>	<b>Biotite Run 26</b> <b>(N=4)</b>
<b>SiO<sub>2</sub></b>	38.7 ± 0.1	40.4 ± 0.1	39.4 ± 0.1	37.5 ± 0.9	42.2 ± 0.2
<b>Al<sub>2</sub>O<sub>3</sub></b>	13.91 ± 0.02	13.4 ± 0.2	14.32 ± 0.05	13.0 ± 0.3	12.78 ± 0.07
<b>TiO<sub>2</sub></b>	2.5 ± 0.1	1.4 ± 0.3	2.36 ± 0.03	2.0 ± 0.5	0.10 ± 0.03
<b>FeO</b>	14 ± 1	11 ± 1	15.1 ± 0.1	13 ± 1	7.87 ± 0.06
<b>MgO</b>	14.05 ± 0.03	18 ± 1	13.60 ± 0.09	16 ± 1	21.3 ± 0.4
<b>MnO</b>	0.46 ± 0.01	0.28 ± 0.04	0.35 ± 0.05	0.35 ± 0.08	b.d.
<b>CaO</b>	b.d.	b.d.	b.d.	b.d.	b.d.
<b>Na<sub>2</sub>O</b>	0.22 ± 0.03	0.38 ± 0.02	0.24 ± 0.01	0.33 ± 0.08	0.45 ± 0.01
<b>K<sub>2</sub>O</b>	8.7 ± 0.1	8.3 ± 0.2	8.78 ± 0.02	8.7 ± 0.2	8.35 ± 0.02
<b>Cl</b>	0.060 ± 0.002	0.10 ± 0.01	0.05 ± 0.01	0.09 ± 0.05	0.17 ± 0.03
<b>In<sub>2</sub>O<sub>3</sub></b>	0.2 ± 0.1	0.2 ± 0.0	0.029 ± 0.004	0.10 ± 0.05	0.49 ± 0.06
<b>Total</b>	93.3 ± 0.6	94 ± 1	94.2 ± 0.2	91 ± 2	93.8 ± 0.5

<b>H<sub>2</sub>O</b>	3.94 ± 0.02	4.04 ± 0.02	3.99 ± 0.01	3.86 ± 0.02	4.10 ± 0.03
-----------------------	-------------	-------------	-------------	-------------	-------------

<b>In (ppm)</b>	1600 ± 800	1600 ± 300	240 ± 30	900 ± 400	4100 ± 500
-----------------	------------	------------	----------	-----------	------------

Table 10 continued

	<b>Biotite Run 27</b> (N=6)	<b>Biotite Run 28</b> (N=11)	<b>Biotite Run 29<sup>s</sup></b> (N=9)	<b>Biotite Run 31</b> (N=9)	<b>Biotite Run 32<sup>t</sup></b> (N=10)
<b>SiO<sub>2</sub></b>	39.7 ± 0.2	40.7 ± 0.5	39.1 ± 0.3	37.6 ± 0.2	39.7 ± 0.4
<b>Al<sub>2</sub>O<sub>3</sub></b>	11.43 ± 0.09	12.2 ± 0.2	13.8 ± 0.1	13.91 ± 0.04	15.1 ± 0.2
<b>TiO<sub>2</sub></b>	0.22 ± 0.01	0.47 ± 0.04	2.82 ± 0.05	3.03 ± 0.02	0.55 ± 0.04
<b>FeO</b>	6.59 ± 0.1	6.99 ± 0.08	15.5 ± 0.2	15.7 ± 0.2	12.2 ± 0.2
<b>MgO</b>	22.6 ± 0.3	22.4 ± 0.2	13.0 ± 0.2	14.4 ± 0.2	18.6 ± 0.2
<b>MnO</b>	b.d.	b.d.	0.55 ± 0.01	0.42 ± 0.01	b.d.
<b>CaO</b>	0.1 ± 0.1	b.d.	b.d.	b.d.	b.d.
<b>Na<sub>2</sub>O</b>	0.51 ± 0.02	0.48 ± 0.01	0.17 ± 0.01	0.22 ± 0.02	0.49 ± 0.01
<b>K<sub>2</sub>O</b>	8.4 ± 0.06	8.54 ± 0.10	9.38 ± 0.03	9.59 ± 0.05	8.74 ± 0.03
<b>Cl</b>	0.115 ± 0.005	0.14 ± 0.01	0.018 ± 0.003	0.04 ± 0.01	0.28 ± 0.01
<b>In<sub>2</sub>O<sub>3</sub></b>	0.38 ± 0.03	0.43 ± 0.05	b.d.	0.06 ± 0.02	0.08 ± 0.01
<b>Total</b>	90.1 ± 0.4	92.4 ± 0.5	94.3 ± 0.4	95.0 ± 0.4	95.7 ± 0.5
<b>H<sub>2</sub>O</b>	3.94 ± 0.02	4.04 ± 0.03	3.97 ± 0.02	3.96 ± 0.01	4.05 ± 0.03
<b>In (ppm)</b>	3200 ± 200	3600 ± 400	b.d.	500 ± 200	650 ± 60

Table 11  
Formulas of biotite run products and starting material

Y-14 (Starting Biotite)		Biotite Run 1 <sup>§</sup>	Biotite Run 4 <sup>**§</sup>	Biotite Run 8	Biotite Run 11	Biotite Run 12 <sup>†</sup>	Biotite Run 13 <sup>*</sup>
Si	2.91 ± 0.01	2.91 ± 0.01	2.933 ± 0.003	2.85 ± 0.01	2.94 ± 0.03	2.93 ± 0.02	2.76 ± 0.04
Al	1.09 ± 0.01	1.09 ± 0.01	1.067 ± 0.003	1.15 ± 0.01	1.06 ± 0.03	1.07 ± 0.02	1.20 ± 0.03
Fe <sup>3+</sup>	-	-	-	-	-	-	0.03 ± 0.03
<b>Total</b>	4.00 ± 0.01	4.00 ± 0.01	4.000 ± 0.005	4.00 ± 0.01	4.00 ± 0.04	4.00 ± 0.02	4.00 ± 0.05
Al	0.15 ± 0.01	0.13 ± 0.01	0.24 ± 0.01	0.13 ± 0.01	0.24 ± 0.05	< 0.07	-
Ti	0.14 ± 0.01	0.148 ± 0.004	n.a.	0.154 ± 0.004	0.10 ± 0.00	0.06 ± 0.01	0.16 ± 0.02
Fe <sup>3+</sup>	0.05 ± 0.03	0.06 ± 0.01	-	< 0.14	-	< 0.15	0.25 ± 0.05
Fe <sup>2+</sup>	0.95 ± 0.01	0.94 ± 0.01	0.61 ± 0.01	0.89 ± 0.01	0.86 ± 0.03	0.5 ± 0.1	0.83 ± 0.08
Mg	1.52 ± 0.01	1.54 ± 0.01	2.10 ± 0.01	1.59 ± 0.02	1.6 ± 0.1	2.3 ± 0.1	1.6 ± 0.1
Mn	0.040 ± 0.001	0.032 ± 0.002	-	0.029 ± 0.001	0.027 ± 0.002	0.0 to 0.01	0.039 ± 0.006
In	-	-	0.012 ± 0.001	0.002 ± 0.001	0.010 ± 0.002	0.009 ± 0.002	-
<b>Total</b>	2.86 ± 0.04	2.85 ± 0.02	2.97 ± 0.02	2.80 ± 0.02	2.9 ± 0.1	2.8 ± 0.2	2.8 ± 0.2
K	0.86 ± 0.03	0.86 ± 0.01	0.82 ± 0.02	0.939 ± 0.004	0.89 ± 0.02	0.89 ± 0.02	0.96 ± 0.02
Ca	-	-	-	-	-	-	-
Na	0.025 ± 0.005	0.034 ± 0.002	0.083 ± 0.002	0.028 ± 0.001	0.04 ± 0.01	0.07 ± 0.01	0.01 ± 0.01
<b>Total</b>	0.89 ± 0.03	0.90 ± 0.01	0.90 ± 0.02	0.97 ± 0.00	0.93 ± 0.02	0.96 ± 0.02	0.97 ± 0.02
Cl	0.003 ± 0.001	0.002 ± 0.001	0.024 ± 0.002	0.006 ± 0.001	0.03 ± 0.01	0.019 ± 0.009	0.004 ± 0.007
OH	1.997 ± 0.001	1.998 ± 0.001	1.976 ± 0.002	1.994 ± 0.001	1.97 ± 0.01	1.981 ± 0.009	1.996 ± 0.007
X <sub>Ann</sub>	0.33 ± 0.01	0.330 ± 0.004	0.21 ± 0.01	0.31 ± 0.01	0.30 ± 0.01	0.17 ± 0.03	0.29 ± 0.03

Formulas calculated by the method of Dymek (1983). Subpopulations are noted by [ ] and labeled in plots by value in [ ], see text for details.

\*Runs that did not exhibit new crystal growth and excluded from plots

§Runs where starting biotite was the only reactant present

†Runs that exhibited weight loss after removal from furnace, but showed no immediate signs of failure

Dashed line indicates that cation below detection or not analyzed.

Table 11 continued

	<b>Biotite Run 15.1</b>	<b>Biotite Run 15.2</b>	<b>Biotite Run 20</b>	<b>Biotite Run 21 *</b>	<b>Biotite Run 23.1</b>	<b>Biotite Run 23.2</b>	<b>Biotite Run 23.3</b>
<b>Si</b>	2.84 ± 0.04	3.08 ± 0.01	3.02 ± 0.02	2.84 ± 0.01	2.93 ± 0.01	2.98 ± 0.01	2.95 ± 0.01
<b>Al</b>	1.16 ± 0.04	0.92 ± 0.01	0.98 ± 0.02	1.16 ± 0.01	1.07 ± 0.01	1.02 ± 0.01	1.05 ± 0.01
<b>Fe<sup>3+</sup></b>	-	-	-	-	-	-	-
<b>Total</b>	4.00 ± 0.06	4.00 ± 0.02	4.00 ± 0.02	4.00 ± 0.02	4.00 ± 0.03	4.00 ± 0.03	4.00 ± 0.01
<b>Al</b>	0.08 ± 0.02	0.15 ± 0.02	0.09 ± 0.03	0.11 ± 0.02	0.17 ± 0.01	0.14 ± 0.01	0.22 ± 0.01
<b>Ti</b>	0.15 ± 0.02	0.03 ± 0.01	0.017 ± 0.001	0.16 ± 0.01	0.144 ± 0.004	0.08 ± 0.02	0.133 ± 0.002
<b>Fe<sup>3+</sup></b>	0.17 ± 0.08	-	0.12 ± 0.04	0.14 ± 0.03	0.01 to 0.04	0.03 ± 0.02	-
<b>Fe<sup>2+</sup></b>	0.56 ± 0.08	0.47 ± 0.01	0.33 ± 0.04	0.87 ± 0.02	0.90 ± 0.01	0.65 ± 0.06	0.95 ± 0.01
<b>Mg</b>	1.9 ± 0.1	2.29 ± 0.02	2.41 ± 0.03	1.55 ± 0.03	1.587 ± 0.005	1.98 ± 0.09	1.52 ± 0.01
<b>Mn</b>	0.01 ± 0.001	0.004 ± 0.002	-	0.035 ± 0.002	0.029 ± 0.001	0.018 ± 0.002	0.023 ± 0.003
<b>In</b>	0.02 ± 0.01	0.008 ± 0.001	0.022 ± 0.001	-	0.006 ± 0.003	0.006 ± 0.001	0.0010 ± 0.0001
<b>Total</b>	2.9 ± 0.2	2.96 ± 0.03	2.98 ± 0.07	2.8 ± 0.1	2.9 ± 0.3	2.9 ± 0.3	2.84 ± 0.01
<b>K</b>	0.81 ± 0.04	0.74 ± 0.01	0.681 ± 0.001	0.895 ± 0.004	0.842 ± 0.002	0.78 ± 0.01	0.840 ± 0.001
<b>Ca</b>	-	-	-	-	-	-	-
<b>Na</b>	0.061 ± 0.01	0.056 ± 0.003	0.067 ± 0.002	0.02 ± 0.01	0.033 ± 0.005	0.054 ± 0.003	0.036 ± 0.002
<b>Total</b>	0.87 ± 0.04	0.79 ± 0.01	0.748 ± 0.001	0.92 ± 0.00	0.86 ± 0.03	0.86 ± 0.03	0.876 ± 0.001
<b>Cl</b>	0.04 ± 0.02	0.015 ± 0.002	0.014 ± 0.002	0.004 ± 0.001	0.008 ± 0.001	0.013 ± 0.001	0.006 ± 0.001
<b>OH</b>	1.96 ± 0.01	1.985 ± 0.002	1.986 ± 0.002	1.996 ± 0.001	1.992 ± 0.001	1.987 ± 0.001	1.994 ± 0.001
<b>X<sub>Ann</sub></b>	0.19 ± 0.001	0.160 ± 0.003	0.11 ± 0.01	0.31 ± 0.01	0.316 ± 0.005	0.22 ± 0.02	0.333 ± 0.003

Table 11 continued

	<b>Biotite Run 24</b>	<b>Biotite Run 26</b>	<b>Biotite Run 27</b>	<b>Biotite Run 28</b>	<b>Biotite Run 29<sup>§</sup></b>	<b>Biotite Run 31</b>	<b>Biotite Run 32<sup>F</sup></b>
<b>Si</b>	2.88 ± 0.03	0.16 ± 0.01	3.00 ± 0.02	3.00 ± 0.01	2.95 ± 0.01	2.82 ± 0.01	2.89 ± 0.01
<b>Al</b>	1.12 ± 0.03	0.01 ± 0.01	1.00 ± 0.01	1.00 ± 0.01	1.05 ± 0.01	1.18 ± 0.01	1.11 ± 0.01
<b>Fe<sup>3+</sup></b>	-	-	-	-	-	-	-
<b>Total</b>	4.00 ± 0.04	0.16 ± 0.02	4.00 ± 0.02	4.00 ± 0.02	4.00 ± 0.02	4.00 ± 0.01	4.00 ± 0.01
<b>Al</b>	0.05 ± 0.02	0.16 ± 0.02	< 0.08	0.05 ± 0.01	0.18 ± 0.02	0.05 ± 0.01	0.18 ± 0.01
<b>Ti</b>	0.11 ± 0.01	0.006 ± 0.002	0.013 ± 0.001	0.026 ± 0.002	0.160 ± 0.003	0.170 ± 0.001	0.03 ± 0.002
<b>Fe<sup>3+</sup></b>	0.16 ± 0.04	-	0.07 ± 0.02	0.07 ± 0.02	-	0.18 ± 0.02	0.05 ± 0.01
<b>Fe<sup>2+</sup></b>	0.66 ± 0.02	0.477 ± 0.003	0.34 ± 0.04	0.36 ± 0.01	0.98 ± 0.01	0.80 ± 0.02	0.69 ± 0.02
<b>Mg</b>	1.88 ± 0.06	2.31 ± 0.04	2.54 ± 0.03	2.46 ± 0.01	1.46 ± 0.02	1.61 ± 0.02	2.01 ± 0.02
<b>Mn</b>	0.023 ± 0.003	-	-	-	0.035 ± 0.001	0.026 ± 0.001	-
<b>In</b>	0.003 ± 0.001	0.015 ± 0.002	0.012 ± 0.001	0.014 ± 0.002	-	0.002 ± 0.001	0.002 ± 0.001
<b>Total</b>	2.9 ± 0.1	2.96 ± 0.04	2.98 ± 0.05	2.97 ± 0.03	2.81 ± 0.03	2.83 ± 0.03	3.0 ± 0.03
<b>K</b>	0.85 ± 0.02	0.77 ± 0.01	0.804 ± 0.005	0.80 ± 0.01	0.904 ± 0.003	0.92 ± 0.01	0.81 ± 0.01
<b>Ca</b>	-	-	-	-	-	-	-
<b>Na</b>	0.05 ± 0.01	0.063 ± 0.003	0.07 ± 0.003	0.069 ± 0.001	0.025 ± 0.001	0.031 ± 0.003	0.069 ± 0.001
<b>Total</b>	0.90 ± 0.02	0.84 ± 0.01	0.88 ± 0.01	0.87 ± 0.01	0.929 ± 0.003	0.95 ± 0.01	0.88 ± 0.01
<b>Cl</b>	0.012 ± 0.003	0.021 ± 0.004	0.015 ± 0.001	0.017 ± 0.001	0.002 ± 0.001	0.005 ± 0.001	0.034 ± 0.001
<b>OH</b>	1.988 ± 0.003	1.979 ± 0.004	1.985 ± 0.001	1.983 ± 0.001	1.998 ± 0.001	1.995 ± 0.001	1.966 ± 0.001
<b>X<sub>Ann</sub></b>	0.23 ± 0.01	0.161 ± 0.001	0.11 ± 0.01	0.121 ± 0.005	0.348 ± 0.004	0.28 ± 0.01	0.23 ± 0.01

Table 12

Run conditions and partition coefficients of biotite runs

Run	Temperature (°C)	Run Duration (Hours)	Partition Coefficient (Biotite/Melt)
<b>Biotite Run 1<sup>§</sup></b>	800	320	n.d.
<b>Biotite Run 4</b>	800	165	3.6 ± 0.3
<b>Biotite Run 8</b>	800	174	0.6 ± 0.1
<b>Biotite Run 11</b>	750	166	5 ± 1
<b>Biotite Run 12<sup>†</sup></b>	750	334	5.1 ± 0.6
<b>Biotite Run 13*</b>	750	336	n.d.
<b>Biotite Run 15 [15.1]</b>	750	336	18 ± 3
<b>Biotite Run 15 [15.2]</b>	750	336	7 ± 1
<b>Biotite Run 20</b>	750	672	12.3 ± 0.6
<b>Biotite Run 21*</b>	750	672	n.d.
<b>Biotite Run 23 [23.1]</b>	750	504	4 ± 2
<b>Biotite Run 23 [23.2]</b>	750	504	4.0 ± 0.8
<b>Biotite Run 23 [23.3]</b>	750	504	0.62 ± 0.09
<b>Biotite Run 24</b>	750	504	2 ± 1
<b>Biotite Run 26</b>	750	1008	16 ± 3
<b>Biotite Run 27</b>	750	1344	6.8 ± 0.6
<b>Biotite Run 28</b>	750	1008	6.6 ± 0.7
<b>Biotite Run 29<sup>§</sup></b>	750	336	n.d.
<b>Biotite Run 31</b>	750	504	2.0 ± 0.9
<b>Biotite Run 32</b>	750	1008	4.3 ± 0.6

\*Runs did not exhibit new crystal growth and excluded from plots

<sup>§</sup>Runs where starting biotite was the only reactant present<sup>†</sup>Runs that exhibited weight loss after removal from furnace, but showed no immediate signs of failure  
Pressure of all runs is 100 MPa.

n.d. is not determined.

Subpopulations are noted by [ ] and labeled in plots by value in [ ], see text for details.

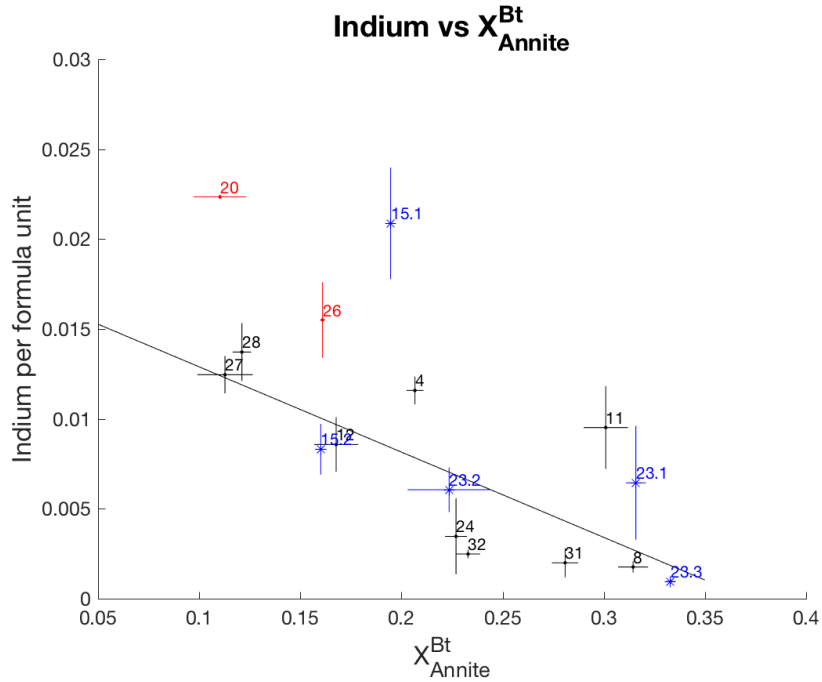


Figure 6: Indium per formula unit vs. mole fraction of annite of experimentally grown biotite. Only runs that show evidence of new biotite growth have been plotted (see Table 10). Biotite formulas calculated according to the method of Dymek (1983). Error bars are standard deviations from the mean ( $1\sigma_m$ ). Numbers corresponds to run number in Table 10. Data points plotted in red are experiments that fall off the trend of plots of partition coefficients (Figures below) and excluded from linear regressions. Blue data points indicate subpopulations excluded from all regressions.

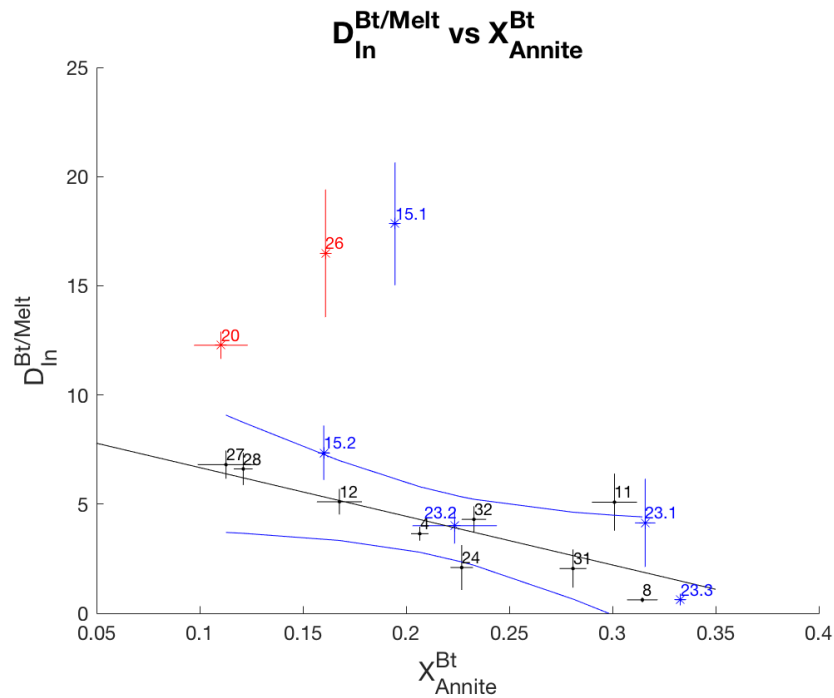


Figure 7: Partition coefficients for indium between biotite/melt vs. mole fraction of annite of experimentally grown biotite. Blue lines represent the 95% confidence envelope. See Figure 6 caption for additional details.

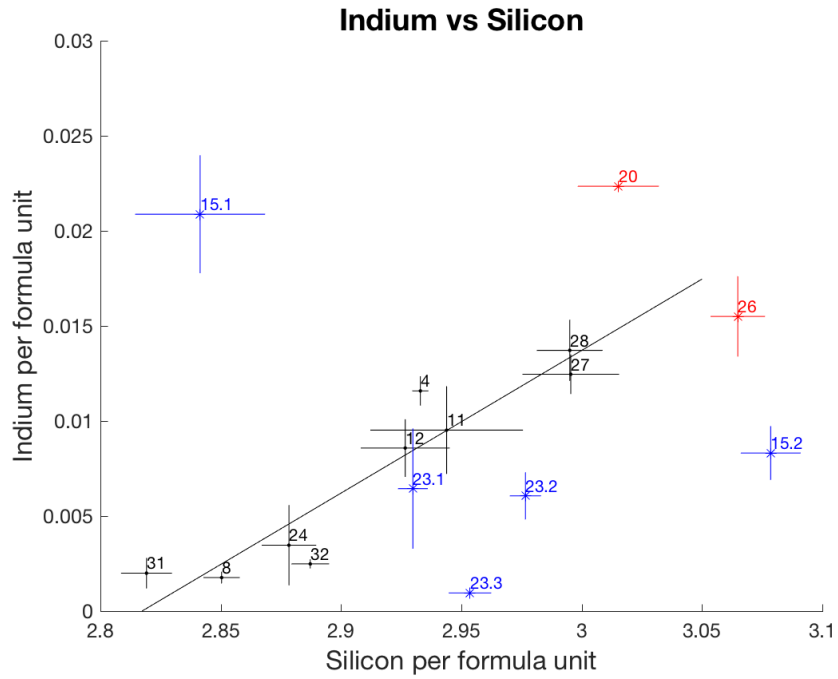


Figure 8: Indium per formula unit vs. silicon per formula unit of experimentally grown biotite. See Figure 6 caption for additional details.

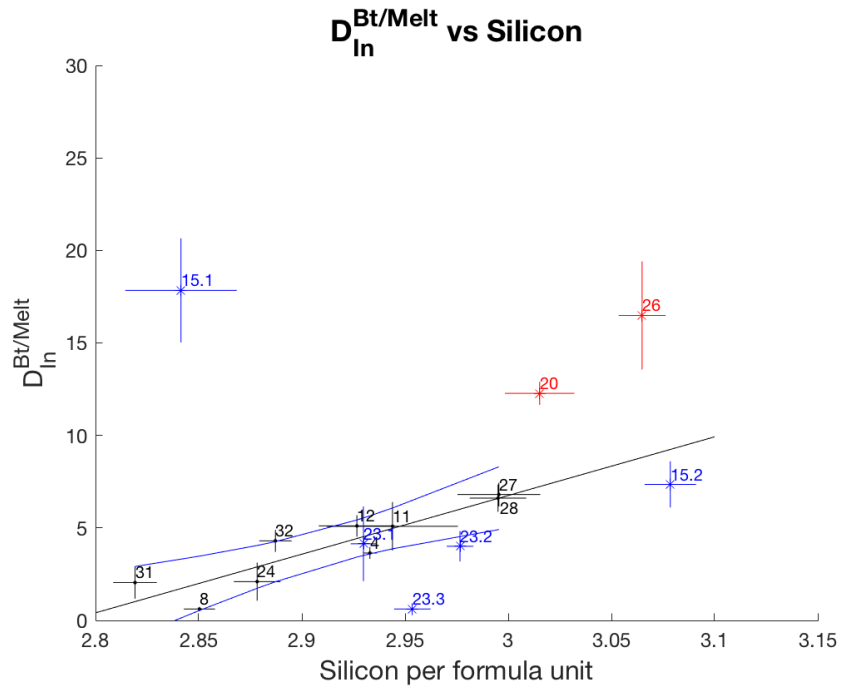


Figure 9: Partition coefficients for indium between biotite/melt vs. silicon per formula unit of experimentally grown biotite. Blue lines represent the 95% confidence envelope. See Figure 6 caption for additional details.

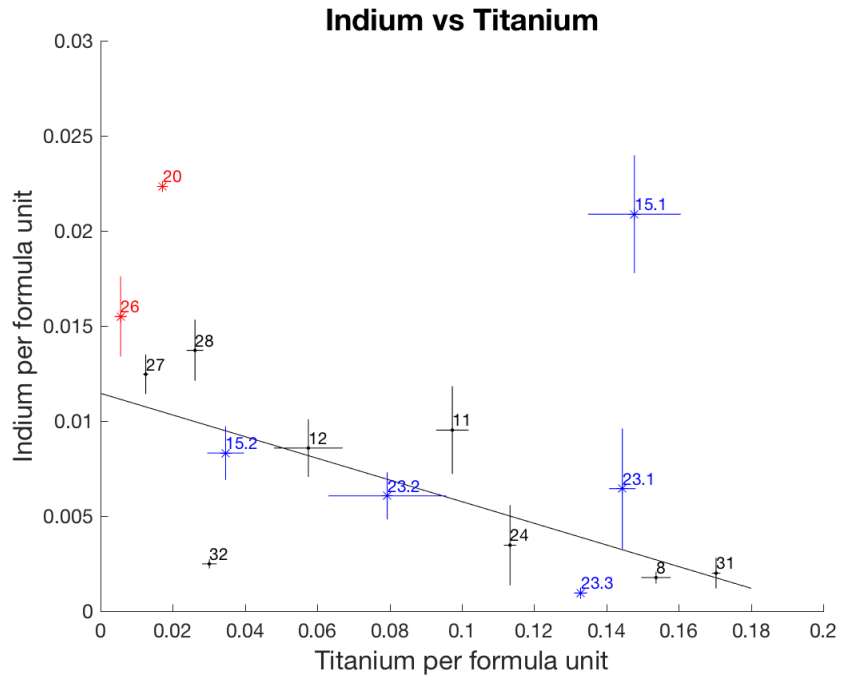


Figure 10: Indium per formula unit vs. titanium per formula unit of experimentally grown biotite. See Figure 6 caption for additional details.

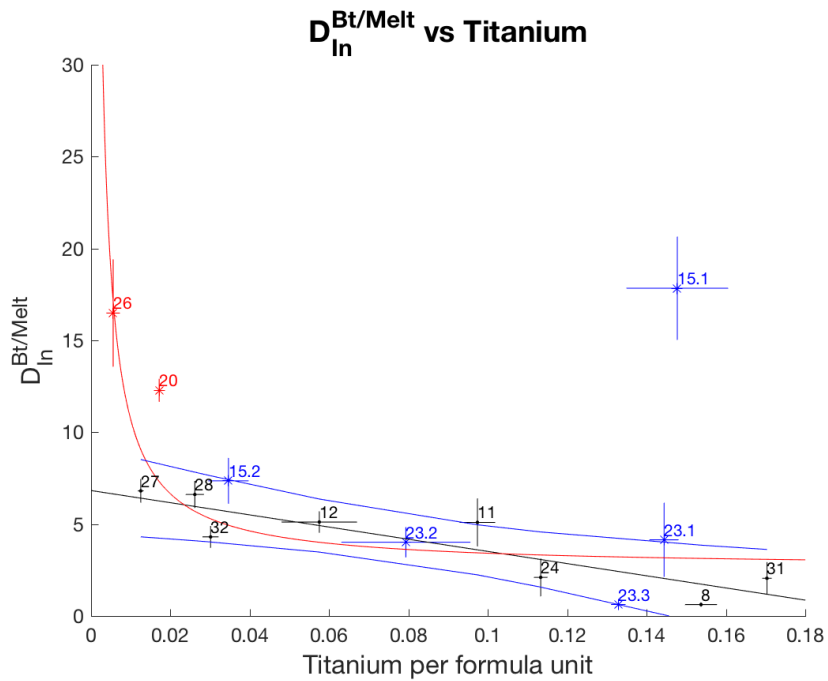


Figure 11: Partition coefficients for indium between biotite/melt vs. titanium per formula unit of experimentally grown biotite. Blue lines represent the 95% confidence envelope for linear regression. Regression in red represents the non linear relationship of the partition coefficient and titanium as titanium approaches zero. See Figure 6 caption for additional details.

#### 4.2. Amphibole/Melt Experiments

Nine experiments that resulted in the nucleation and growth of amphibole were deemed successful. Eight of these experiments were seeded with Half Dome Granodiorite amphibole and one was unseeded. Three experiments (Amphibole Run 8, 10, and 14) experienced a weight loss of >2 mg (relative to total mass) due to the loss of aqueous chloride solution and were deemed to have failed upon quench. It should be noted that the three experiments that experienced failure on quench had run times of greater than 1000 hrs. Additionally, these experiments also produced high-Ni biotite. Elevated nickel in biotite may indicate failure during the run; however, significant Ni was not detected in run product glasses or in amphibole. In addition these experiments are consistent with trends exhibited by other amphibole experiments. Similar to biotite experiments, red rhombohedral flakes of hematite were grown in one amphibole experiment. In-silicate was grown in four experiments. In an additional three experiments In-silicate crystals were not confirmed, but small crystals were suspected to have grown based on optical observations.

The compositions of run product glass from amphibole experiments are reported in Table 13. The run product glasses have a mean ASI of  $1.05 \pm 0.02$  ( $1\sigma_m$ ). Run product amphibole compositions are reported in Table 14 and are nominally hornblende (Table 15).  $D_{in}^{Am/Melt}$  ranges from 25 to 50, with a mean of  $36 \pm 4$  ( $1\sigma_m$ ) (Table 16). In three experiments subpopulations of amphibole were present, two populations in Amphibole Run 6 (labeled 6.1 and 6.2), four populations in Amphibole Run 11 (labeled 11.1, 11.2, 11.3, 11.4), and two populations in Amphibole Run 14 (labeled 14.1 and 14.2). Similar to biotite experiments, these populations show

significant variation in amphibole composition within their respective runs, indicating disequilibrium. Experiments with subpopulations have been plotted in all figures but have been excluded from the computation of any average or range. The reader can add these experiments to calculations if desired. When examining plots of amphibole composition trends are apparent if subpopulations are included. The strongest correlation is between In p.f.u. and tetrahedral Al p.f.u (Figure 12), and a moderate correlation between In p.f.u and Ti, K+Na, and Fe p.f.u, respectively, where formulas are calculated by the method of Hawthorne et al. (2012) (Figures 13-15). These relationships result in a correlation between  $D_{\text{In}}^{\text{Am/Melt}}$  and Al, Ti, and K+Na p.f.u (Figures 16-18), but not between  $D_{\text{In}}^{\text{Am/Melt}}$  and Fe p.f.u. (Figure 19). Although these trends are present when subpopulations are included, the trends are weak to non-existent when examining the data that excludes the subpopulations.

Table 13  
Composition of glass run products in Amphibole Runs determined by Electron Microprobe Analysis (EPMA)

	Amphibole Run 4 (N=11)	Amphibole Run 6 (N=7)	Amphibole Run 7 (N=9)	Amphibole Run 8 <sup>†</sup> (N=7)	Amphibole Run 9 (N=9)
SiO <sub>2</sub>	67.4 ± 0.3	68.4 ± 0.4	71.6 ± 0.3	72.5 ± 0.3	71.3 ± 0.5
Al <sub>2</sub> O <sub>3</sub>	12.8 ± 0.3	13.7 ± 0.6	13.3 ± 0.3	12.47 ± 0.08	13.5 ± 0.4
TiO <sub>2</sub>	0.08 ± 0.01	0.11 ± 0.02	0.08 ± 0.01	0.09 ± 0.01	0.09 ± 0.01
FeO	0.66 ± 0.02	0.59 ± 0.02	0.69 ± 0.01	0.77 ± 0.03	0.61 ± 0.02
MgO	0.11 ± 0.01	0.10 ± 0.01	0.13 ± 0.01	0.08 ± 0.01	0.11 ± 0.01
MnO	b.d.	b.d.	b.d.	b.d.	b.d.
CaO	1.2 ± 0.1	1.4 ± 0.3	1.3 ± 0.1	1.05 ± 0.04	1.14 ± 0.1
Na <sub>2</sub> O	2.6 ± 0.2	3.5 ± 0.2	2.94 ± 0.07	2.96 ± 0.06	3.0 ± 0.1
K <sub>2</sub> O	5.0 ± 0.1	5.3 ± 0.2	5.5 ± 0.1	5.01 ± 0.04	5.6 ± 0.1
Cl	0.29 ± 0.01	0.29 ± 0.02	0.30 ± 0.01	0.32 ± 0.01	0.30 ± 0.01
In <sub>2</sub> O <sub>3</sub>	0.08 ± 0.01	0.09 ± 0.01	0.108 ± 0.004	0.052 ± 0.003	0.088 ± 0.005
<b>Total</b>	<b>90.2 ± 0.5</b>	<b>93.4 ± 0.8</b>	<b>95.9 ± 0.4</b>	<b>95.4 ± 0.3</b>	<b>95.8 ± 0.6</b>
<b>In (ppm)</b>	<b>670 ± 80</b>	<b>750 ± 50</b>	<b>900 ± 40</b>	<b>430 ± 20</b>	<b>730 ± 40</b>
<b>ASI</b>	<b>1.08 ± 0.05</b>	<b>0.98 ± 0.1</b>	<b>1.02 ± 0.04</b>	<b>1.02 ± 0.02</b>	<b>1.03 ± 0.05</b>

All values in weight percent unless otherwise noted. ASI (Aluminum Saturation Index) is dimensionless and defined as the ratio of molar Al<sub>2</sub>O<sub>3</sub> to molar Na<sub>2</sub>O + K<sub>2</sub>O + CaO.

<sup>†</sup>Runs that exhibited weight loss after removal from furnace, but showed no immediate signs of failure  
b.d. indicates below the detection of EPMA

Table 13 continued

	Amphibole Run 10 <sup>F</sup> (N=9)	Amphibole Run 11 (N=7)	Amphibole Run 13 (N=9)	Amphibole Run 14 <sup>F</sup> (N=5)
SiO <sub>2</sub>	68.5 ± 0.3	68.3 ± 0.3	68.7 ± 0.2	67.6 ± 0.4
Al <sub>2</sub> O <sub>3</sub>	12.4 ± 0.3	13.4 ± 0.2	12.8 ± 0.2	13.5 ± 0.1
TiO <sub>2</sub>	0.12 ± 0.01	0.07 ± 0.01	0.07 ± 0.01	0.04 ± 0.01
FeO	0.73 ± 0.02	0.59 ± 0.02	0.60 ± 0.02	0.67 ± 0.04
MgO	0.10 ± 0.01	0.08 ± 0.01	0.06 ± 0.01	0.05 ± 0.01
MnO	b.d.	b.d.	b.d.	b.d.
CaO	1.4 ± 0.2	1.1 ± 0.1	1.05 ± 0.06	0.55 ± 0.01
Na <sub>2</sub> O	3.0 ± 0.1	2.81 ± 0.04	2.73 ± 0.07	2.96 ± 0.02
K <sub>2</sub> O	4.5 ± 0.1	5.15 ± 0.05	5.00 ± 0.05	5.38 ± 0.06
Cl	0.32 ± 0.01	0.38 ± 0.02	0.33 ± 0.01	0.05 ± 0.01
In <sub>2</sub> O <sub>3</sub>	0.032 ± 0.002	0.099 ± 0.002	0.085 ± 0.003	0.020 ± 0.001
Total	91.0 ± 0.5	92.0 ± 0.4	91.4 ± 0.3	90.9 ± 0.4
In (ppm)	270 ± 10	820 ± 20	710 ± 20	170 ± 10
ASI	1.01 ± 0.05	1.10 ± 0.04	1.09 ± 0.03	1.16 ± 0.02

Table 14  
Composition of amphibole run products determined by Electron Microprobe Analysis (EPMA)

	Amphibole Run 4 (N=4)	Amphibole Run 6 [6.1] (N=4)	Amphibole Run 6 [6.2] (N=9)	Amphibole Run 7 (N=8)	Amphibole Run 8 <sup>F</sup> (N=6)
SiO <sub>2</sub>	46 ± 2	46.0 ± 0.8	42.7 ± 0.4	42.9 ± 0.5	44.9 ± 0.2
Al <sub>2</sub> O <sub>3</sub>	9.6 ± 0.3	5.33 ± 0.08	8.5 ± 0.1	8.95 ± 0.08	8.32 ± 0.07
TiO <sub>2</sub>	1.2 ± 0.1	0.62 ± 0.02	1.31 ± 0.04	1.13 ± 0.03	1.30 ± 0.06
FeO	9.5 ± 0.6	12.15 ± 0.07	11.1 ± 0.6	8.64 ± 0.09	12.4 ± 0.2
MgO	10.1 ± 0.9	13.7 ± 0.2	12.8 ± 0.5	14.20 ± 0.07	10.0 ± 0.2
MnO	0.21 ± 0.04	0.62 ± 0.05	0.31 ± 0.02	0.25 ± 0.04	0.27 ± 0.03
CaO	9.2 ± 0.7	10.68 ± 0.11	11.5 ± 0.3	11.4 ± 0.2	11.42 ± 0.06
Na <sub>2</sub> O	1.4 ± 0.1	0.94 ± 0.03	1.36 ± 0.07	1.51 ± 0.03	1.35 ± 0.02
K <sub>2</sub> O	1.5 ± 0.2	0.43 ± 0.01	0.94 ± 0.05	1.05 ± 0.02	0.90 ± 0.02
Cl	0.26 ± 0.02	0.016 ± 0.005	0.23 ± 0.02	0.23 ± 0.05	0.40 ± 0.01
In <sub>2</sub> O <sub>3</sub>	2.4 ± 0.3	0.012 ± 0.003	3.2 ± 0.2	2.8 ± 0.1	1.47 ± 0.07
Total	91 ± 2	90.5 ± 0.9	94 ± 1.0	93.0 ± 0.6	92.7 ± 0.4
H <sub>2</sub> O	1.64 ± 0.04	1.83 ± 0.02	1.63 ± 0.01	1.66 ± 0.02	1.59 ± 0.01
In (ppm)	20,000 ± 2,000	100 ± 30	26,000 ± 1,000	23,100 ± 600	12,200 ± 600

All values in weight percent unless otherwise noted. Uncertainties excluding Amphibole 11.3, 11.4, and 14.2 are derived from counting statistics due to small sample size.

<sup>F</sup>Runs that exhibited weight loss after removal from furnace, but showed no immediate signs of failure. Subpopulations are noted by [ ] labeled in plots by value in [ ], see text for details.

Water calculated on assumption of a filled hydroxyl site.

Table 14 continued

	Amphibole Run 9 (N=7)	Amphibole Run 10 <sup>F</sup> (N=8)	Amphibole Run 11 [11.1] (N=3)	Amphibole Run 11 [11.2] (N=5)	Amphibole Run 11 [11.3] (N=1)
SiO <sub>2</sub>	44.3 ± 0.4	45.1 ± 0.2	47.9 ± 0.3	46.4 ± 0.9	43.8 ± 0.2
Al <sub>2</sub> O <sub>3</sub>	9.2 ± 0.1	8.43 ± 0.08	4.8 ± 0.7	5.4 ± 0.2	5.0 ± 0.1
TiO <sub>2</sub>	1.42 ± 0.03	1.74 ± 0.03	0.5 ± 0.2	0.70 ± 0.08	0.67 ± 0.04
FeO	10.00 ± 0.09	12.6 ± 0.1	13.1 ± 0.7	13.7 ± 0.2	13.5 ± 0.2
MgO	14.47 ± 0.08	11.9 ± 0.1	14.1 ± 0.5	13.2 ± 0.5	13.0 ± 0.1
MnO	0.25 ± 0.02	0.28 ± 0.02	0.65 ± 0.06	0.54 ± 0.08	0.6 ± 0.1
CaO	12.18 ± 0.05	11.0 ± 0.1	11.7 ± 0.1	11.6 ± 0.1	11.50 ± 0.08
Na <sub>2</sub> O	1.53 ± 0.02	1.46 ± 0.02	0.80 ± 0.06	0.92 ± 0.04	0.84 ± 0.03
K <sub>2</sub> O	1.01 ± 0.02	0.81 ± 0.01	0.40 ± 0.06	0.47 ± 0.02	0.51 ± 0.02
Cl	0.18 ± 0.01	0.26 ± 0.01	0.09 ± 0.04	0.13 ± 0.05	0.06 ± 0.01
In <sub>2</sub> O <sub>3</sub>	3.49 ± 0.04	1.32 ± 0.09	0.04 ± 0.01	0.6 ± 0.1	1.62 ± 0.01
Total	98.0 ± 0.5	94.9 ± 0.3	94 ± 1	94 ± 1	91.1 ± 0.3
H <sub>2</sub> O	1.70 ± 0.02	1.58 ± 0.01	1.902 ± 0.003	1.8 ± 0.1	1.8 ± 0.2
In (ppm)	29,000 ± 400	11,000 ± 800	300 ± 60	5,000 ± 1,000	13,480 ± 50

Table 14 continued

	Amphibole Run 11 [11.4] (N=1)	Amphibole Run 13 (N=9)	Amphibole Run 14 [14.1] <sup>F</sup> (N=6)	Amphibole Run 14 [14.2] <sup>F</sup> (N=1)
SiO <sub>2</sub>	42.0 ± 0.2	42.6 ± 0.3	44.0 ± 0.3	47.3 ± 0.2
Al <sub>2</sub> O <sub>3</sub>	7.9 ± 0.1	8.8 ± 0.1	7.7 ± 0.2	5.6 ± 0.1
TiO <sub>2</sub>	1.40 ± 0.05	1.62 ± 0.07	1.40 ± 0.06	0.70 ± 0.04
FeO	12.5 ± 0.2	11.4 ± 0.2	13.0 ± 0.1	14.0 ± 0.2
MgO	13.2 ± 0.1	12.2 ± 0.3	13.3 ± 0.3	13.4 ± 0.1
MnO	0.27 ± 0.06	0.30 ± 0.02	0.29 ± 0.02	0.59 ± 0.07
CaO	11.6 ± 0.1	11.11 ± 0.08	10.9 ± 0.1	11.7 ± 0.1
Na <sub>2</sub> O	1.27 ± 0.04	1.43 ± 0.05	1.11 ± 0.06	0.88 ± 0.03
K <sub>2</sub> O	0.77 ± 0.03	0.96 ± 0.02	0.50 ± 0.01	0.38 ± 0.02
Cl	0.21 ± 0.01	0.26 ± 0.01	0.18 ± 0.01	0.04 ± 0.01
In <sub>2</sub> O <sub>3</sub>	3.32 ± 0.01	4.2 ± 0.1	1.97 ± 0.06	0.11 ± 0.01
Total	94.4 ± 0.3	94.9 ± 0.5	94.4 ± 0.4	94.7 ± 0.3
H <sub>2</sub> O	1.6	1.56 ± 0.01	1.65 ± 0.01	1.88 ± 0.01
In (ppm)	27,500 ± 100	35,000 ± 1,000	16,300 ± 500	940 ± 40

Table 15

Formulas of run product amphiboles and starting materials

	Half Dome Amphibole	Amphibole Run 4	Amphibole Run 6 [6.1]	Amphibole Run 6 [6.2]	Amphibole Run 7	Amphibole Run 8 <sup>†</sup>
<b>Si</b>	7.34 ± 0.01	7.2 ± 0.2	7.24 ± 0.08	6.66 ± 0.05	6.66 ± 0.04	7.00 ± 0.02
<b>Al</b>	0.66 ± 0.01	0.8 ± 0.2	0.76 ± 0.08	1.34 ± 0.05	1.34 ± 0.04	1.00 ± 0.02
<b>Total</b>	8.00 ± 0.02	8.0 ± 0.3	8.0 ± 0.1	8.0 ± 0.1	8.0 ± 0.1	8.00 ± 0.04
<b>Al</b>	0.30 ± 0.04	0.9 ± 0.3	0.23 ± 0.06	0.21 ± 0.05	0.29 ± 0.03	0.53 ± 0.02
<b>Ti</b>	0.069 ± 0.001	0.14 ± 0.01	0.073 ± 0.002	0.153 ± 0.004	0.132 ± 0.003	0.15 ± 0.01
<b>Fe<sup>3+</sup></b>	0.004 ± 0.001	0.07 ± 0.01	< 0.45	< 0.49	0.06 ± 0.01	0.105 ± 0.005
<b>Fe<sup>2+</sup></b>	1.6 ± 0.02	1.17 ± 0.08	1.59 ± 0.09	1.4 ± 0.1	1.06 ± 0.01	1.52 ± 0.02
<b>Mg</b>	3.0 ± 0.03	2.3 ± 0.2	3.21 ± 0.07	3.0 ± 0.1	3.28 ± 0.03	2.33 ± 0.04
<b>Mn</b>	0.076 ± 0.001	0.03 ± 0.01	0.08 ± 0.01	0.040 ± 0.002	0.03 ± 0.01	0.036 ± 0.004
<b>In</b>	-	0.16 ± 0.02	0.0008 ± 0.0002	0.21 ± 0.01	0.19 ± 0.01	0.099 ± 0.004
<b>Total</b>	5.08 ± 0.05	4.8 ± 0.4	5.2 ± 0.1	5.0 ± 0.2	5.05 ± 0.04	4.77 ± 0.05
<b>K</b>	0.09 ± 0.002	0.29 ± 0.05	0.087 ± 0.003	0.187 ± 0.009	0.208 ± 0.005	0.178 ± 0.003
<b>Ca</b>	1.8 ± 0.02	1.5 ± 0.1	1.80 ± 0.02	1.92 ± 0.05	1.89 ± 0.02	1.91 ± 0.02
<b>Na</b>	0.30 ± 0.02	0.43 ± 0.04	0.29 ± 0.01	0.41 ± 0.02	0.45 ± 0.01	0.410 ± 0.007
<b>Total</b>	2.22 ± 0.03	2.3 ± 0.2	2.17 ± 0.02	2.52 ± 0.05	2.55 ± 0.02	2.50 ± 0.02
<b>Cl</b>	0.004 ± 0.001	0.07 ± 0.005	0.004 ± 0.001	0.061 ± 0.005	0.06 ± 0.01	0.105 ± 0.005
<b>OH</b>	1.86 ± 0.003	1.66 ± 0.02	1.849 ± 0.003	1.633 ± 0.008	1.67 ± 0.01	1.59 ± 0.01

Formulas calculated by the method of Hawthorne et al. (2012). Subpopulations are noted by [ ] and labeled in plots by value in [ ], see text for details.

<sup>†</sup>Runs that exhibited weight loss after removal from furnace, but showed no immediate signs of failure

Table 15 continued

	Amphibole Run 9	Amphibole Run 10 <sup>†</sup>	Amphibole Run 11 [11.1]	Amphibole Run 11 [11.2]	Amphibole Run 11 [11.3]	Amphibole Run 11 [11.4]
<b>Si</b>	6.59 ± 0.03	6.87 ± 0.03	7.3 ± 0.1	7.1 ± 0.06	6.96 ± 0.03	6.53 ± 0.03
<b>Al</b>	1.41 ± 0.02	1.13 ± 0.03	0.7 ± 0.1	0.9 ± 0.05	0.936 ± 0.003	1.442 ± 0.002
<b>Total</b>	8.00 ± 0.04	8.00 ± 0.04	8.0 ± 0.2	8.0 ± 0.08	7.9 ± 0.03	7.97 ± 0.03
<b>Al</b>	0.20 ± 0.01	0.38 ± 0.03	0.11 ± 0.02	0.11 ± 0.05	-	-
<b>Ti</b>	0.159 ± 0.003	0.199 ± 0.004	0.06 ± 0.02	0.08 ± 0.01	0.08 ± 0.004	0.163 ± 0.004
<b>Fe<sup>3+</sup></b>	< 0.41	0.067 ± 0.002	0.20 ± 0.12	0.20 ± 0.08	0.51 ± 0.04	0.41 ± 0.03
<b>Fe<sup>2+</sup></b>	1.20 ± 0.04	1.53 ± 0.01	1.5 ± 0.1	1.57 ± 0.08	1.29 ± 0.03	1.21 ± 0.02
<b>Mg</b>	3.21 ± 0.03	2.70 ± 0.03	3.2 ± 0.1	3.03 ± 0.09	3.07 ± 0.01	3.06 ± 0.01
<b>Mn</b>	0.031 ± 0.003	0.036 ± 0.002	0.08 ± 0.01	0.07 ± 0.01	0.08 ± 0.01	0.04 ± 0.01
<b>In</b>	0.224 ± 0.003	0.09 ± 0.01	0.002 ± 0.001	0.04 ± 0.01	0.112 ± 0.001	0.223 ± 0.001
<b>Total</b>	5.01 ± 0.05	5.00 ± 0.04	5.1 ± 0.2	5.1 ± 0.2	5.15 ± 0.05	5.10 ± 0.04
<b>K</b>	0.191 ± 0.003	0.158 ± 0.003	0.08 ± 0.01	0.09 ± 0.01	0.103 ± 0.004	0.153 ± 0.004
<b>Ca</b>	1.94 ± 0.01	1.80 ± 0.01	1.91 ± 0.01	1.90 ± 0.04	1.958 ± 0.002	1.924 ± 0.002
<b>Na</b>	0.44 ± 0.01	0.431 ± 0.004	0.23 ± 0.02	0.27 ± 0.02	0.26 ± 0.01	0.38 ± 0.01
<b>Total</b>	2.57 ± 0.01	2.39 ± 0.02	2.22 ± 0.02	2.27 ± 0.05	2.32 ± 0.01	2.46 ± 0.01
<b>Cl</b>	0.045 ± 0.002	0.067 ± 0.002	0.02 ± 0.01	0.03 ± 0.01	0.017 ± 0.002	0.056 ± 0.002
<b>OH</b>	1.64 ± 0.01	1.53 ± 0.01	1.85 ± 0.03	1.80 ± 0.03	1.80 ± 0.01	1.60 ± 0.01

Table 15 continued

	Amphibole Run 13			Amphibole Run 14 [14.1] <sup>T</sup>			Amphibole Run 14 [14.2] <sup>T</sup>		
<b>Si</b>	6.62	±	0.04	6.76	±	0.03	7.16	±	0.03
<b>Al</b>	1.38	±	0.03	1.24	±	0.03	0.84	±	0.03
<b>Total</b>	8.00	±	0.05	8.00	±	0.04	8.00	±	0.04
<b>Al</b>	0.22	±	0.04	0.15	±	0.02	0.16	±	0.03
<b>Ti</b>	0.19	±	0.01	0.16	±	0.01	0.079	±	0.004
<b>Fe<sup>3+</sup></b>	0.07	±	0.03	0.21	±	0.04	0.18	±	0.04
<b>Fe<sup>2+</sup></b>	1.42	±	0.04	1.46	±	0.04	1.58	±	0.03
<b>Mg</b>	2.83	±	0.06	3.05	±	0.04	3.02	±	0.01
<b>Mn</b>	0.039	±	0.003	0.038	±	0.002	0.07	±	0.01
<b>In</b>	0.29	±	0.01	0.131	±	0.004	0.0074	±	0.0003
<b>Total</b>	5.1	±	0.1	5.20	±	0.07	5.1	±	0.1
<b>K</b>	0.189	±	0.005	0.097	±	0.002	0.073	±	0.003
<b>Ca</b>	1.85	±	0.01	1.8	±	0.02	1.898	±	0.002
<b>Na</b>	0.43	±	0.01	0.33	±	0.02	0.258	±	0.008
<b>Total</b>	2.47	±	0.02	2.23	±	0.03	2.23	±	0.01
<b>Cl</b>	0.07	±	0.002	0.047	±	0.003	0.012	±	0.002
<b>OH</b>	1.55	±	0.01	1.62	±	0.01	1.82	±	0.01

Table 16

Run conditions and partition coefficients for amphibole runs

<b>Run</b>	<b>Temperature (°C)</b>	<b>Run Duration (Hours)</b>	<b>Partition Coefficient (Amphibole/Melt)</b>		
<b>Amphibole Run 4</b>	800	336	30	±	5
<b>Amphibole Run 6 [6.1]</b>	800	336	0.13	±	0.04
<b>Amphibole Run 6 [6.2]</b>	800	336	35	±	3
<b>Amphibole Run 7</b>	800	672	26	±	1
<b>Amphibole Run 8<sup>T</sup></b>	800	1008	28	±	2
<b>Amphibole Run 9</b>	800	504	40	±	2
<b>Amphibole Run 10<sup>T</sup></b>	800	1344	41	±	3
<b>Amphibole Run 11 [11.1]</b>	800	520	0.4	±	0.1
<b>Amphibole Run 11 [11.2]</b>	800	520	7	±	1
<b>Amphibole Run 11 [11.3]</b>	800	520	16.5	±	0.4
<b>Amphibole Run 11 [11.4]</b>	800	520	33.6	±	0.8
<b>Amphibole Run 13</b>	800	1776	50	±	2
<b>Amphibole Run 14 [14.1]<sup>T</sup></b>	800	1344	96	±	7
<b>Amphibole Run 14 [14.2]<sup>T</sup></b>	800	1344	5.5	±	0.5

<sup>T</sup>Runs that exhibited weight loss after removal from furnace, but showed no immediate signs of failure

Pressure of all runs is 100 MPa.

Subpopulations are noted by [ ] and labeled in plots by value in [ ], see text for details.

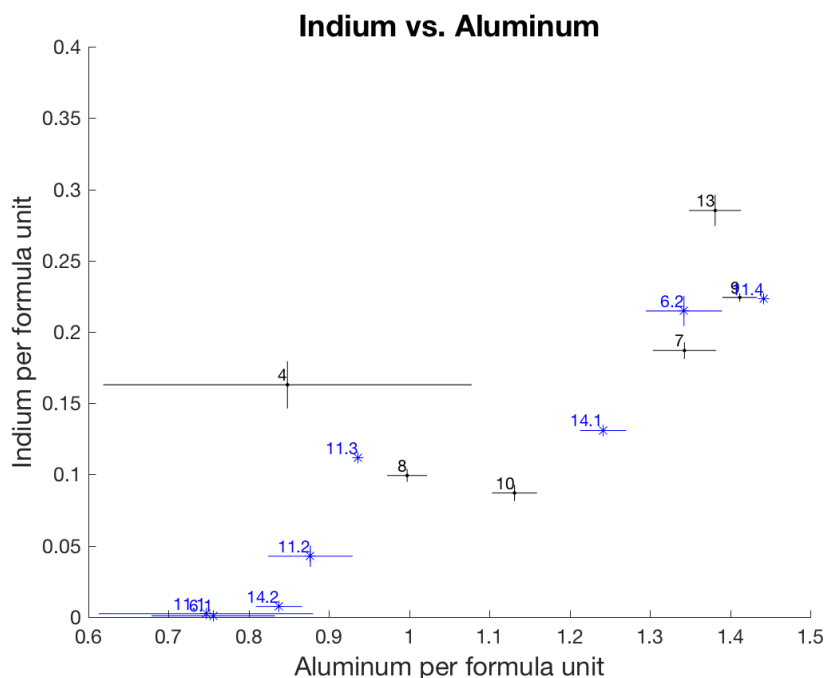


Figure 12: Indium per formula unit vs. aluminum per formula unit of experimentally grown amphibole. Amphibole formulas calculated according to the method of Hawthorne et al. (2012). Error bars are standard deviations from the mean or uncertainty due to counting statistics ( $1\sigma_m$ ). Numbers corresponds to run number in Table 14. Data points plotted in blue represent subpopulations.

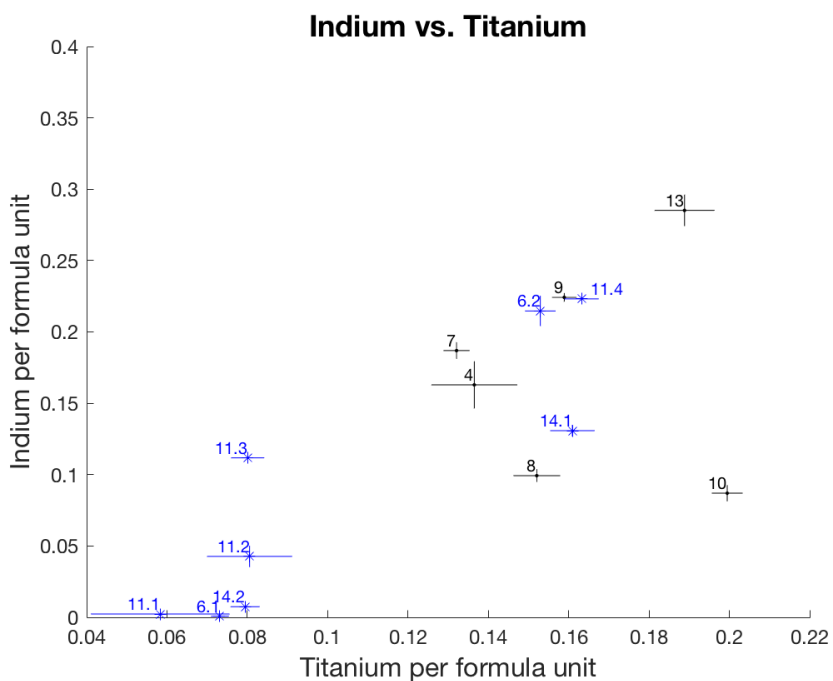


Figure 13: Indium per formula unit vs. titanium per formula unit of experimentally grown amphibole. See Figure 12 for additional details.

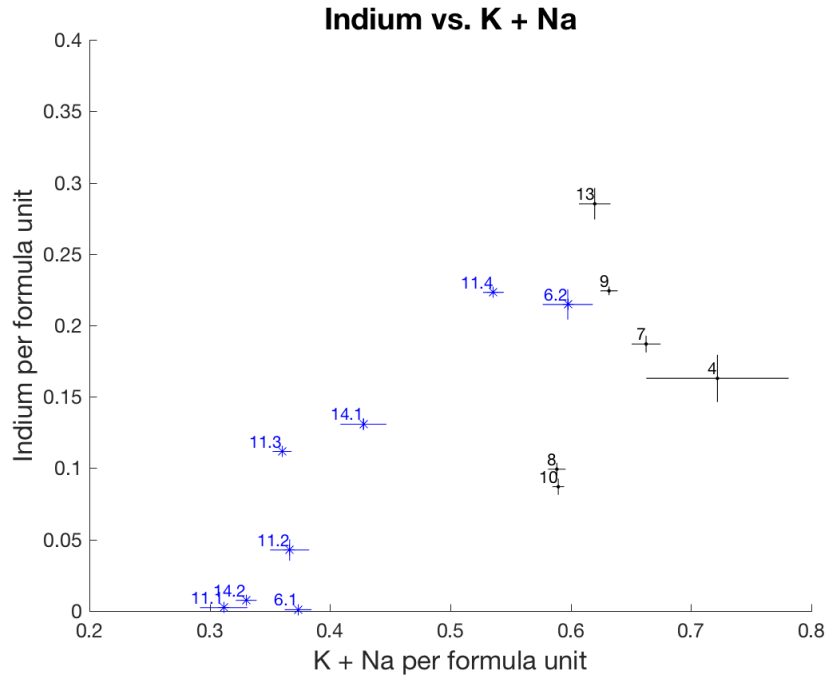


Figure 14: Indium per formula unit vs. K + Na per formula unit for experimentally grown amphibole. See Figure 12 for additional details.

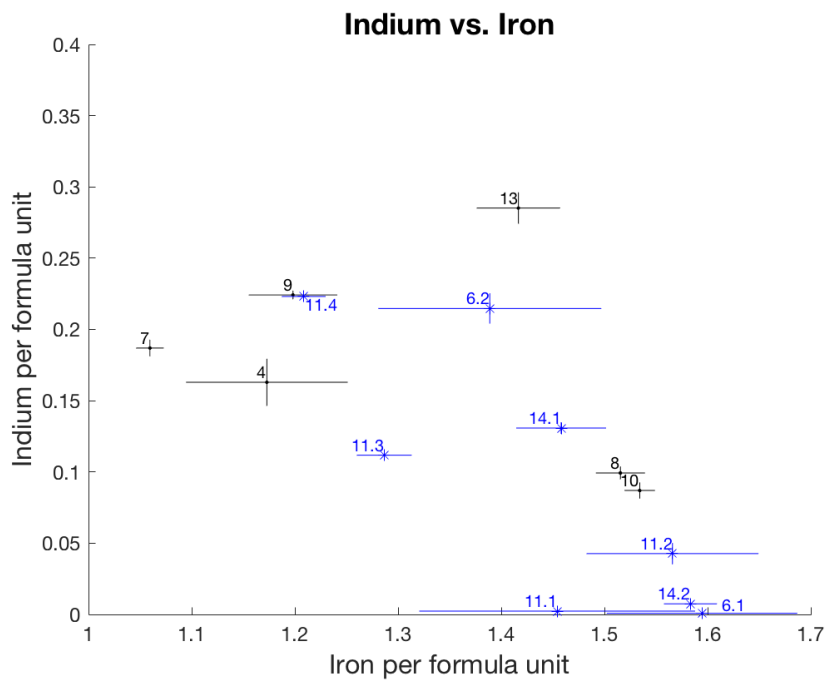


Figure 15: Indium per formula unit vs. Iron per formula unit for experimentally grown amphibole. See Figure 12 for additional details.

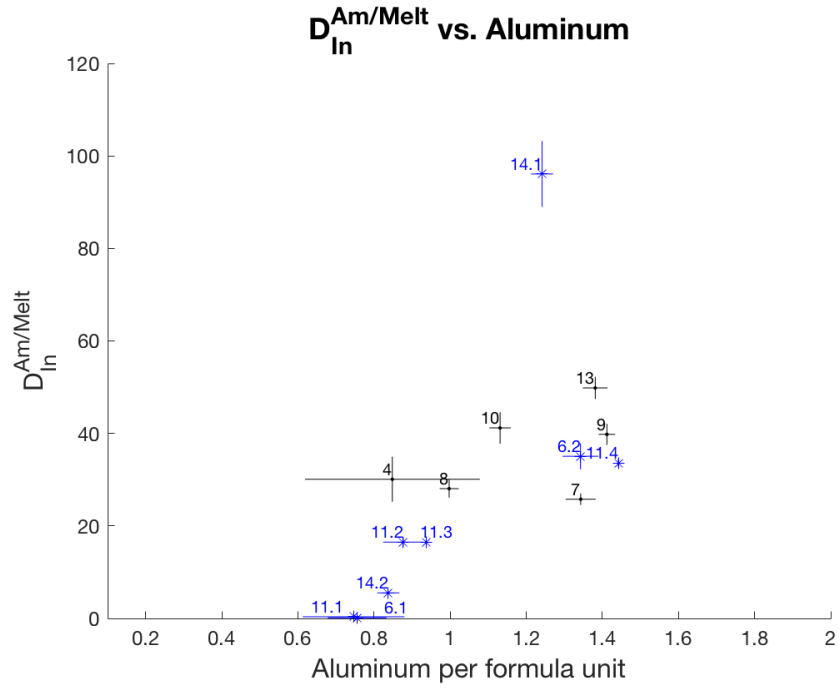


Figure 16: Partition coefficients for indium between amphibole/melt vs. aluminum per formula unit for experimentally grown amphibole. See Figure 12 for additional details.

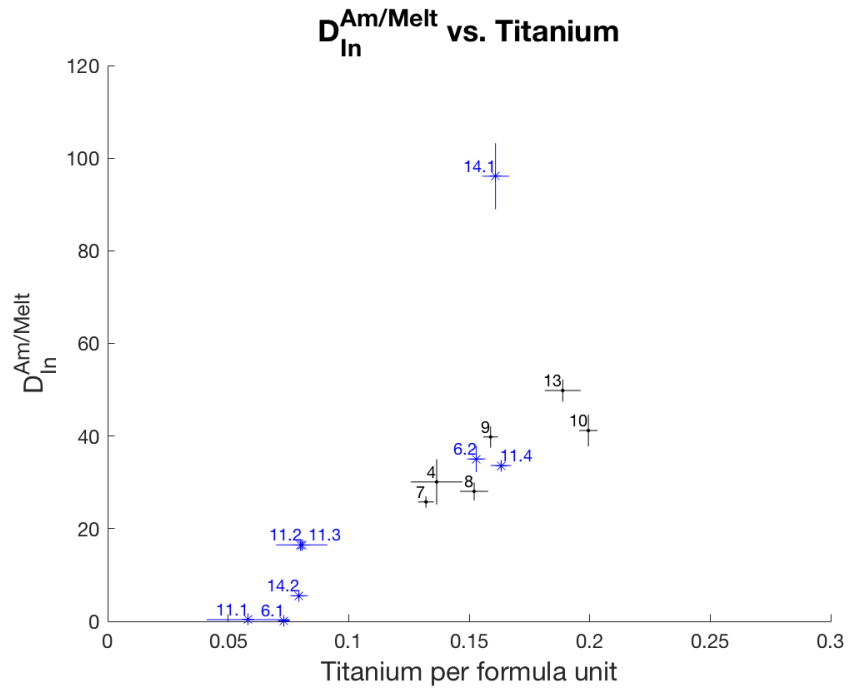


Figure 17: Partition coefficients for indium between amphibole/melt vs. titanium per formula unit for experimentally grown amphibole. Blue lines are 95% confidence intervals. See Figure 12 for additional details

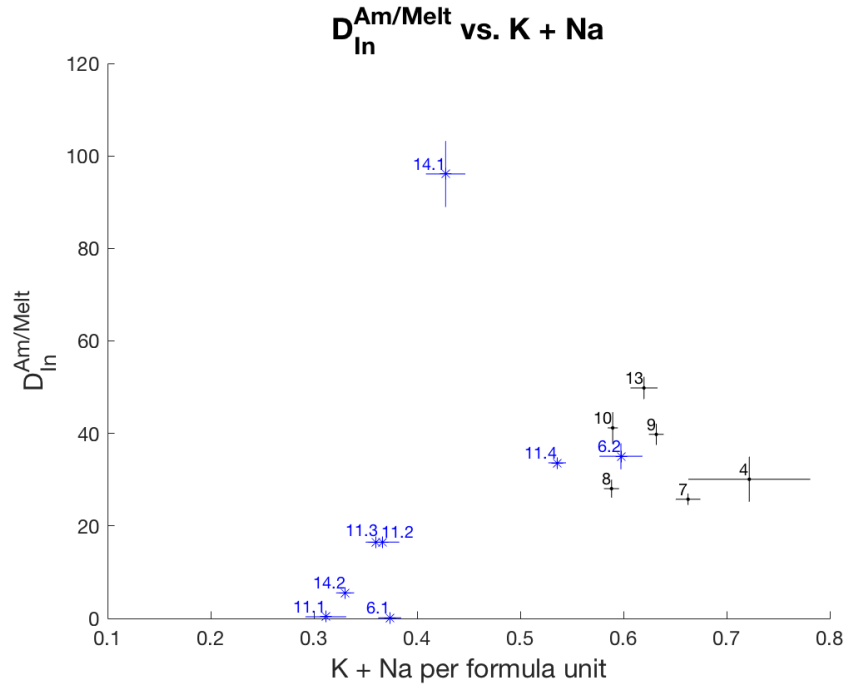


Figure 18: Partition coefficients for indium between amphibole/melt vs. K+ Na per formula unit for experimentally grown amphibole. Blue lines are 95% confidence intervals. See Figure 12 for additional details.

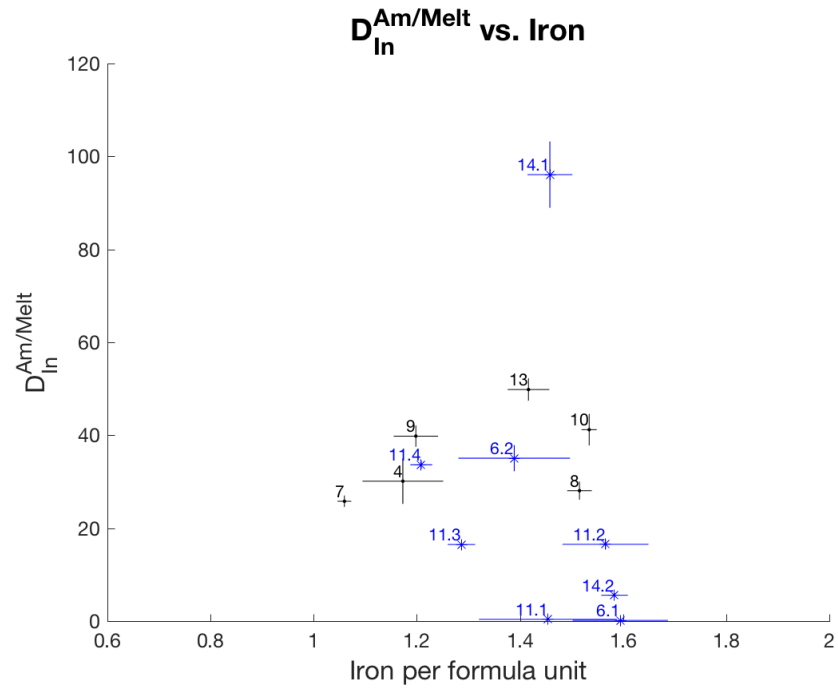


Figure 19: Partition coefficients for indium between amphibole/melt vs. iron per formula unit for experimentally grown amphibole. See Figure 12 for additional details.

### 4.3. Vapor/Melt Experiments

In five experiments (two biotite/melt and three amphibole/melt) run product fluid was extracted and analyzed by ICP-MS. The mean  $D_{In}^{Vapor/Melt}$  is  $17 \pm 5$  (Table 17), with a range of

Table 17  
Indium concentration in run product fluids and vapor/melt partition coefficient

Run	Indium Concentration (ppm)	Partition coefficient (Vapor/Melt)		
Biotite Run 31	7,660	31	±	5
Biotite Run 32	3,700	24	±	2
Amphibole Run 9	13,750	19	±	1
Amphibole Run 11	2,200	2.68	±	0.07
Amphibole Run 13	5,780	8.2	±	0.3

Indium concentration determined by ICP-MS. Relative standard deviation for the total number of counts in ICP-MS analyses is between 0.1% to 0.2%.

2.7 to 31. Because the fluid is not trapped within a fluid inclusion, indium, as well as other components of the fluid could precipitate during quench. In the case of this study, the measured  $D_{In}^{Vapor/Melt}$  represent an order of magnitude estimation and will be used as such.  $D_{In}^{Vapor/Melt}$  is strongly affected by the Cl concentration of vapor and

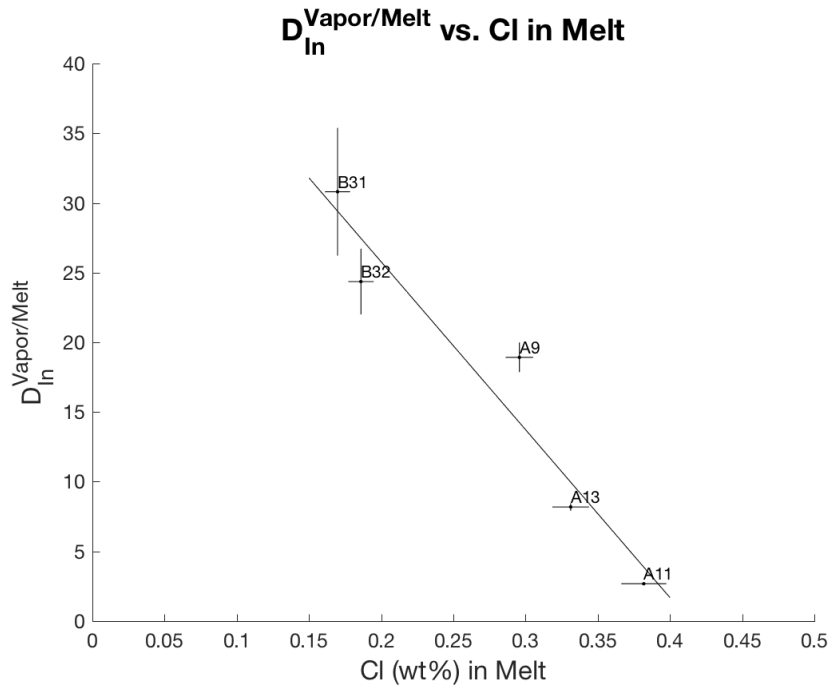


Figure 20: Vapor/melt partition coefficient vs. chlorine concentration in the melt. B indicates biotite run, A indicates amphibole run.

the melt, such that the greater the concentration of Cl in melt the lower the partition coefficient (Figure 20). However, this result is highly preliminary and should be viewed with caution.

#### 4.4. *Indium Silicates*

In total, nine experiments resulted in the nucleation and growth of a crystalline indium silicate ( $\text{In}_2\text{Si}_2\text{O}_7$ ). This phase was originally described by Ito (1968) and has been termed In-thortveitite, due to its isostructural nature with the scandium mineral thortveitite ( $\text{Sc}_2\text{Si}_2\text{O}_7$ ). The chemical composition of the In-thortveitite crystals synthesized in this study are liken to that described by Ito (1968). However, the crystals grown here contain up to 3 wt% FeO and minor amounts of  $\text{Al}_2\text{O}_3$ . The compositions of select indium silicates are listed in Table 18. These compositional variations are likely due to the presence of magnetite, contributing to high iron, and the high ASI of the melt, contributing to high  $\text{Al}_2\text{O}_3$ . These run product crystals are also presumed to be isostructural with thortveitite, as reported by Ito (1968).

Table 18  
Composition of indium silicates in experimental runs

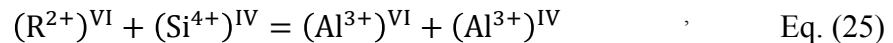
	Biotite Run 20 (N=5)			Biotite Run 23 (N=4)			Biotite Run 24 (N=4)			Biotite Run 27 (N=3)			Amphibole Run 4 (N=5)			Amphibole Run 6 (N=5)		
$\text{In}_2\text{O}_3$	64.3	±	0.3	63.8	±	0.4	64.5	±	0.4	64.2	±	0.4	62.3	±	0.3	63	±	0.5
FeO	2.6	±	0.2	2.6	±	0.2	2.4	±	0.1	2.9	±	0.1	2.4	±	0.2	2.2	±	0.2
$\text{SiO}_2$	32.8	±	0.1	32.7	±	0.2	32.7	±	0.2	33.00	±	0.05	32.6	±	0.4	32.4	±	0.2
$\text{Al}_2\text{O}_3$	0.07	±	0.02	0.13	±	0.03	0.7	±	0.4	0.5		0.2	n.a.		n.a.			
<b>Total</b>	<b>99.8</b>	<b>±</b>	<b>0.4</b>	<b>99.2</b>	<b>±</b>	<b>0.5</b>	<b>100</b>	<b>±</b>	<b>1</b>	<b>100.6</b>	<b>±</b>	<b>0.4</b>	<b>97</b>	<b>±</b>	<b>1</b>	<b>97</b>	<b>±</b>	<b>1</b>

Values (in wt%) determined by Electron Microprobe Analysis (EPMA)  
n.a. is not analyzed

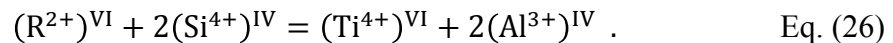
## Chapter 5: Discussion

### 5.1. Substitution of Indium into Biotite and Amphibole

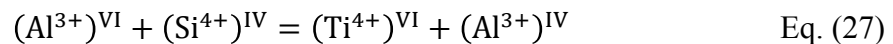
Compositional variations in biotite and amphibole indicate that multiple exchanges and substitutions are occurring. Generally there is a primary Al-Tschermak exchange occurring following equation 25:



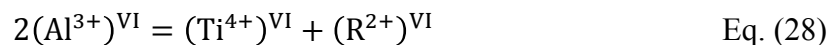
where  $(R^{2+})^{VI}$  is a 2+ metal cation in the octahedral site. The substitution of Ti into biotite and amphibole can occur through a variety of substitutions. Dymek (1983) summarizes several substitutions for Ti into biotite (Equations 26-29), which can be used analogously for Ti substitutions into amphibole. For a Ti-Tschermak component:



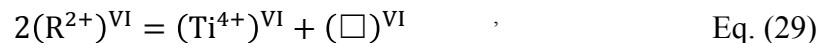
Another coupled substitution would be:



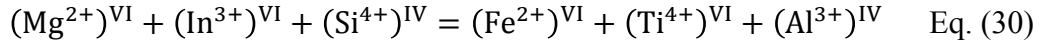
or a direct substitute of Ti into the octahedral site:



or:

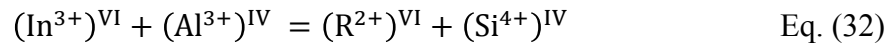
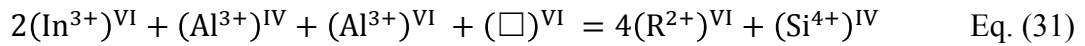


where  $\square$  is a vacancy. Applying these exchanges to experimental biotite, a possible exchange component involving the substitution of indium, where indium is assumed to be  $In^{3+}$ , into biotite can be estimated. For biotite the substitution is given in equation 30.

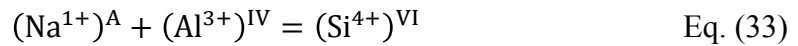


Given the low concentrations of both indium and titanium in the experimental biotite, this exchange is difficult to detect. Equation 30 is thus inferred from the previously listed exchange components and variations in the partition coefficient as a function of biotite composition.

For amphibole, the exchanges and substitutions are more easily detected due to the higher concentrations of indium and titanium. Indium, again assumed to be  $\text{In}^{3+}$ , can be substituted into amphibole by equation 31 or 32.



Reversing the substitutions with the goal of producing an amphibole with a tremolite formula ( $\text{Ca}_2\text{Mg}_5\text{Si}_8\text{O}_{22}(\text{OH})_2$ ), up to 2/3 of the indium substituting into amphibole follows equation 31, while the remaining 1/3 follows equation 32. As for titanium, 1/3 substitutions follow equations 26, 27, and 28, respectively. These indium and titanium substitution are overprinted by the Al-Tschermak exchange (equation 25) and Na- exchange given in equation 33.



It should be noted that equation 32 is essentially an Al-Tschermak exchange coupled with an exchange of  $(\text{In}^{3+})^{\text{VI}}$  for  $(\text{Al}^{3+})^{\text{VI}}$ .

5.2. Effect of Oxygen Fugacity on Biotite

Composition

As discussed above, oxygen fugacity is a major influence on mineral stability.

The vessels used here have an intrinsic  $f_{O_2}$  of NNO + 1.3 and thus this is the  $f_{O_2}$  imposed on the system and is not expected to vary significantly between experiments.

An  $f_{O_2}$  for each experiment was calculated by using the fugacity equation given by Czamanske and Wones (1973) (see equation 5) (Table 19). The  $f_{O_2}$  calculated by

equation 5 vary significantly from the imposed oxygen fugacity, which are interrupted to be an artifact of the

experimental design (i.e. slight changes in proportions of starting materials) and termed “fictive oxygen fugacities”. Plotting

$D_{In}^{Bt/Melt}$  vs. fictive oxygen fugacities results

in a relationship that show  $D_{In}^{Bt/Melt}$  increasing with increasing oxidation (Figure

21). Although these are fictive oxygen fugacities, in natural systems  $f_{O_2}$  does influence biotite composition (Wones and Eugster, 1965), which in turn would affect

Table 19

Run	Fictive Oxygen Fugacity ( $\Delta$ NNO)
<b>Biotite Run 1<sup>§</sup></b>	n.d.
<b>Biotite Run 4</b>	1.0
<b>Biotite Run 8</b>	-0.1
<b>Biotite Run 11</b>	0.5
<b>Biotite Run 12<sup>†</sup></b>	2.0
<b>Biotite Run 13*</b>	0.6
<b>Biotite Run 15 [15.1]</b>	1.6
<b>Biotite Run 15 [15.2]</b>	2.1
<b>Biotite Run 20</b>	3.1
<b>Biotite Run 21*</b>	0.4
<b>Biotite Run 23 [23.1]</b>	0.4
<b>Biotite Run 23 [23.2]</b>	1.3
<b>Biotite Run 23 [23.3]</b>	0.2
<b>Biotite Run 24</b>	1.2
<b>Biotite Run 26</b>	2.1
<b>Biotite Run 27</b>	3.1
<b>Biotite Run 28</b>	2.9
<b>Biotite Run 29<sup>§</sup></b>	0.1
<b>Biotite Run 31</b>	0.7
<b>Biotite Run 32</b>	1.2

Fictive oxygen fugacities calculated from Czamanske and Wones (1973)

$D_{\text{In}}^{\text{Bt/Melt}}$ . Thus, Figure 21 represents a predicted relationship between  $D_{\text{In}}^{\text{Bt/Melt}}$  and  $f_{\text{O}_2}$  in natural system.

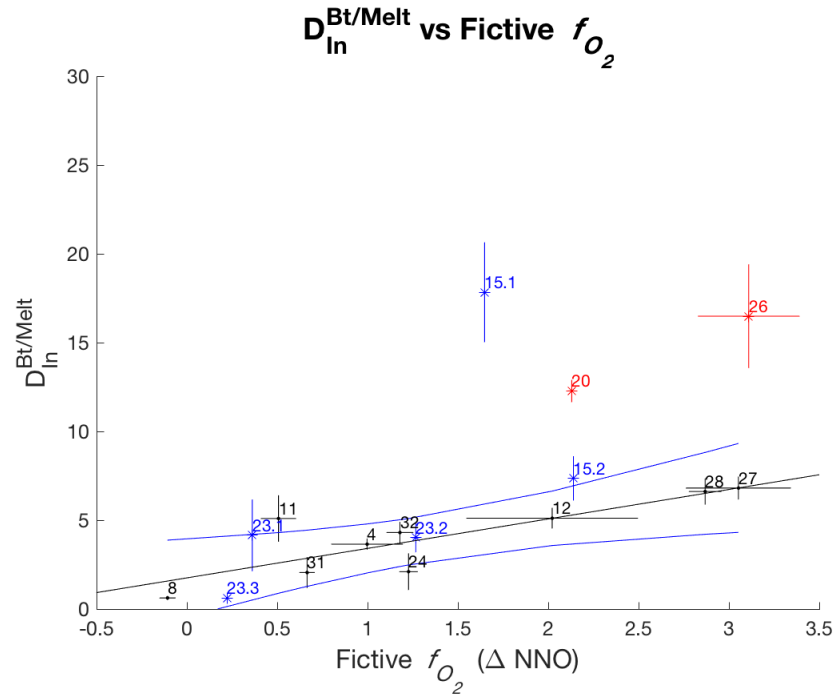


Figure 21: Partition coefficients for indium between biotite/melt vs. fictive  $f_{\text{O}_2}$  relative to NNO of experiments. Blue lines represent the 95% confidence interval. See Figure 6 for additional details.

### 5.3. Thermodynamics of Indium Partitioning between Biotite and Melt

$D_{\text{In}}^{\text{Bt/Melt}}$  can be evaluated thermodynamically. To do so, thermodynamic equilibria have been derived from a Gauss-Jordan reduction following the method of Thompson (1982) (Appendix F). There are 17 phase components of interest:  $\text{KMg}_3\text{AlSi}_3\text{O}_{10}(\text{OH})_2$ ,  $\text{KFe}_3\text{AlSi}_3\text{O}_{10}(\text{OH})_2$ , and  $\text{KIn}_2\text{AlSi}_3\text{O}_{10}(\text{OH})_2$  are components of the biotite solid solution;  $\text{KAlSi}_3\text{O}_8$  and  $\text{NaAlSi}_3\text{O}_8$  are components of the alkali feldspar solid solution;  $\text{MgSiO}_3$  and  $\text{FeSiO}_3$  are components of orthopyroxene solid solution; and  $\text{Fe}_3\text{O}_4$  is the lone component of spinel. The aqueous volatile phase has the phase components:  $\text{H}_2\text{O}$ ,  $\text{HCl}$ ,  $\text{NaCl}$ ,  $\text{KCl}$ , and  $\text{InCl}_3$ . The melt phase has two

phase components that take part in the equilibria considered herein:  $\text{SiO}_2$  and  $\text{In}_2\text{O}_3$ .

There are two additional phase components: metallic indium in the InAu alloy and  $\text{O}_2$  that will be represented in the equilibria as a component of the system. These phase components can be defined by 10 system components written as elements: K, Na, Al, Mg, Si, Fe, H, Cl, In, and O. Given these phase and system components, 7 linearly independent equilibria (equations 34 to 40) are derived:

$$\mu_{\text{NaAlSi}_3\text{O}_8}^{\text{Fsp}} + \mu_{\text{KCl}}^{\text{Vapor}} = \mu_{\text{KAlSi}_3\text{O}_8}^{\text{Fsp}} + \mu_{\text{NaCl}}^{\text{Vapor}} \quad \text{Eq. (34)}$$

$$\mu_{\text{KMg}_3\text{AlSi}_3\text{O}_{10}(\text{OH})_2}^{\text{Bt}} + 3\mu_{\text{FeSiO}_3}^{\text{Opx}} = 3\mu_{\text{MgSiO}_3}^{\text{Opx}} + \mu_{\text{KFe}_3\text{AlSi}_3\text{O}_{10}(\text{OH})_2}^{\text{Bt}} \quad \text{Eq. (35)}$$

$$\mu_{\text{KMg}_3\text{AlSi}_3\text{O}_{10}(\text{OH})_2}^{\text{Bt}} + 3\mu_{\text{SiO}_2}^{\text{Melt}} = \mu_{\text{KAlSi}_3\text{O}_8}^{\text{Fsp}} + 3\mu_{\text{MgSiO}_3}^{\text{Opx}} + \mu_{\text{H}_2\text{O}}^{\text{Vapor}} \quad \text{Eq. (36)}$$

$$\mu_{\text{KFe}_3\text{AlSi}_3\text{O}_{10}(\text{OH})_2}^{\text{Bt}} + \frac{1}{2}\mu_{\text{O}_2}^{\text{System}} = \mu_{\text{KAlSi}_3\text{O}_8}^{\text{Fsp}} + \mu_{\text{Fe}_3\text{O}_4}^{\text{Mt}} + \mu_{\text{H}_2\text{O}}^{\text{Vapor}} \quad \text{Eq. (37)}$$

$$\mu_{\text{KAlSi}_3\text{O}_8}^{\text{Fsp}} + \mu_{\text{H}_2\text{O}}^{\text{Vapor}} + \mu_{\text{In}_2\text{O}_3}^{\text{Melt}} = \mu_{\text{KIn}_2\text{AlSi}_3\text{O}_{10}(\text{OH})_2}^{\text{Bt}} \quad \text{Eq. (38)}$$

$$\mu_{\text{KAlSi}_3\text{O}_8}^{\text{Fsp}} + 4\mu_{\text{H}_2\text{O}}^{\text{Vapor}} + 2\mu_{\text{InCl}_3}^{\text{Vapor}} = \mu_{\text{KIn}_2\text{AlSi}_3\text{O}_{10}(\text{OH})_2}^{\text{Bt}} + 6\mu_{\text{HCl}}^{\text{Vapor}} \quad \text{Eq. (39)}$$

$$\mu_{\text{KAlSi}_3\text{O}_8}^{\text{Fsp}} + 2\mu_{\text{In}}^{\text{Alloy}} + \mu_{\text{H}_2\text{O}}^{\text{Vapor}} + \frac{3}{2}\mu_{\text{O}_2}^{\text{System}} = \mu_{\text{KIn}_2\text{AlSi}_3\text{O}_{10}(\text{OH})_2}^{\text{Bt}} \quad \text{Eq. (40)}$$

The partitioning of indium between biotite and melt can be expressed as an equilibrium written in terms of chemical potentials as shown by equation 38.

The formal equilibrium constant for equation 38 can be expressed as:

$$K_1 = \frac{a_{\text{KIn}_2\text{AlSi}_3\text{O}_{10}(\text{OH})_2}^{\text{Bt}}}{a_{\text{In}_2\text{O}_3}^{\text{Melt}} \cdot a_{\text{KAlSi}_3\text{O}_8}^{\text{Fsp}} \cdot f_{\text{H}_2\text{O}}^{\text{Melt}}}, \quad \text{Eq. (41)}$$

where  $a_{\text{KIn}_2\text{AlSi}_3\text{O}_{10}(\text{OH})_2}^{\text{Bt}}$  is written as  $a_{\text{InBt}}^{\text{Bt}}$  for convenience. The equilibrium constant can be rearranged to yield

$$\left( \frac{x_{\text{InBt}}^{\text{Bt}}}{x_{\text{In}_2\text{O}_3}^{\text{Melt}}} \right) = K_1 \left( \frac{\gamma_{\text{In}_2\text{O}_3}^{\text{Melt}}}{\gamma_{\text{InBt}}^{\text{Bt}}} \right) \cdot a_{\text{KAlSi}_3\text{O}_8}^{\text{Fsp}} \cdot f_{\text{H}_2\text{O}}^{\text{Melt}} \quad \text{Eq. (42)}$$

The partition coefficient can be expressed as:

$$\left(\frac{X_{\text{In}}^{\text{Bt}}}{X_{\text{In}}^{\text{Melt}}}\right)\beta = D_{\text{In}}^{\text{Bt/Melt}} \quad , \quad \text{Eq. (43)}$$

where  $X_{\text{InBt}}^{\text{Bt}} = X_{\text{In}}^{\text{Bt}}$ ,  $X_{\text{In}_2\text{O}_3}^{\text{Melt}} = X_{\text{In}}^{\text{Melt}}$ , and  $\beta$  is the constant of proportionality converting mole fraction to concentration in ppm. The equilibrium is then expressed as:

$$D_{\text{In}}^{\text{Bt/Melt}} = K_1' \cdot a_{\text{KAlSi}_3\text{O}_8}^{\text{Fsp}} \cdot f_{\text{H}_2\text{O}}^{\text{Melt}} \quad , \quad \text{Eq. (44)}$$

where:

$$K_1 \left(\frac{\gamma_{\text{In}_2\text{O}_3}^{\text{Melt}}}{\gamma_{\text{InBt}}^{\text{Bt}}}\right)\beta = K_1' \quad . \quad \text{Eq. (45)}$$

The logarithmic transformation of the partition coefficient is:

$$\log D_{\text{In}}^{\text{Bt/Melt}} = \log K_1' + \log a_{\text{KAlSi}_3\text{O}_8}^{\text{Fsp}} + \log f_{\text{H}_2\text{O}}^{\text{Melt}} \quad . \quad \text{Eq. (46)}$$

Equation 46 describes the variation in the partition coefficient as a function of  $f_{\text{H}_2\text{O}}^{\text{Melt}}$  and  $a_{\text{KAlSi}_3\text{O}_8}^{\text{Fsp}}$ .

#### 5.4. Thermodynamics of Indium Partitioning between Amphibole and Melt

In the same method used to evaluate  $D_{\text{In}}^{\text{Bt/Melt}}$ ,  $D_{\text{In}}^{\text{Am/Melt}}$  is evaluated thermodynamically using the method of Thompson (1982) (Appendix F). There are 18 phase components of interest:  $\text{Ca}_2\text{Mg}_5\text{Si}_8\text{O}_{22}(\text{OH})_2$ ,  $\text{Ca}_2\text{Fe}_5\text{Si}_8\text{O}_{22}(\text{OH})_2$ ,  $\text{Ca}_2\text{Mg}_4\text{AlSi}_7\text{AlO}_{22}(\text{OH})_2$ ,  $\text{Ca}_2\text{Mg}_4\text{InSi}_7\text{AlO}_{22}(\text{OH})_2$ ,  $\text{Ca}_2\text{In}_2\text{Al}_2\text{Si}_6\text{Al}_2\text{O}_{22}(\text{OH})_2$ ,  $\text{NaCa}_2\text{Mg}_5\text{Si}_7\text{AlO}_{22}(\text{OH})_2$  are phase components of the amphibole solid solution;  $\text{SiO}_2$ ,  $\text{Al}_2\text{O}_3$ ,  $\text{MgO}$ ,  $\text{FeO}$ ,  $\text{CaO}$ ,  $\text{Na}_2\text{O}$ , and  $\text{In}_2\text{O}_3$  are phase components of the melt;  $\text{H}_2\text{O}$ ,  $\text{HCl}$ , and  $\text{InCl}_3$  are phase components of the vapor. Two additional phase components: metallic indium, in the InAu alloy, and  $\text{O}_2$  that will be represented in the equilibria as a component of the system. For simplicity, the Mg bearing amphibole

phases will be the main phase components considered. These phase components can be defined by 10 system components written as elements: Ca, Na, Al, Mg, Si, Fe, H, Cl, In, and O. These phase and system components define 8 linearly independent equilibria (equations 47 to 54).

$$\mu_{\text{Ca}_2\text{Mg}_5\text{Si}_8\text{O}_{22}(\text{OH})_2}^{\text{Am}} + 5\mu_{\text{FeO}}^{\text{Melt}} = \mu_{\text{Ca}_2\text{Fe}_5\text{Si}_8\text{O}_{22}(\text{OH})_2}^{\text{Am}} + 5\mu_{\text{MgO}}^{\text{Melt}} \quad \text{Eq. (47)}$$

$$\mu_{\text{Ca}_2\text{Mg}_5\text{Si}_8\text{O}_{22}(\text{OH})_2}^{\text{Am}} + \mu_{\text{Al}_2\text{O}_3}^{\text{Melt}} = \mu_{\text{Ca}_2\text{Mg}_4\text{AlSi}_7\text{AlO}_{22}(\text{OH})_2}^{\text{Am}} + \mu_{\text{MgO}}^{\text{Melt}} + \mu_{\text{SiO}_2}^{\text{Melt}} \quad \text{Eq. (48)}$$

$$\mu_{\text{Ca}_2\text{Mg}_5\text{Si}_8\text{O}_{22}(\text{OH})_2}^{\text{Am}} + \frac{1}{2}\mu_{\text{Al}_2\text{O}_3}^{\text{Melt}} + \frac{1}{2}\mu_{\text{Na}_2\text{O}}^{\text{Melt}} = \mu_{\text{NaCa}_2\text{Mg}_5\text{Si}_7\text{AlO}_{22}(\text{OH})_2}^{\text{Am}} + \mu_{\text{SiO}_2}^{\text{Melt}} \quad \text{Eq. (49)}$$

$$\mu_{\text{Ca}_2\text{Mg}_4\text{AlSi}_7\text{AlO}_{22}(\text{OH})_2}^{\text{Am}} = 7\mu_{\text{SiO}_2}^{\text{Melt}} + 4\mu_{\text{MgO}}^{\text{Melt}} + 2\mu_{\text{CaO}}^{\text{Melt}} + \mu_{\text{Al}_2\text{O}_3}^{\text{Melt}} + \mu_{\text{H}_2\text{O}}^{\text{Vapor}} \quad \text{Eq. (50)}$$

$$\mu_{\text{Ca}_2\text{Mg}_4\text{AlSi}_7\text{AlO}_{22}(\text{OH})_2}^{\text{Am}} + \mu_{\text{In}_2\text{O}_3}^{\text{Melt}} + \mu_{\text{Al}_2\text{O}_3}^{\text{Melt}} = \mu_{\text{Ca}_2\text{In}_2\text{Al}_2\text{Si}_6\text{Al}_2\text{O}_{22}(\text{OH})_2}^{\text{Am}} + 4\mu_{\text{MgO}}^{\text{Melt}} + \mu_{\text{SiO}_2}^{\text{Melt}} \quad \text{Eq. (51)}$$

$$\mu_{\text{Ca}_2\text{Mg}_5\text{Si}_8\text{O}_{22}(\text{OH})_2}^{\text{Am}} + \mu_{\text{In}_2\text{O}_3}^{\text{Melt}} + \mu_{\text{Al}_2\text{O}_3}^{\text{Melt}} = \mu_{\text{Ca}_2\text{Mg}_3\text{In}_2\text{Si}_6\text{Al}_2\text{O}_{22}(\text{OH})_2}^{\text{Am}} + 2\mu_{\text{MgO}}^{\text{Melt}} + 2\mu_{\text{SiO}_2}^{\text{Melt}} \quad \text{Eq. (52)}$$

$$\mu_{\text{In}_2\text{O}_3}^{\text{Melt}} + 6\mu_{\text{HCl}}^{\text{Vapor}} = 3\mu_{\text{H}_2\text{O}}^{\text{Vapor}} + 2\mu_{\text{InCl}_3}^{\text{Vapor}} \quad \text{Eq. (53)}$$

$$2\mu_{\text{In}}^{\text{Alloy}} + \frac{3}{2}\mu_{\text{O}_2}^{\text{System}} = \mu_{\text{In}_2\text{O}_3}^{\text{Melt}} \quad \text{Eq. (54)}$$

Other amphibole endmembers, not used here, can be derived using this set of equilibria, including various Na and Fe bearing amphibole phases.  $D_{\text{In}}^{\text{Am/Melt}}$  can be expressed using equations 51 and 52. The formal equilibrium constant for equation 51 can be expressed as:

$$K_2 = \frac{(a_{\text{MgO}}^{\text{Melt}})^4 \cdot a_{\text{SiO}_2}^{\text{Melt}} \cdot a_{\text{In-Al-Ts}}^{\text{Am}}}{a_{\text{In}_2\text{O}_3}^{\text{Melt}} \cdot a_{\text{Al}_2\text{O}_3}^{\text{Melt}} \cdot a_{\text{Mg-Hbl}}^{\text{Am}}}, \quad \text{Eq. (55)}$$

where  $a_{\text{Ca}_2\text{In}_2\text{Al}_2\text{Si}_6\text{Al}_2\text{O}_{22}(\text{OH})_2}^{\text{Am}}$  is written as  $a_{\text{In-Al-Ts}}^{\text{Am}}$  and  $\mu_{\text{Ca}_2\text{Mg}_4\text{AlSi}_7\text{AlO}_{22}(\text{OH})_2}^{\text{Am}}$  is written as  $a_{\text{Mg-Hbl}}^{\text{Am}}$  for convenience. Rearranging yields equation 56:

$$K_2 \left( \frac{\gamma_{\text{In}}^{\text{Melt}}}{\gamma_{\text{In-Al-Ts}}^{\text{Am}}} \right) \frac{a_{\text{Al}_2\text{O}_3}^{\text{Melt}} \cdot a_{\text{Mg-Hbl}}^{\text{Am}}}{(a_{\text{MgO}}^{\text{Melt}})^4 \cdot a_{\text{SiO}_2}^{\text{Melt}}} = \frac{X_{\text{In-Al-Ts}}^{\text{Am}}}{X_{\text{In}}^{\text{Melt}}} \quad , \quad \text{Eq. (56)}$$

where  $X_{\text{In}_2\text{O}_3}^{\text{Melt}} = X_{\text{In}}^{\text{Melt}}$ . At this point is useful to refer back to indium substitutions into amphibole. Approximately 2/3 of indium substituting into amphibole follow equation 31, which is represented by the equilibria 51. The  $D_{\text{In}}^{\text{Am/Melt}}$  can be represented by equation 57:

$$D_{\text{In}}^{\text{Am/Melt}} = \left( \frac{X_{\text{In}}^{\text{Am}}}{X_{\text{In}}^{\text{Melt}}} \right) \tau \quad , \quad \text{Eq. (57)}$$

when

$$0.66X_{\text{In}}^{\text{Am}} = X_{\text{In-Al-Ts}}^{\text{Am}} \quad \text{Eq. (58)}$$

and

$$K_2 \left( \frac{\gamma_{\text{In}}^{\text{Melt}}}{\gamma_{\text{In-Al-Ts}}^{\text{Am}}} \right) \tau \frac{a_{\text{Al}_2\text{O}_3}^{\text{Melt}} \cdot a_{\text{Mg-Hbl}}^{\text{Am}}}{(a_{\text{MgO}}^{\text{Melt}})^4 \cdot a_{\text{SiO}_2}^{\text{Melt}}} = \left( \frac{0.66X_{\text{In}}^{\text{Am}}}{X_{\text{In}}^{\text{Melt}}} \right) \tau \quad , \quad \text{Eq. (59)}$$

where  $\tau$  is the constant of proportionality converting mole fraction to concentration in ppm.

Thus,

$$\frac{K'_2}{0.66} \frac{a_{\text{Al}_2\text{O}_3}^{\text{Melt}} \cdot a_{\text{Mg-Hbl}}^{\text{Am}}}{(a_{\text{MgO}}^{\text{Melt}})^4 \cdot a_{\text{SiO}_2}^{\text{Melt}}} = D_{\text{In}}^{\text{Am/Melt}} \quad , \quad \text{Eq. (60)}$$

where

$$K'_2 = K_2 \left( \frac{\gamma_{\text{In}}^{\text{Melt}}}{\gamma_{\text{In-Al-Ts}}^{\text{Am}}} \right) \tau. \quad \text{Eq. (61)}$$

The logarithmic transformation of equation 60 is thus

$$\begin{aligned} \log(D_{\text{In}}^{\text{Am/Melt}}) &= \log(K'_2) + \log(a_{\text{Al}_2\text{O}_3}^{\text{Melt}}) + \log(a_{\text{Mg-Hbl}}^{\text{Am}}) - 4 \log(a_{\text{MgO}}^{\text{Melt}}) \\ &\quad - \log(a_{\text{SiO}_2}^{\text{Melt}}) - (-0.18) \quad . \quad \text{Eq. (62)} \end{aligned}$$

$D_{\text{In}}^{\text{Am/Melt}}$  can also be expressed by equation 52, where the formal equilibrium constant is expressed as

$$K_3 = \frac{(a_{\text{MgO}}^{\text{Melt}})^2 \cdot (a_{\text{SiO}_2}^{\text{Melt}})^2 \cdot a_{\text{In-Mg-Ts}}^{\text{Am}}}{a_{\text{In}_2\text{O}_3}^{\text{Melt}} \cdot a_{\text{Tr}}^{\text{Am}} \cdot a_{\text{Al}_2\text{O}_3}^{\text{Melt}}}, \quad \text{Eq. (63)}$$

where  $\mu_{\text{Ca}_2\text{Mg}_3\text{In}_2\text{Si}_6\text{Al}_2\text{O}_{22}(\text{OH})_2}^{\text{Am}}$  is written as  $a_{\text{In-Mg-Ts}}^{\text{Am}}$  and  $\mu_{\text{Ca}_2\text{Mg}_5\text{Si}_8\text{O}_{22}(\text{OH})_2}$  is written as  $a_{\text{Tr}}^{\text{Am}}$  for convenience.

Rearranging yields equation 64.

$$K_3 \left( \frac{\gamma_{\text{In}}^{\text{Melt}}}{\gamma_{\text{In-Mg-Ts}}^{\text{Am}}} \right) \frac{a_{\text{Tr}}^{\text{Am}} \cdot a_{\text{Al}_2\text{O}_3}^{\text{Melt}}}{(a_{\text{MgO}}^{\text{Melt}})^2 \cdot (a_{\text{SiO}_2}^{\text{Melt}})^2} = \frac{X_{\text{In-Mg-Ts}}^{\text{Am}}}{X_{\text{In}}^{\text{Melt}}}, \quad \text{Eq. (64)}$$

where  $X_{\text{In}_2\text{O}_3}^{\text{Melt}} = X_{\text{In}}^{\text{Melt}}$ . Again referring back to indium substitutions into amphibole approximately 1/3 of indium substituting into amphibole follow equation 32, which is represented by equation 52. In equation 64  $D_{\text{In}}^{\text{Am/Melt}}$  can be defined by

$$D_{\text{In}}^{\text{Am/Melt}} = \frac{X_{\text{In}}^{\text{Am}}}{X_{\text{In}}^{\text{Melt}}} \tau \quad \text{Eq. (65)}$$

when

$$0.33X_{\text{In}}^{\text{Am}} = X_{\text{In-Mg-Ts}}^{\text{Am}} \quad \text{Eq. (66)}$$

and

$$K_3 \left( \frac{\gamma_{\text{In}}^{\text{Melt}}}{\gamma_{\text{In-Mg-Ts}}^{\text{Am}}} \right) \tau \frac{a_{\text{Tr}}^{\text{Am}} \cdot a_{\text{Al}_2\text{O}_3}^{\text{Melt}}}{(a_{\text{MgO}}^{\text{Melt}})^2 \cdot (a_{\text{SiO}_2}^{\text{Melt}})^2} = \frac{0.33X_{\text{In}}^{\text{Am}}}{X_{\text{In}}^{\text{Melt}}} \tau \quad \text{Eq. (67)}$$

Thus,

$$\frac{K_3'}{0.33} \frac{a_{\text{Tr}}^{\text{Am}} \cdot a_{\text{Al}_2\text{O}_3}^{\text{Melt}}}{(a_{\text{MgO}}^{\text{Melt}})^2 \cdot (a_{\text{SiO}_2}^{\text{Melt}})^2} = D_{\text{In}}^{\text{Am/Melt}}, \quad \text{Eq. (68)}$$

where

$$K_3' = K_3 \left( \frac{\gamma_{\text{In}}^{\text{Melt}}}{\gamma_{\text{In-Mg-Ts}}^{\text{Am}}} \right) \tau. \quad \text{Eq. (69)}$$

The logarithmic transformation of equation 69 is thus

$$\log(D_{\text{In}}^{\text{Am/Melt}}) = \log(K'_3) + \log(a_{\text{Tr}}^{\text{Am}}) + \log(a_{\text{Al}_2\text{O}_3}^{\text{Melt}}) - 2\log(a_{\text{MgO}}^{\text{Melt}}) - 2\log(a_{\text{SiO}_2}^{\text{Melt}}) - (-0.48) \quad \text{Eq. (70)}$$

Equations 62 and 70 describes the variation in the partition coefficient as a function of  $a_{\text{Tr}}^{\text{Am}}$ ,  $a_{\text{Mg-Hbl}}^{\text{Am}}$ ,  $a_{\text{MgO}}^{\text{Melt}}$ ,  $a_{\text{Al}_2\text{O}_3}^{\text{Melt}}$ , and  $a_{\text{SiO}_2}^{\text{Melt}}$ .

### 5.5. Indium Silicates

To the best of my knowledge, indium silicates do not crystallize in natural settings, but have been synthesized in this study. Indium silicates with the formula  $\text{In}_2\text{Si}_2\text{O}_7$  were first synthesized by Ito (1968). Gels were prepared by Ito (1968) with a chemical composition that was stoichiometric  $\text{In}_2\text{Si}_2\text{O}_7$ . From this starting gel, crystalline  $\text{In}_2\text{Si}_2\text{O}_7$  was grown in cold-seal vessels between 450 and 720°C at 150 to 200 MPa, or in air at 1,200°C. Ito (1968) determined that the indium silicate is isostructural with thortveitite, a scandium silicate with the formula  $\text{Sc}_2\text{Si}_2\text{O}_7$ . The isostructural indium silicate is referred to as In-thortveitite. In-thortveitite has been prepared via a gel method by various other materials science studies for use as scintillators (Karazhanov et al., 2011; Messous et al., 1995; Reid et al., 1977; Tsujimoto et al., 1975).

The presence of indium silicates in these experiments allows for an explanation of the narrow range of indium concentration in the melts of this study (Tables 9 and 13). Thermodynamic equilibrium involving In-thortveitite in the experiments presented here can be expressed as:

$$\mu_{\text{In}_2\text{O}_3}^{\text{Melt}} + 2\mu_{\text{SiO}_2}^{\text{Melt}} = \mu_{\text{In}_2\text{Si}_2\text{O}_7}^{\text{In-Thort}} \quad \text{Eq. (71)}$$

and the equilibrium constant can be expressed as:

$$K_4 = \frac{a_{\text{In}_2\text{Si}_2\text{O}_7}^{\text{In-Thort}}}{a_{\text{In}_2\text{O}_3}^{\text{Melt}} \cdot (a_{\text{SiO}_2}^{\text{Melt}})^2} . \quad \text{Eq. (72)}$$

By using equation 72 the concentration of indium in the melt can be expressed as:

$$X_{\text{In}}^{\text{Melt}} = \frac{a_{\text{In}_2\text{Si}_2\text{O}_7}^{\text{In-Thort}}}{K_4' (a_{\text{SiO}_2}^{\text{Melt}})^2} , \quad \text{Eq. (73)}$$

where

$$K_4' = K_2 \gamma_{\text{In}}^{\text{Melt}} \quad \text{Eq. (74)}$$

and

$$X_{\text{In}}^{\text{Melt}} = X_{\text{In}_2\text{O}_3}^{\text{Melt}} . \quad \text{Eq. (75)}$$

The logarithmic transformation of equation 73 yields:

$$\log X_{\text{In}}^{\text{Melt}} = \log a_{\text{In}_2\text{Si}_2\text{O}_7} - 2 \log a_{\text{SiO}_2}^{\text{Melt}} - \log K_4' . \quad \text{Eq. (76)}$$

Given equation 76, it is evident that the concentration of indium in the melt is intimately related to the activity of  $\text{SiO}_2$  the melt and activity of  $\text{In}_2\text{Si}_2\text{O}_7$ . The activity of  $\text{SiO}_2$  in all of the biotite experiments is approximately constant and the melts are at or near quartz saturation. It is also assumed that the activity of  $\text{In}_2\text{Si}_2\text{O}_7$  is also constant, i.e. the melt is saturated with  $\text{In}_2\text{Si}_2\text{O}_7$ . Thus, the activity of  $\text{In}_2\text{O}_3$  is also nearly constant, such that the run products glasses have a mean In concentration of  $410 \pm 30$  ppm ( $1 \sigma_m$ ). In the amphibole experiments, the activity of  $\text{SiO}_2$  may change with time as the Bishop Tuff and Juan de Fuca glass reach equilibrium. Equilibrium may be achieved by lowering the activity of  $\text{SiO}_2$  in the Bishop Tuff, raising the activity in the Juan de Fuca glass, or both. In any case, the activity of  $\text{SiO}_2$ , and thus activity of  $\text{In}_2\text{O}_3$ , in the melt is relative constant resulting in narrow range of In concentration in amphibole/melt run product glasses, which have a mean

In concentration of  $600 \pm 80$  ( $1\sigma_m$ ) ppm. For melts with lower activities of  $\text{SiO}_2$  there is potential for indium enrichment relative to melts with high activity of  $\text{SiO}_2$  in the presence of In-thortveitite.

Table 20

Example of mass balance of indium in Biotite Run 24

Phase	Concentration of In (ppm)	Weight of phase (mg)*	Mass of indium (mg)
<u>Prior to experiment</u>			
InAu alloy	50,000	50	2.50
<u>After experiment</u>			
Melt	410	30	0.01
Biotite	900	1	0.001
Capsule	75	700	0.05
InAu alloy	300	50	0.02
Au foil	75	49	0.00
Inner Au capsule	75	89	0.01
In-thortveitite	600,000	3	1.80
Total			1.89
Starting Indium			2.50
Ending Indium			1.89
Indium unaccounted for			0.61

\* Weights of biotite, amphibole, and In-thortveitite are approximations. Weights of melt, capsule, alloy, Au foil, and inner Au capsule have uncertainty of  $\pm 0.01$  mg. No analysis is available for solution in Biotite Run 24.

A significant proportion of the indium in the starting alloy likely reacts to form In-thortveitite. A mass balance of run product phases containing indium after an experiment has been conducted for Biotite Run 24. In the example given, ~25% (0.61

mg) of indium is unaccounted for (Table 20) after the summation of indium in biotite, melt, Au capsules and foil, InAu alloy and In-thortveitite. The most probable host of this indium is the volatile phase. If the remaining indium is in the volatile phase the run product solution would have ~30,000 ppm indium. This predicted concentration is likely higher (two to three times that of measured solutions) than the actual concentration. Additional indium may also be lost due to the gold capsule. A similar distribution is likely present throughout experiments.

## 5.6. Demonstration of Equilibrium

### 5.6.1. Biotite Equilibrium

In order to use experimentally measured  $D_{\text{In}}^{\text{Bt/Melt}}$  to understand natural systems equilibrium must be demonstrated. In biotite experiments equilibrium is evaluated by comparing  $D_{\text{In}}^{\text{Bt/Melt}}$  with time. To do so, the linear regression of equation 24 was used to calculate a residual for each experiment. Equation 24 was used to calculate a  $D_{\text{In}}^{\text{Bt/Melt}}$  for each experiment based on the  $X_{\text{Annite}}^{\text{Bt}}$ . The measured  $D_{\text{In}}^{\text{Bt/Melt}}$  is then subtracted from the calculated  $D_{\text{In}}^{\text{Bt/Melt}}$  resulting in a residual. This residual is then plotted against run time (Figure 22). It should be noted that experiments with subpopulations or experiments falling off the trend of  $D_{\text{In}}^{\text{Bt/Melt}}$  vs  $X_{\text{Annite}}^{\text{Bt}}$  have been excluded from this plot. The reasoning of exclusion is discussed above and evidence of disequilibrium in these experiments is discussed below. Figure 22 shows that the residual approaches zero with increasing time indicating that experiments are approaching equilibrium.

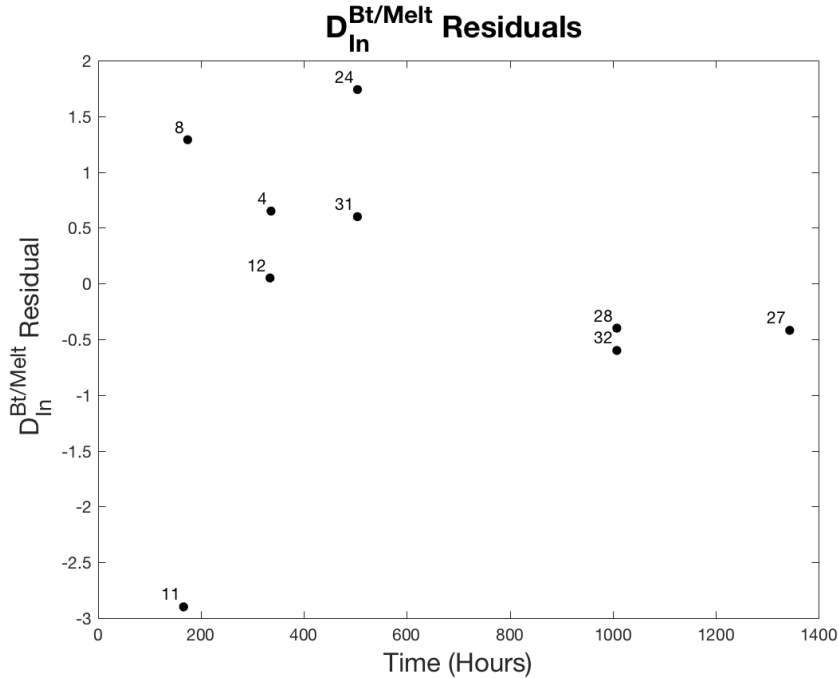


Figure 22: Residual of biotite/melt partition coefficient vs. time showing no systematic change of the partition coefficient with time. Experiments with subpopulation and those falling off the trend of  $D_{In}^{Bt/Melt}$  vs  $X_{Annite}^{Bt}$  have not been plotted (see text for details).

### 5.6.2. *Amphibole Equilibrium*

With regard to amphibole experiments the  $D_{In}^{Am/Melt}$  of experiments can be plotted against time. Figure 23 indicates that with time there is no significant variation from the mean ( $36 \pm 5$  ( $1\sigma_m$ )) with increasing time. Experiments with subpopulations have been excluded (see discussion on disequilibrium).

### 5.7. *Disequilibrium in Partitioning Experiments*

Although both  $D_{In}^{Bt/Melt}$  and  $D_{In}^{Am/Melt}$  are functions of composition, there is some evidence for disequilibrium in several experiments. As mentioned above, there are chemically different subpopulations of biotite (Biotite Run 15 and 23) and

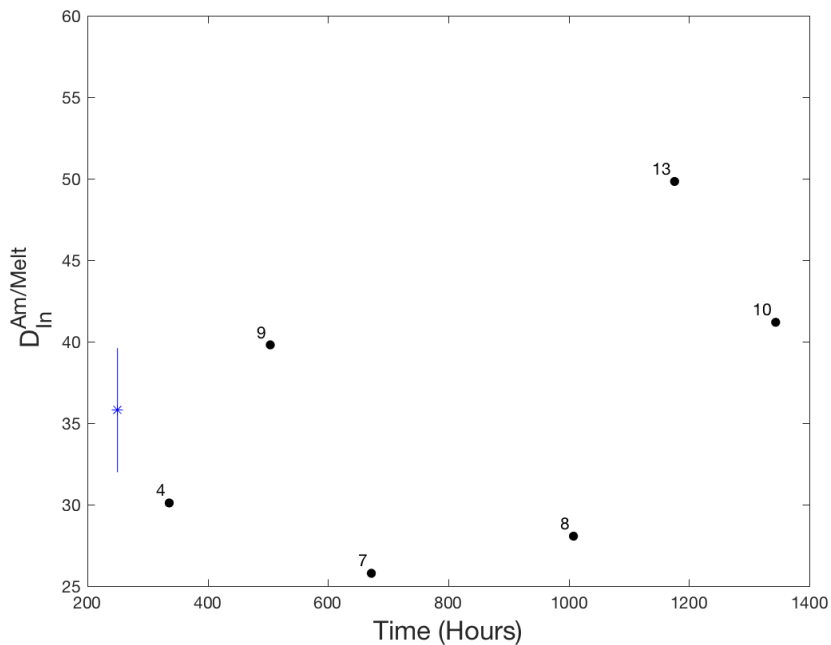


Figure 23: Amphibole/melt partition coefficient vs. time showing no significant change of the partition coefficient with time. Blue point is mean  $\pm$  the standard deviation of the mean ( $1\sigma_m$ )

amphibole (Amphibole Run 6, 11, 14) within single experiments. These subpopulations indicate that the system is in disequilibrium. Despite this disequilibrium, run products generally fit the trends of partition coefficients plotted against biotite and amphibole compositions, respectively. It is interpreted that the experiments that fall significantly off of trends described in Chapter 4, is a result of disequilibrium or compositional variations that are unaccounted for. For amphibole runs, runs with  $D_{In}^{Am/Melt} < 10$  are likely the furthest from equilibrium.

### 5.8. Henry's Law

In some cases the magnitude of a partition coefficient is a function of the concentration of the trace element in the crystal, in addition to temperature, pressure, and major element composition. In an ideal solution, trace elements will follow Raoult's Law where the activity of the trace element is equal to the mole fraction of

that trace element, i.e.  $a = X$ . Deviations from this 1:1 relationship may follow Henry's Law, where the activity of the trace element is equal to the mole fraction of that trace element multiplied by the activity coefficient, i.e.  $a = hX$ , where  $h$  is the Henry's law constant, which is essentially a constant activity coefficient at a suitably low concentration of the trace element in question. At increasingly higher trace element concentrations there is a failure of Henry's Law (Figure 24). After the failure of Henry's Law, the magnitude of partitioning will be a function of the concentration of the trace element. Generally, the failure of Henry's Law in experimental systems occurs at concentration level that is specific to each element-mineral pair and results in a decrease in the partition coefficient (see Harrison (1981), Harrison and Wood (1980), Hoover (1978), Mysen (1978), Pan et al. (2003), Prowatke and Klemme (2006), Watson (1985), and references therein).

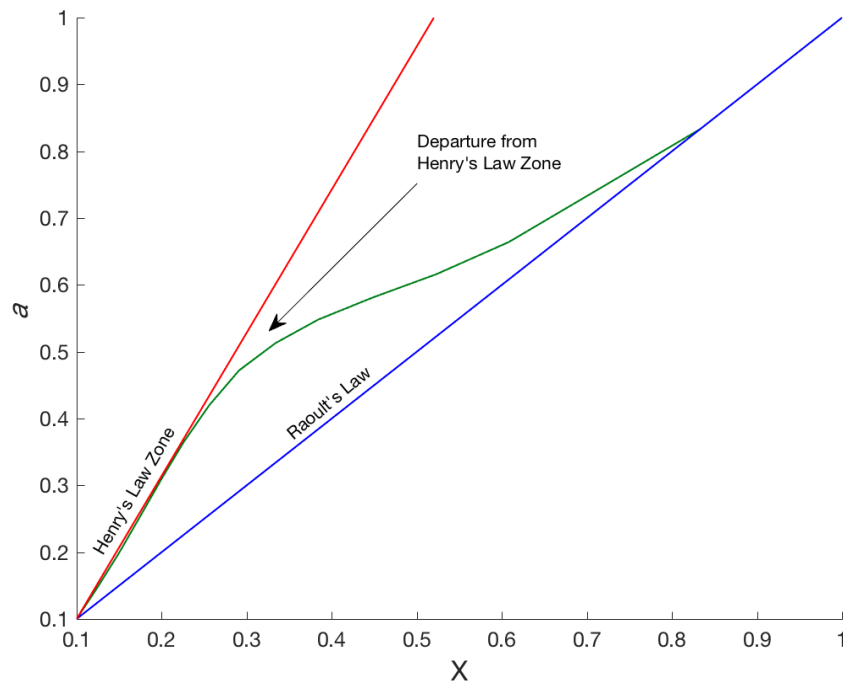


Figure 24: Relationship of Raoult's Law, Henry's Law, and departure from Henry's Law.

The failure of Henry's Law in experimental studies is a consequence of the high levels of doping with trace elements that may be necessary for analytical considerations. As both biotite and amphibole experiments have been doped with high concentrations of indium, problems regarding Henry's Law should be evaluated. To do so, the lattice strain model of Blundy and Wood (1994) is used to estimate both  $D_{In}^{Bt/Melt}$  and  $D_{In}^{Am/Melt}$ . The lattice strain model of Blundy and Wood (1994) is given in equation 77:

$$D_i = D_o \exp \left[ -4\pi E N_A \left( \frac{r_o(r_i - r_o)^2 + \frac{1}{3}(r_i - r_o)^3}{RT} \right) \right], \quad \text{Eq. (77)}$$

where  $D_i$  is the Nernst-type partition coefficient for element  $i$ ,  $D_o$  is the Nernst-type partition coefficient for an element imparting no strain on a crystallographic site with the radius  $r_o$ ,  $r_i$  is the ionic radius of element  $i$ ,  $R$  is the gas constant,  $T$  is temperature in Kelvin,  $N_A$  is Avogadro's number, and  $E$  is the Young's Modulus of the crystallographic site. Parameters used in equation 77 are given in Table 21. The predicted partition coefficients are plotted on an Onuma diagram along with partition

Table 21

Parameters used in lattice strain model of Blundy and Wood (1994)

Variable	Biotite	Amphibole	Reference
$r_o$ (Sc)	0.7	0.7	Shannon (1976)
$r_i$ (In)	0.8	0.8	Shannon (1976)
$D_o$ (Sc)	13.1	35.1	Biotite- Mahood and Hildreth (1983), Amphibole -Nandedkar et al. (2016)
Charge (z)	3	3	
M-O	2.1	2.1	Figure 42 of Hawthorne (1983) where the linear relationship is $M-O = 1.527 + 0.764 * r$
E (Young's Modulus)	366.4	366.4	Bulk Modulus from Figure 1 of Hazen and Finger (1979). Bulk Modulus converted you Young's Modulus using a Poisson ratio of 0.25 after Blundy and Wood (1994)
T (Kelvin)	1023	1073	
Predicted D	9.5	24.3	

Scandium used as proxy for ideal ionic radii and E. M-O is metal-oxygen bond length of scandium.

coefficients for REEs, d-block metals, and measured partition coefficients for both biotite (Figure 25) and amphibole (Figure 26). From these diagrams the predicted partition coefficients fit the trends shown by literature reported partition coefficients vs ionic radii. Measured partition coefficients of biotite are both higher and lower than the estimated partition coefficient. However, these variations do not indicate a failure of Henry's Law as the variation is a function of biotite composition. A failure of Henry's Law would show a decrease in the partition coefficient with increasing indium concentration; however, because the indium concentration of melt is constant the partition coefficient increases. As the partition coefficient increases, it begins to approach and cluster near the predicted partition coefficient (Figure 25). For amphibole, there is a greater risk of Henry's Law failure, because the concentration of indium in amphibole is almost always >1%. The measured partition coefficients

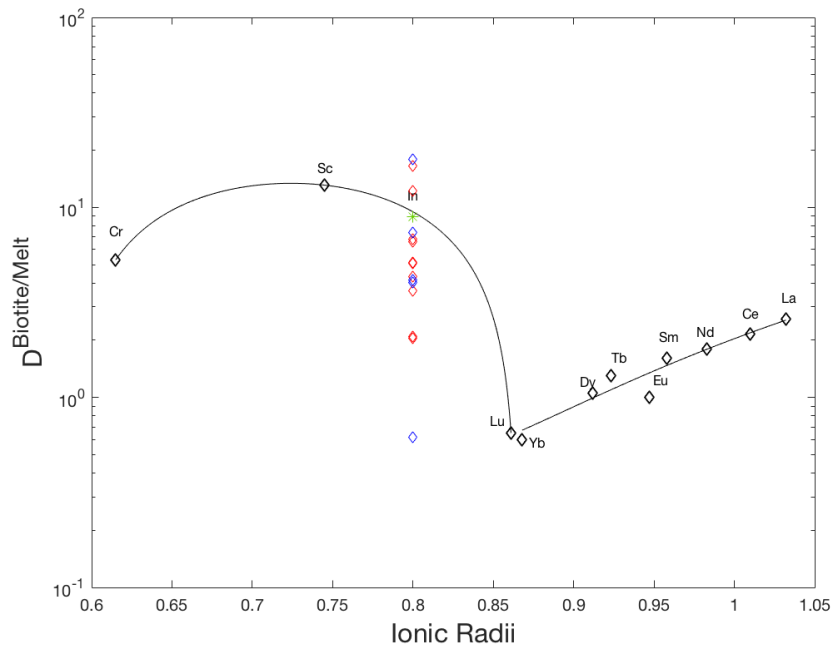


Figure 25: Onuma diagram of partition coefficients for biotite/melt vs. ionic radii. Points in red/blue are experimental partition coefficients for indium. Points in blue are points indicating subpopulations of experiments. Green star is the predicted partition coefficient for indium. All other partition coefficients are from Mahood and Hildreth (1983).

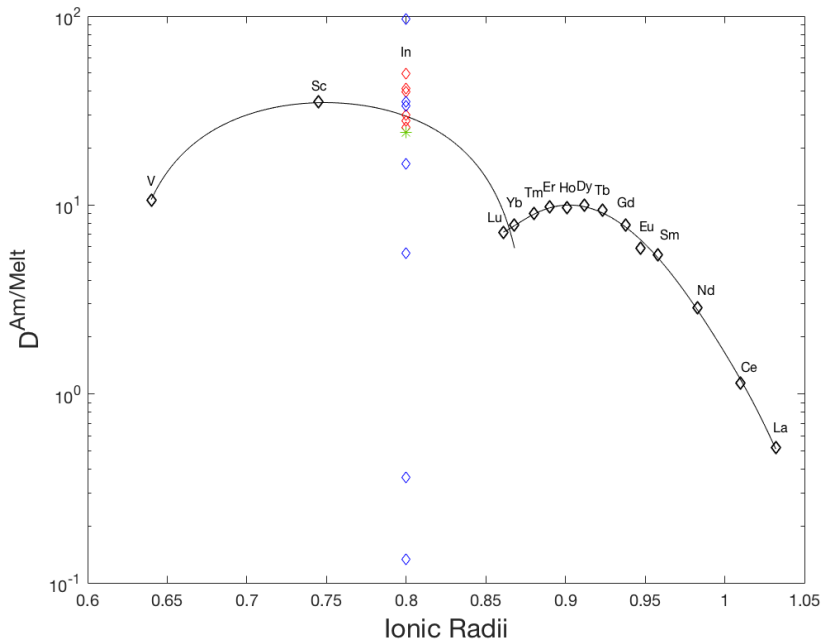


Figure 26: Onuma diagram of partition coefficients for amphibole/melt vs. ionic radii. Points in blue are points indicating subpopulations of experiments. Green star is the predicted partition coefficient for indium. All other partition coefficients are from Nandedkar et al. (2016).

cluster near the predicted partition coefficient (Figure 26) and the average measured partition coefficient would plot slightly above the predicted value. In addition there is no evidence of a decrease in the partition coefficient as a result of increasing concentration of indium as one might expect from previous studies (again see Harrison (1981), Harrison and Wood (1980), Hoover (1978), Mysen (1978), Pan et al. (2003), Prowatke and Klemme (2006), Watson (1985), and references therein).

#### Indium Sequestration Model

Conceptual models of ore formation can be used to as guides for mineral exploration. These models may be concerned with grade and tonnage, or where in space and time deposits are likely to form. The results of experimental studies are used as variables and constraints in the construction of conceptual models.

Conceptual models constructed in this study begin with a melt that evolves through

fractional crystallization and volatile saturation followed by the complete crystallization of the melt. Modeling of indium through the crystallization process can be modeled using the Rayleigh fractionation equation from Rayleigh (1902):

$$\frac{C_i^L}{C_i^{L^\circ}} = F^{\bar{D}-1} \quad , \quad \text{Eq. (78)}$$

where  $C_i^L$  is the concentration of element i in the liquid,  $C_i^{L^\circ}$  is the initial concentration of element i in the liquid,  $F$  is the melt fraction, and  $\bar{D}$  is the bulk partition coefficient. The Rayleigh fractionation equation can be also be defined in terms of masses:

$$\frac{\frac{M_i^L}{M^L}}{\frac{M_i^{L^\circ}}{M^{L^\circ}}} = F^{\bar{D}-1} \quad , \quad \text{Eq. (79)}$$

where  $M_i^L$  is the mass of element i in the liquid,  $M^L$  is the mass of the liquid,  $M_i^{L^\circ}$  is the initial mass of element i in the liquid, and  $M^{L^\circ}$  is the initial mass of the liquid.

The melt fraction remaining can be defined as  $\frac{M_i^{L^\circ}}{M^{L^\circ}}$  thus; equation 79 can be rearranged to yield:

$$M_i^L = M_i^{L^\circ} \cdot F \cdot F^{\bar{D}-1} \quad \text{Eq. (80)}$$

and

$$M_i^L = M_i^{L^\circ} \cdot F^{\bar{D}} \quad , \quad \text{Eq. (81)}$$

where equation 81 is from Simon et al. (2003). Particular care should be taken when applying equation 81, as its primary use is to economic geologists. It should be explicitly noted that equation 81 varies from the Rayleigh fractionation equation (equation 78) in that concentrations are not used and the “-1” in the exponent is not present. The traditional Rayleigh fractionation equation is not adequate in the

modeling of ore deposits concerned with the mass (i.e. tonnage), thus the economic geologist Rayleigh fractionation equation (equation 81) is necessary. Equation 81 can then be used to calculate the amount of trace element *i* sequestered in the crystalline phases and the amount remaining in the liquid prior to volatile saturation. Post-volatile saturation, the mass of *i* can be determined through a mass balance:

$$C_i^{XL} = \bar{D}_i^{XL/V} \cdot C_i^V, \quad \text{Eq. (82)}$$

where  $C_i^{XL}$  is the concentration of element *i* in the crystal phase(s),  $C_i^V$  is the concentration of element *i* in the vapor phase, and  $\bar{D}_i^{XL/V}$  is the crystal/vapor bulk partition coefficient. Equation 82 can be written in terms of mass and rearranged to yield:

$$M_i^{XL} = \bar{D}_i^{XL/V} \cdot \frac{M_i^V}{M^V} \cdot M^{XL}, \quad \text{Eq. (83)}$$

where  $M_i^{XL}$  is the mass of element *i* in the crystal phase(s),  $M^{XL}$  is the mass of the crystal phase(s),  $M_i^V$  is the mass of element *i* in the vapor phase, and  $M^V$  is the mass of the vapor phase. The mass balance of element *i* is defined as:

$$M_i = M_i^{XL} + M_i^V + M_i^L, \quad \text{Eq. (84)}$$

where  $M_i$  is the mass of element *i* in the liquid immediately prior to saturation with the volatile phase. Substituting equation 83 into equation 84 and rearranging yields

$$M_i^V = \frac{M_i - M_i^L}{\bar{D}_i^{XL/V} \cdot \frac{1}{M^V} \cdot M_i^{XL} + 1}. \quad \text{Eq. (85)}$$

An iterative process combined with equations 81 and 85, and a mass balance equation can predict the efficiency of ore formation. The efficiency of ore formation is the efficiency at which the trace element is removed from the melt into the ore fluid and defined by:

$$E_i = \frac{M_i^V}{M_i^{\text{System}}} \cdot 100 \quad , \quad \text{Eq. (86)}$$

where  $E_i$  is the efficiency of removal and  $M_i^{\text{System}}$  is the total mass of element  $i$  in the liquid when  $F = 1$ . The  $E_i$  defined here is roughly equal to that of  $E_i$  of Candela and Holland (1986). The difference between the  $E_i$  presented here and that of Candela and Holland (1986) is the  $E_i$  of Candela and Holland (1986) is integrated from  $F=0$  to  $F=1$ , while the  $E_i$  presented here is the instantaneous  $E_i$  for a given melt fraction. When both methods are compared at  $F=0$ , the  $E_i$  is equal, given the crystalline phases sequestering element  $i$  crystallize in the same proportions throughout the crystallization of melt, no hydrous phases are crystallized, and the only volatiles in the melt is water.

With regard to indium, there are three primary models that will be evaluated based on granite type, ferromagnesian phases, and volatiles. The models are the I-type model, which contains biotite and amphibole; the S-type model, which contains only biotite; and the A-type model, which contains biotite and will focus on fluorine-rich rhyolites (topaz rhyolites). The models are designated I-, S-, or A- type to distinguish the granitic system that fits the model being discussed and will be referred to as such. The parameters for each model have been chosen to highlight changes in  $E_{In}$ . For instance I-type systems commonly contain both biotite and amphibole, while S-type systems lack amphibole (Chappell and White, 2001) and a comparison between the two systems, when  $D_{In}^{\text{Bt/Melt}}$  is the same, is a valuable exercise. Although A-type systems may have amphibole present (Whalen et al., 1987), those that do not generally contain iron-rich biotite (Anderson and Bender, 1989), as well

as significant F. Thus, the A-type system and can be used as a comparison to the S-type system, which may also contain iron-rich biotite, but allows the presence of F to be evaluated. Comparison of these three models can then be used to evaluate the conditions that promote the maximize  $E_{In}$ . In all three models to be discussed, three stages of crystallization will be evaluated. Stage one is the crystallization of the melt, during which biotite and/or amphibole are not stable and the crystallization products are feldspar. The second stage includes the crystallization of the melt prior to volatile saturation, during which biotite and/or amphibole are stable. The third stage is the

Table 22

	Model		
	I-Type	S-Type	A-Type
<b>Stage One</b>			
Initial Water	2%	2%	2%
Initial Chlorine	0	0	0.15%
Initial Fluorine	0	0	1.25%
Melt Fraction	0.5	0.5	0.5
<b>Stage Two</b>			
Mass Fraction of Biotite	9%	16%	15%
Mass Fraction of Amphibole	7%	0%	0
Amphibole/Melt D	336	-	-
Biotite/Melt D	1.5	1.5	0.20
Melt Fraction (of Stage)	0.64	0.63	0.42
Total Melt Fraction	0.32	0.32	0.21
<b>Stage Three*</b>			
Vapor/Melt D In	50	50	50**
Vapor/Melt D Cl	-	-	10
Vapor/Melt D F	-	-	0.5
Efficiency of Ore Formation	15%	82%	98%

For references of stage one variable and details on calculations see text.  
 \*Biotite and amphibole mass fractions and partition coefficients equal to stage two. \*\*Maximum and various as a function of Cl in the evolving melt.

crystallization of the melt after volatile saturation, during which biotite and/or amphibole are stable. For each model the melt has a volume of  $1 \text{ km}^3$ , a density of  $2,300 \text{ kg/m}^3$  (Ochs and Lange, 1999), and an initial indium concentration of 0.05 ppm (Rudnick and Gao, 2003). Pressure is set at 200 MPa, the starting temperature of  $1000^\circ\text{C}$ , the final temperature will be below the solidus ( $<700^\circ\text{C}$ ), and initial water content of 2 wt%. Parameters (biotite mass, amphibole mass, Cl, F, etc.) and results of each stage are given in Table 22 and discussed below. The Cl and F concentrations for each I- and S- type models are negligible (0.05 wt% and  $<1000$  ppm, respectively) and thus are approximated as zero.

The I-type model has the lowest efficiency of removal, due to the crystallization of significant quantities of magmatic biotite and amphibole. The mass of biotite (9%) and amphibole (7%) used in the model are converted from the modal percent (7% biotite, 5% amphibole) of each mineral reported by Bateman (1992) for the Half Dome Equigranular Granodiorite of the Tuolumne Intrusive Suite.  $D_{\text{In}}^{\text{Bt/Melt}}$  (1.5) is calculated based on the  $X_{\text{Annite}}^{\text{Bt}}$  of Y-14 biotite and  $D_{\text{In}}^{\text{Am/Melt}}$  is the average  $D_{\text{In}}^{\text{Am/Melt}}$  (36) of this study, making indium mildly compatible biotite and extremely compatible in amphibole. The first stage of the model begins at  $1000^\circ \text{C}$ . The melt crystallizes 50% until the temperature is  $\sim 750^\circ \text{C}$  at which point biotite and amphibole are stable. During the second stage the remaining melt crystallizes 64% (the total melt remaining is 32% of the original melt) sequestering indium (following equation 81) in both biotite and amphibole until volatile saturation at 6% water. After volatile saturation the MVP is formed and indium can partition into biotite, amphibole, and the MVP.  $D_{\text{In}}^{\text{Vapor/Melt}}$  for this model is 50 (extremely compatible).

Using equations 81 and 85, and a mass balance the mass of indium in the vapor phase can be calculated after the melt as completely crystallized. The efficiency of removal for the I-type model is ~15%.

The second model is the S-type model. The S-type model has a high efficiency of removal, but is lower than the A-type model. The S-type model contains only biotite and no amphibole. The mass of biotite (16%) is converted from the median modal percent of biotite (12%) of the Keotong Suite of the Lachlan Fold Belt (Price, 1983). This estimate is reasonable as mafic S-type granites can contain up to 35 modal % biotite (Chappell and White, 2001).  $D_{In}^{Bt/Melt}$  (1.5, mildly compatible and used to highlight the change in  $E_{in}$  when amphibole is removed) and  $D_{In}^{Vapor/Melt}$  (50, extremely compatible) is the same used in the I-type model. Similar to the I-type model the first stage starts at 1000° C and the melt crystallizes 50% until the temperature is ~750° C, at which point biotite is stable. During the second stage the remaining melt crystallizes 63% (the total melt remaining is 31.5% of the original melt) sequestering indium (following equation 81) in biotite until volatile saturation at 6% water. Again using equations 81 and 85, and a mass balance the mass of indium in the vapor phase can be calculated after the melt as completely crystallized. The efficiency of removal for the S-type model is ~82%. It should be noted that S-type magmas frequently have iron-rich biotite such that indium will behave incompatibly. In this scenario the efficiency of removal will be similar to the A-type model below.

The third model is the A-type (topaz rhyolite) model. This model differs from both the I- and S-type models due to the significant concentrations of fluorine (>1000

ppm) in the melt. In addition to the 2 wt% water, the melt has 1.25 wt% F and 0.15 wt% Cl. These concentrations are equal to that of the Spor Mountain Vitrophere reported by Webster et al. (1987) and Webster (1990). In this model, it is assumed these concentrations represent the initial Cl and F in the melt at Spor Mountain. The model contains only biotite (11 modal %, 15 wt%) and no amphibole. The modal % of biotite is again from the Spor Mountain Rhyolite as reported by Christiansen et al. (1980). The first stage of the model is equal to that of the first stage of both I- and S-type model, where 50% of the melt is crystallized. This increases the concentration of water to 4% and because there are no phases to sequester fluorine or chlorine their concentrations become 2.5 wt% and 0.3 wt %, respectively. Due to the increase in fluorine the solubility of water in the melt increases, delaying water saturation (Holtz et al., 1993). Once the water content of the melt reaches 4% biotite becomes stable (Webster et al., 1987) and stage two begins.

At this point the model increases in complexity. In order to estimate the efficiency of removal, the amount of crystallization needed to saturate with a volatile phase must be known. Because the melt in this model contains fluorine the point of volatile saturation changes based on the fluorine concentration. The point at which the melt becomes volatile saturated is calculated using the relationship between volatile saturation and F concentration determined by Holtz et al. (1993) for haplogranite melts. Likewise, once biotite is stable both fluorine and chlorine can exchange with OH in the hydroxyl site of the biotite, removing fluorine and chlorine from the melt. The amount of fluorine and chlorine exchanging between biotite and melt is dependent on the fluorine and chlorine concentration of the melt and thus

requires the use of a formal equilibrium constant, as opposed to a partition coefficient (Candela, 1986). Candela (1986) derived equations to predict the mole fraction of F, Cl, and OH in magmatic apatite based on the concentration of F and Cl in melt, the mole fraction of OH in the melt, and a given set of equilibrium constants. This approach can also be applied to magmatic biotite in order to provide an estimate of the mass of F, Cl, and water removed from the melt into biotite. The first task in this approach is to calculate the relevant equilibrium constants. To do so the mole fractions of F, Cl, and OH in biotite from Spor Mountain, as well as the water, fluorine, and chlorine content of Spor Mountain melt must be known. Biotite from Spor Mountain has a mole fraction of F, Cl, and OH equal to 0.32, 0.04, and 0.64, respectively (Dailey, 2016) and the melt has 1 wt % water, 1.25 wt% F, and 0.15 wt% Cl (Webster et al., 1987). Given these variables the relevant equilibrium constants ( $K_{12}$  and  $K_{13}$  as defined by Candela (1986)) can be calculated. These equilibrium constants are equal to 1.16 and 39.8, respectively. Assuming these equilibrium constants are valid in the model, the mole fraction of F, Cl, and OH of crystallizing biotite can be predicted as a function of the F, Cl, and water content of the melt. Given that this process is circular in nature (i.e. the concentration of F in melt must be known to calculate the mole fraction of F in biotite, but the amount of F in the biotite affects the concentration of F in the melt) the process is coupled with an iterative mass balance. This iterative process results in a melt that must crystallize 42% during the second stage (the total melt remaining is 21% of the original melt), sequestering indium in biotite following equation 81, until volatile saturation at 9% water. Due to the iron-rich nature of biotite from Spor Mountain ( $X_{\text{Annite}}^{\text{Bt}} = 0.84$ ) (Dailey, 2016),

$D_{\text{In}}^{\text{Bt/Melt}}$  is 0.2 (incompatible) and calculated for  $X_{\text{Annite}}^{\text{Bt}} = 0.39$  (the limit of the linear relationship of  $D_{\text{In}}^{\text{Bt/Melt}}$  vs  $X_{\text{Annite}}^{\text{Bt}}$ ). Note that in this model ignores any effect Cl and F has on  $D_{\text{In}}^{\text{Bt/Melt}}$ . The F concentration of the melt will be 5.5% and the Cl concentration will be 0.6 wt% after stage two. After volatile saturation, indium, chlorine, and fluorine can partition between the melt, crystal, and volatile phase. The amount of fluorine, chlorine, and water in the biotite is determined as described above. The mass of fluorine and chlorine in the melt is determined by equation 81 with  $D_{\text{F}}^{\text{Vapor/Melt}}$  equal to 0.5 (Webster, 1990) and  $D_{\text{Cl}}^{\text{Vapor/Melt}}$  equal 10 (Webster and Holloway, 1988) and the mass of fluorine and chlorine in the volatile phase is calculated by mass balance. The mass of indium in the melt, crystals, and volatile phase is then calculated using equations 81 and 85, and a mass balance, where the maximum  $D_{\text{In}}^{\text{Vapor/Melt}}$  is 50 (extremely compatible) and varies (from 3 to 50) with the chlorine concentration in the evolving melt (Figure 20). The efficiency of removal for the A-type model is the highest of the three models at 98%.

From Table 22 and discussed in the text above it is easily seen that the highest efficiency of removal occurs in A- or S- type melts where amphibole is not present and the biotite is iron-rich, such that indium is incompatible. Additionally, when In is modeled as an incompatible element, the effect of delayed volatile saturation (due to significant F in the melt >1000 ppm) will result in a higher efficiency of removal of indium relative to compatible metals (i.e. copper). S-type melts also have a high efficiency of removal, so long as the amount of biotite is not >20 modal percent and/or  $X_{\text{Annite}}^{\text{Bt}}$  does not approximate the phlogopite endmember ( $X_{\text{Annite}}^{\text{Bt}} = 0$ ). The addition of amphibole to the crystallization products drastically reduces the efficiency

of removal, such that for each modal percent of amphibole added, the efficiency of removal decreases ~30%.

### 5.9. Exploration Vectors

The previously discussed models provide insights into the conditions that are most likely to form indium-bearing deposits. These insights are termed exploration vectors and can be used to aid the exploration enterprise. Given that the A-type model has the highest efficiency of removal, the conditions and variables used in this model are primary exploration vectors. The first exploration vector concerns the ferromagnesian phases that occur in the genetically-related granitic rocks that are associated with the prospect in outcrop or drill core. Rocks that contain minimal biotite are favored over rocks containing significant biotite or amphibole

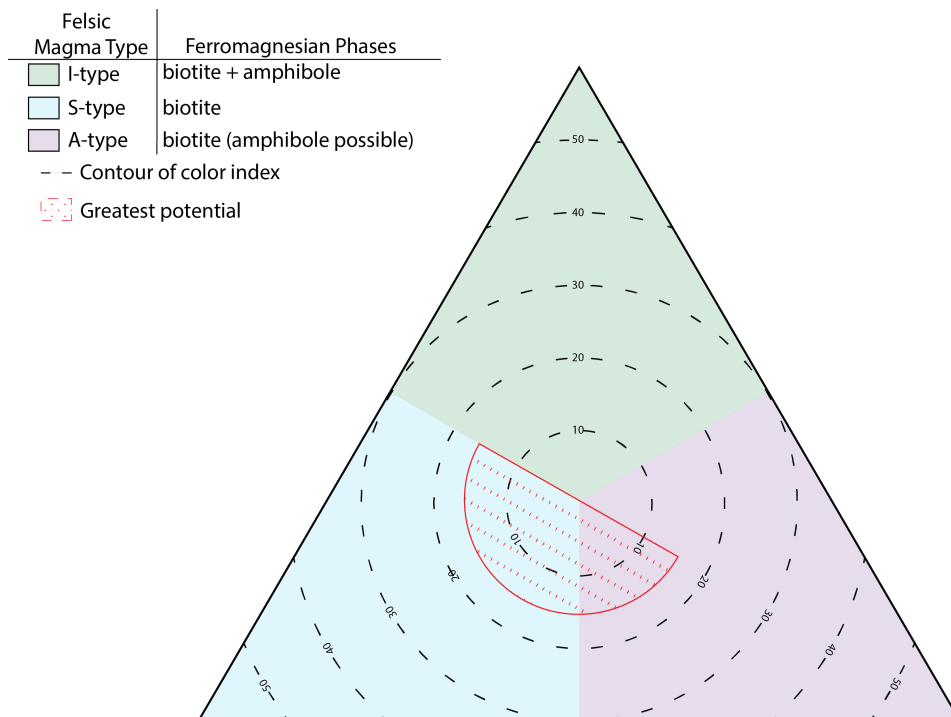


Figure 27: Ternary showing which magma types have the greatest potential of being associated with indium-bearing deposits. Color indices from Anderson and Bender (1989) and Chappell and White (2001). Figure is generalized and assumes that the A-type granites in the zone of greatest potential lack amphibole and resemble topaz rhyolites.

(hornblende), bearing in mind the presence of hornblende will drastically decrease the potential of finding associated indium-bearing deposits. The second exploration vector involves the composition of biotite, such that iron-rich biotite ( $X_{\text{Annite}}^{\text{Bt}} > 0.35$ ) is favored over magnesium-rich biotite ( $X_{\text{Annite}}^{\text{Bt}} < 0.35$ ). In rocks that have iron-rich biotite, indium would have behaved incompatibly during their crystallization. The third exploration vector is the presence of other volatiles in the melt phase. If the melt contains F the solubility of water in the melt will increase, promoting late stage volatile saturation. So long as indium behaves incompatibly, delaying volatile saturation will result in the increase of the ratio of the efficiencies of removal of indium relative to that of compatible elements (such as copper).

Once these exploration vectors have been defined, they can be combined with information about known deposit types to identify which of these deposits may serve as indium hosts. First, it is necessary to constrain which magmas, in light of the exploration vectors, are most likely to concentrate indium. The conceptual model in Figure 27 combined with

the models described above, show the three major magma types (I, S, and A) separated into tectonic setting and contoured according to their color index (i.e. percent of dark-colored

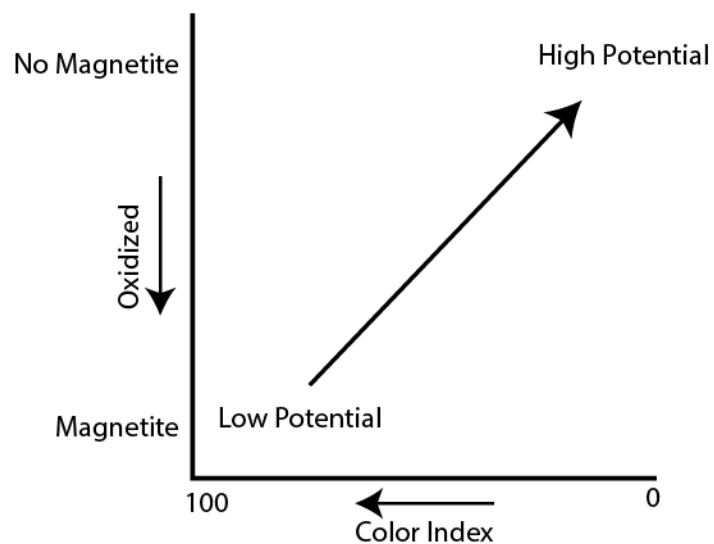


Figure 28: Relationship of oxidation and color index to the potential for being associated with indium-bearing deposit.

phases (biotite, hornblende, etc.). Plotted over the contour intervals, are shaded regions showing conditions that favor the maximum efficiency of removal. Additionally, given the influence of oxygen fugacity on the composition of biotite, a simple relationship between color index and the presence of magnetite can be related to the potential of being associated with an indium-bearing deposit (Figure 28).

Given that I-type magmas commonly contain hornblende, deposits associated with them (i.e. porphyry copper) have a very low potential for forming an indium-bearing deposit, thus deposits associated with I-type magmas will not be considered. The types of deposits to be considered are those associated with A- or S-type melts. As discussed above (Chapter 1) Climax-type molybdenum deposits are often associated with high fluorine, A-type melts and thus present a higher potential for being associated with indium, assuming suitable host minerals are present.

Peripherally related to A-type melts and Climax-type deposits is the low sulfidation Mo, Ag, base metal mineralization in the Valles caldera, New Mexico (Hulen et al., 1987). Given the mineralization is at the site of an active geothermal system and interpreted to be the result of Climax-type deposit formation at depth, there is a potential for low-sulfidation deposits to host indium. Low-sulfidation deposits bearing indium have been described in Argentina (Dill et al., 2013; Jovic et al., 2011) and most notably the Toyoha deposits in Japan (Ishihara et al., 2006; Ohta, 1991; Yajima and Ohta, 1979). Interestingly, the fluid responsible for the second stage of mineralization at Toyoha has been interpreted to be sourced from an ilmenite-series granitoid (Ohta, 1991; Yajima and Ohta, 1979). On the basis of the exploration vectors outlined here, it can be inferred the ilmenite-series granitoid responsible for

indium mineralization lacked significant amphibole ( $\ll 1$  modal %) and contained minimal biotite during crystallization. Additionally, W, Mo, and Sn skarns are associated with A- or S-type melts (Meinert, 1995). The final deposit type that should be considered are Sn-W porphyry deposits. As discussed in Chapter 1, magmas having high HF/H<sub>2</sub>O ratios (Candela, 1989a) and that genetically-related to A- or S-type granites (*s.l.*) (Sinclair, 1996) are commonly associated with W and Sn bearing porphyry/vein-stockwork deposits. Assuming that there is minimal biotite associate with these magmas, they have a potential to be indium-bearing, again assuming adequate indium host minerals are present.

Of special note in this discussion is the Mount Pleasant deposit in New Brunswick, Canada. In the author's opinion, Mount Pleasant displays characteristics that are ideal for indium exploration and should be used as a direct comparison to the exploration vectors discussed here. An overarching description of Mount Pleasant is that it is a Sn-W-Mo and In-bearing deposit associated with reduced (Yang and Lentz, 2005), fluorine-rich, and high-silica granites (Kooiman et al., 1986; Sinclair, 1994). Comparing these characteristics to the exploration vectors shows continuity between conceptually derived results and real world application. The associated granites contain no amphibole and minimal biotite (Inverno and Hutchinson, 2006; Yang and Lentz, 2005). The biotite that has been characterized by Yang and Lentz (2005) has a Mg/(Mg+Fe) ratio of ~0.01. I suggest that its iron-rich nature will also result in  $D_{\text{In}}^{\text{Bt/Melt}} < 1$ , similar to that of a biotite with  $X_{\text{Annite}}^{\text{Bt}} > 0.35$ . In addition, the  $f_{\text{O}_2}$  of the magmas were likely between QFM -1 to QFM -2 (Yang and Lentz, 2005). The host granite has 0.3 to 1 wt% F (Kooiman et al., 1986; Sinclair, 1994), which during

crystallization would result in volatile saturation at a later stage relative to a F-free system. Likewise, the granites have been classified A-type (topaz) granites (Inverno and Hutchinson, 2006; Kooiman et al., 1986; Sinclair et al., 2007; Taylor et al., 1985; Taylor, 1992). Mount Pleasant also exhibits indium host minerals including roquesite, sphalerite, stannite, stannoidite, chalcopyrite, pyrite, and several other sulfide minerals (Sinclair et al., 2006).

One deposit type not yet discussed are VMS deposits. Given that the role of magmas in the formation of VMS deposits, aside from providing heat, is unclear the application of the experimental results discussed here to their formation is problematic. For these exploration vectors to be applied to a VMS system it must be assumed that some of the metal present is sourced from the underlying magma chamber. This has been suggested for Au in VMS deposits (i.e. Franklin et al. (2005), Hannington et al. (1999), and Large et al. (2001)). If this is assumed, deposits that are associated with felsic magmatism are more likely to be indium-bearing. The most likely VMS deposits to show felsic magmatism are the bimodal-mafic and bimodal-felsic systems as described by Barrie and Hannington (1999). This coincides with observations made by Ishihara and Endo (2007) concerning the indium-bearing Japanese Kuroku deposits, which are bimodal-felsic type deposits (Barrie and Hannington, 1999). However, various other Japanese deposits, such as the Besshi deposits are mafic-siliclastic types (Barrie and Hannington, 1999) and have the highest indium tonnage (Ishihara and Endo, 2007). The role magmatism (felsic or mafic) plays in the input of metals into VMS systems requires additional work, although it could be suggested that VMS deposits that are enriched in indium have

felsic magmatic sources. For this suggestion to be evaluated, the behavior of indium in VMS forming environments needs to be constrained. If the grade and tonnage of indium found in VMS deposits is greater than what can be sourced by purely hydrothermal processes, the excess indium may be magmatic in origin.

## Chapter 6: Conclusions

Experiments have been conducted on the partitioning of indium between coexisting crystalline, vapor, and melt phases in felsic-magmatic systems. Experimental results are consistent with  $D_{\text{In}}^{\text{Bt/Melt}}$  ranging from  $0.6 \pm 0.1$  ( $1 \sigma_m$ ) to  $16 \pm 3$  ( $1 \sigma_m$ ) and is a function of the composition of the biotite, such that an increasing  $X_{\text{Annite}}^{\text{Bt}}$  results in a decreasing  $D_{\text{In}}^{\text{Bt/Melt}}$ .  $D_{\text{In}}^{\text{Am/Melt}}$  is  $36 \pm 4$  ( $1 \sigma_m$ ).  $D_{\text{In}}^{\text{Vapor/Melt}}$  ranges from 2.7 to 31 with a mean of  $17 \pm 5$  and its functional dependence on the concentration of Cl in the aqueous phase and other variable remain to be elucidated. These results aid in constraining the behavior of indium during the crystallization of felsic magmas and provide insight into conditions that are favorable for the formation of indium-bearing deposits. These exploration vectors indicate that the crystallization of I-type magmas containing significant amphibole (hornblende) and biotite will result in a low efficiency of removal. Conversely, A- or S-type magmas containing no amphibole (hornblende) and minimal iron-rich biotite create a scenario where indium behaves incompatibly and results in the highest efficiency of removal. Deposits associated with A- or S-type magmas are thus prime candidates for indium exploration.

## Appendices

### Appendix A: Co-Pd Oxygen Fugacity Sensors

CoPd  $f_{O_2}$  sensors were placed within vessels to monitor the oxygen fugacity of experimental runs. These sensors are constructed after Taylor et al. (1992), who used binary alloys as a proxy for the oxidation state of a system. Sensors are constructed by placing the oxidizing metal (Co) in the presence of Pd, and subjecting the mixture to the P-T conditions of interest. The resulting alloy has a mole fraction of Co that can be equated to an oxygen fugacity through equation A.1 from Taylor et al. (1992):

$$\log f_{O_2} (Co, Pd) = -2 \log X_{Co} - \frac{1}{2.3025RT} \left( (491649 - 508.527T + 122.6909T \log T - 0.025187^2) + \left( 2(1 - X_{Co})^2 (-9.76T + 16445(4X_{Co} - 1)) \right) \right), \quad \text{Eq. (A.1)}$$

where  $X_{Co}$  is the mole fraction of cobalt, R is the gas constant ( $8.314 \text{ J mol}^{-1} \text{ K}^{-1}$ ), and T is temperature in Kelvin. The working temperature range for CoPd sensor is 973 to 1473 K.

Sensors used in this study were contained inside platinum capsules of 2, 3, or 5 mm outer diameter, 0.127 mm thickness, and 5-17 mm in length. Yttrium-stabilized, zirconium oxide paper was used to line the platinum capsule and prevent the Co and Pd from alloying with the capsule. Initially small Pd nuggets were added, followed by a mixture of Co + water, which were injected into the capsule via a hypodermic needle. The ratio of Pd to Co + water was ~0.5. Due to the larger size of the Pd nuggets, initial sensors did not produce homogenous CoPd alloys and were unusable. Later sensors were constructed by mixing Co powder (<2  $\mu\text{m}$ ) and Pd powder (74  $\mu\text{m}$ ) into a ratio of ~ 1:3 and pelleting the mixture. Once placed in

capsules ~20  $\mu\text{L}$  of water was added. Finally, a cap of the yttrium-stabilized zirconium oxide paper is placed on top of the CoPd pellet, and the capsule is welded shut. The ratios of Co to Pd ensure that upon completion of the experiment both a binary alloy and a metal monoxide are present.

After the completion of the experiments, the capsules are opened and inspected for the presences of a binary alloy and metal monoxide. The metal monoxides are identified by the blue color of CoO. The binary alloys are then mounted in epoxy, polished, and analyzed via EPMA. Under the conditions of these experiments the mole fraction of Co in the alloy at NNO is ~0.3

## Appendix B: Composition of NBS 610

NBS 610 (NISTRM 610) is the primary standard used for indium analyses performed in this study, as its indium concentration is approximately that of run products. Table B contains the preferred values of NBS 610 from Jochum et al. (2011).

Table B  
Composition of NBS 610 (NISTRM610)

NBS 610														
SiO <sub>2</sub>	69.7	±	0.5	wt%	Zn	460	±	18	ppm	Pr	448	±	7	ppm
Na <sub>2</sub> O	13.4	±	0.3	wt%	Ga	433	±	13	ppm	Nd	430	±	8	ppm
CaO	11.4	±	0.2	wt%	Ge	447	±	78	ppm	Sm	453	±	11	ppm
Al <sub>2</sub> O <sub>3</sub>	1.95	±	0.04	wt%	As	325	±	18	ppm	Eu	447	±	12	ppm
H	15	±		ppm	Se	138	±	42	ppm	Gd	449	±	12	ppm
Li	468	±	24	ppm	Br	93	±		ppm	Tb	437	±	9	ppm
Be	476	±	31	ppm	Rb	426	±	1	ppm	Dy	437	±	11	ppm
B	350	±	56	ppm	Sr	516	±	1	ppm	Ho	449	±	12	ppm
F	304	±		ppm	Y	462	±	11	ppm	Er	455	±	14	ppm
Mg	432	±	29	ppm	Zr	448	±	9	ppm	Tm	435	±	10	ppm
P	413	±	46	ppm	Nb	465	±	34	ppm	Yb	450	±	9	ppm
S	575	±	32	ppm	Mo	417	±	21	ppm	Lu	439	±	8	ppm
S	575	±	32	ppm	Rh	1.29	±	0.07	ppm	Hf	435	±	12	ppm
Cl	274	±	67	ppm	Pd	1.21	±	0.44	ppm	Ta	446	±	33	ppm
K	464	±	21	ppm	Ag	251	±	9	ppm	W	444	±	29	ppm
K	464	±	21	ppm	Cd	270	±	16	ppm	Re	49.9	±	3.7	ppm
Sc	455	±	10	ppm	In	434	±	19	ppm	Pt	3.12	±	0.08	ppm
Ti	452	±	10	ppm	Sn	430	±	29	ppm	Au	23.6	±	1.7	ppm
V	450	±	9	ppm	Sb	396	±	19	ppm	Tl	59.6	±	2.8	ppm
Cr	408	±	10	ppm	Te	302	±		ppm	Pb	426	±	1	ppm
Mn	444	±	13	ppm	Cs	366	±	9	ppm	Bi	384	±	26	ppm
Fe	458	±	9	ppm	Ba	452	±	9	ppm	Th	457.2	±	1	ppm
Co	410	±	10	ppm	Ba	452	±	9	ppm	U	461.5	±	1	ppm
Ni	459	±	4	ppm	La	440	±	10	ppm	CO <sub>2</sub>	0.0002	±		wt%
Cu	441	±	15	ppm	Ce	453	±	8	ppm	H <sub>2</sub> O	0.013	±		wt%

Composition from Jochum et al. (2011)

## Appendix C: EPMA of Starting Materials

Table C: EPMA of starting materials (wt%)

SiO <sub>2</sub>	Al <sub>2</sub> O <sub>3</sub>	TiO <sub>2</sub>	FeO	MgO	MnO	CaO	Na <sub>2</sub> O	K <sub>2</sub> O	Cl	In <sub>2</sub> O <sub>3</sub>	Total
<b>Juan de Fuca Basalt (Analysis by John Nance (LMDR))</b>											
50.9	14.0	1.9	12.0	6.9	0.21	11.2	2.7	0.08	b.d.	b.d.	99.9
50.8	13.8	1.9	12.0	7.0	0.19	11.3	2.7	0.09	b.d.	b.d.	99.8
51.0	14.0	1.9	11.8	7.1	0.19	11.2	2.8	0.09	b.d.	b.d.	100.0
50.7	13.8	1.9	12.0	7.1	0.20	11.3	2.7	0.08	b.d.	b.d.	99.7
50.9	13.8	1.9	11.8	7.1	0.18	11.0	2.7	0.09	b.d.	b.d.	99.5
50.2	13.8	1.9	11.7	6.9	0.17	10.8	2.8	0.10	b.d.	b.d.	98.3
50.6	13.9	1.9	12.3	6.8	0.23	11.1	2.7	0.09	b.d.	b.d.	99.6
51.0	13.9	1.9	12.0	7.0	0.22	11.2	2.8	0.09	b.d.	b.d.	100.1
50.9	13.5	1.9	11.8	6.9	0.21	11.3	2.8	0.09	b.d.	b.d.	99.5
51.3	14.0	1.9	12.2	7.1	0.22	11.3	2.8	0.08	b.d.	b.d.	101.0
51.3	14.0	1.9	12.1	7.1	0.20	11.3	2.8	0.09	b.d.	b.d.	100.9
51.2	14.1	1.9	12.0	7.2	0.21	11.4	2.8	0.09	b.d.	b.d.	100.8
51.1	13.9	2.0	11.8	7.1	0.18	11.1	2.7	0.07	b.d.	b.d.	100.0
51.4	14.1	1.9	12.2	7.2	0.18	11.4	2.7	0.08	b.d.	b.d.	101.0
50.9	13.9	2.0	12.0	7.0	0.20	11.3	2.8	0.09	b.d.	b.d.	100.2
51.3	14.2	2.0	12.1	7.2	0.20	11.3	2.7	0.08	b.d.	b.d.	101.2
51.3	14.1	2.0	12.1	7.2	0.20	11.3	2.8	0.07	b.d.	b.d.	100.9
51.4	14.1	1.9	11.9	7.1	0.20	11.2	2.8	0.09	b.d.	b.d.	100.6
51.2	14.0	2.0	12.0	7.1	0.21	11.4	2.7	0.08	b.d.	b.d.	100.6
51.0	14.1	1.9	11.9	7.1	0.24	11.3	2.7	0.08	b.d.	b.d.	100.3
50.8	13.8	1.9	12.1	7.1	0.23	11.2	2.7	0.08	b.d.	b.d.	100.0
50.9	14.1	1.8	12.1	7.0	0.21	11.2	2.7	0.08	b.d.	b.d.	100.2
51.1	13.9	1.9	12.0	6.8	0.18	11.2	2.9	0.09	b.d.	b.d.	99.9
50.9	14.0	1.9	12.0	7.1	0.21	11.3	2.7	0.09	b.d.	b.d.	100.3
51.1	14.1	1.9	12.0	7.0	0.18	11.3	2.7	0.09	b.d.	b.d.	100.4
51.0	14.0	1.9	11.9	7.1	0.20	11.2	2.7	0.07	b.d.	b.d.	100.1
51.0	13.9	1.9	12.1	7.0	0.19	11.3	2.7	0.08	b.d.	b.d.	100.3
51.1	13.9	2.0	11.9	7.1	0.26	11.4	2.7	0.08	b.d.	b.d.	100.5
<b>Enstatite</b>											
58.4	0.27	b.d.	2.28	38.9	0.00	0.01	0.03	b.d.	0.07	b.d.	100.0
58.6	0.18	0.15	2.66	39.7	0.00	0.09	0.03	b.d.	0.04	b.d.	101.4
57.5	0.21	b.d.	2.47	38.8	0.07	b.d.	0.04	0.03	0.05	b.d.	99.2
58.3	0.15	b.d.	2.23	39.6	0.02	0.05	b.d.	b.d.	0.02	b.d.	100.4
58.2	0.21	b.d.	2.71	39.7	0.04	0.11	0.04	b.d.	b.d.	b.d.	101.1

	SiO <sub>2</sub>	Al <sub>2</sub> O <sub>3</sub>	TiO <sub>2</sub>	FeO	MgO	MnO	CaO	Na <sub>2</sub> O	K <sub>2</sub> O	Cl	In <sub>2</sub> O <sub>3</sub>	Total
<b>Bishop Tuff</b>												
74.6	15.5	0.08	1.06	0.07	0.16	0.49	2.81	4.69	0.01	b.d.	b.d.	99.4
75.7	12.4	0.04	0.62	0.03	b.d.	0.45	2.71	4.81	b.d.	b.d.	b.d.	96.7
76.6	12.2	0.02	0.87	0.02	b.d.	0.32	2.64	4.73	0.04	b.d.	b.d.	97.4
75.5	13.3	0.06	1.00	0.10	b.d.	0.37	2.86	4.89	b.d.	b.d.	b.d.	98.1
72.7	16.2	0.00	0.96	0.05	0.16	0.43	2.71	4.75	0.01	b.d.	b.d.	98.0
74.6	14.6	0.01	1.00	0.06	0.10	0.46	2.80	4.92	0.03	b.d.	b.d.	98.5
72.4	16.4	0.08	0.98	0.05	0.13	0.61	2.83	4.67	0.03	b.d.	b.d.	98.2
76.7	12.7	0.05	0.77	0.01	b.d.	0.39	2.67	4.85	0.03	b.d.	b.d.	98.2
69.1	20.1	0.13	1.02	0.02	b.d.	0.57	2.71	4.55	0.04	b.d.	b.d.	98.3
76.4	13.0	0.06	0.72	0.03	0.03	0.41	2.90	4.85	b.d.	b.d.	b.d.	98.5
71.9	18.0	0.08	1.03	0.10	0.16	0.57	2.91	4.63	b.d.	b.d.	b.d.	99.3
75.1	13.4	b.d.	0.80	0.09	0.10	0.42	2.89	4.66	0.05	b.d.	b.d.	97.5
73.7	15.1	0.09	0.75	0.00	0.06	0.51	2.68	4.69	0.03	b.d.	b.d.	97.6
72.1	16.7	0.02	0.78	0.14	b.d.	0.54	2.72	4.44	0.05	b.d.	b.d.	97.5
74.9	14.4	0.12	0.73	b.d.	b.d.	0.44	2.72	4.52	b.d.	b.d.	b.d.	97.8
75.4	13.4	b.d.	0.75	0.07	0.13	0.29	2.67	4.98	0.01	b.d.	b.d.	97.7
73.0	14.6	0.05	0.77	0.03	0.19	0.49	2.92	4.74	b.d.	b.d.	b.d.	96.8
73.3	14.7	0.17	0.85	0.01	b.d.	0.40	2.82	4.78	0.03	b.d.	b.d.	97.1
73.3	15.5	0.09	0.86	0.09	0.16	0.42	2.72	4.73	0.02	b.d.	b.d.	97.9
73.2	15.0	0.10	0.70	0.02	0.06	0.46	2.89	4.69	0.03	b.d.	b.d.	97.1
<b>Sanidine</b>												
66.2	19.2	0.09	0.12	b.d.	b.d.	0.34	4.06	9.94	b.d.	b.d.	b.d.	100.0
65.9	18.6	b.d.	0.27	b.d.	b.d.	0.30	3.84	10.2	0.01	b.d.	b.d.	99.01
66.6	18.9	b.d.	0.22	b.d.	b.d.	0.27	3.84	10.1	0.01	b.d.	b.d.	99.93
66.2	19.2	b.d.	0.07	0.06	b.d.	0.32	3.83	9.89	0.02	b.d.	b.d.	99.56
65.0	18.8	b.d.	0.10	b.d.	0.22	0.21	3.88	9.82	b.d.	b.d.	b.d.	98.06
66.1	19.0	0.14	0.08	b.d.	b.d.	0.31	3.85	10.2	0.02	b.d.	b.d.	99.74
65.6	19.0	0.06	0.16	0.03	b.d.	0.30	3.57	10.6	b.d.	b.d.	b.d.	99.32
66.4	18.9	b.d.	0.07	b.d.	b.d.	0.22	3.60	10.7	0.02	b.d.	b.d.	99.86
65.3	18.7	b.d.	0.13	b.d.	b.d.	0.17	3.56	11.0	b.d.	b.d.	b.d.	98.82
65.7	18.7	b.d.	0.06	b.d.	0.16	0.31	3.95	10.3	b.d.	b.d.	b.d.	99.09

	SiO <sub>2</sub>	Al <sub>2</sub> O <sub>3</sub>	TiO <sub>2</sub>	FeO	MgO	MnO	CaO	Na <sub>2</sub> O	K <sub>2</sub> O	Cl	In <sub>2</sub> O <sub>3</sub>	Total
<b>Y-14 Biotite</b>												
	39.0	14.0	2.9	15.7	13.3	0.6	b.d.	0.2	9.4	0.02	b.d.	95.1
	38.3	13.8	2.8	16.0	13.3	0.6	b.d.	0.2	8.9	0.04	b.d.	94.0
	39.0	13.9	2.6	15.1	13.4	0.7	b.d.	0.1	9.4	0.02	b.d.	94.3
	38.1	13.6	2.6	15.6	13.7	0.6	b.d.	0.1	9.3	0.02	b.d.	93.6
	37.5	13.6	2.0	17.1	13.1	0.6	b.d.	0.3	7.6	0.03	b.d.	91.8
	39.3	14.4	2.3	16.0	14.0	0.6	b.d.	0.2	9.2	0.03	b.d.	96.0
<b>Magnetite</b>												
	0.10	0.29	0.72	90.26	0.00	0.26	b.d.	0.04	b.d.	b.d.	b.d.	91.7
	0.00	0.38	0.59	89.97	0.02	0.29	b.d.	0.06	b.d.	b.d.	b.d.	91.3
	0.03	0.21	0.47	92.09	0.09	0.00	b.d.	b.d.	b.d.	0.01	b.d.	92.9
	0.09	0.32	0.64	91.61	0.00	0.11	b.d.	b.d.	b.d.	0.02	b.d.	92.8
	0.16	0.31	0.62	90.99	0.00	0.00	b.d.	0.08	0.02	b.d.	b.d.	92.2

## Appendix D: Masses of Experimental Charges

Table D

	Bishop Tuff			Sanidine	Magnetite	Enstatite	CI Solution	InAu Alloy	Basalt	GR1	Y-14 Biotite	Distilled Water
Biotite Run 1	-	-	-	-	-	-	-	53.9	-	16.25	12.8	14.8
Biotite Run 4	29.9	29.9	14.1	18.4	20.9	20.9	20.9	55.0	-	-	-	-
Biotite Run 8	30.0	30.1	14.2	18.8	20.6	20.6	20.6	51.9	-	-	-	-
Biotite Run 11	29.9	30.2	14.3	18.5	20.8	20.8	20.8	49.8	-	-	-	-
Biotite Run 12	30.0	30.1	14.1	18.6	20.8	20.8	20.8	50.8	-	-	-	-
Biotite Run 13	29.9	29.9	14.4	18.0	20.7	20.7	20.7	50.9	-	-	-	-
Biotite Run 15	30.1	29.9	14.5	18.0	21.4	21.4	21.4	50.7	-	-	-	-
Biotite Run 20	30.0	30.1	14.3	18.2	20.9	20.9	20.9	50.4	-	-	-	-
Biotite Run 21	29.9	30.1	14.4	18.2	21.1	21.1	21.1	49.9	-	-	-	-
Biotite Run 23	30.0	30.1	14.3	18.1	21.0	21.0	21.0	50.5	-	-	-	-
Biotite Run 24	29.9	30.0	14.4	18.0	20.9	20.9	20.9	50.0	-	-	-	-
Biotite Run 26	29.9	30.0	14.2	18.4	22.0	22.0	22.0	50.6	-	-	-	-
Biotite Run 27	30.0	20.2	14.3	18.0	21.7	21.7	21.7	50.0	-	-	-	-
Biotite Run 28	29.8	29.9	14.2	18.3	21.8	21.8	21.8	52.8	-	-	-	-
Biotite Run 29 <sup>s</sup>	16.2	-	-	-	21.1	21.1	21.1	24.1	-	-	7.6	-
Biotite Run 31	14.5	14.7	8.0	8.4	10.5	10.5	10.5	28.0	-	-	-	-
Biotite Run 32	15.6	17.7	7.6	8.9	10.6	10.6	10.6	21.0	-	-	-	-
Amphibole Run 4	29.9	-	-	-	21.1	21.1	21.1	50.3	10.6	-	-	-
Amphibole Run 6	29.9	-	-	-	20.9	20.9	20.9	48.0	9.5	-	-	-
Amphibole Run 7	30.5	-	-	-	21.1	21.1	21.1	51.6	10.8	-	-	-
Amphibole Run 8	30.5	-	-	-	20.5	20.5	20.5	49.8	9.3	-	-	-
Amphibole Run 9	30.3	-	-	-	20.5	20.5	20.5	51.9	9.3	-	-	-
Amphibole Run 10	30.0	-	-	-	20.4	20.4	20.4	50.5	9.9	-	-	-
Amphibole Run 11	31.0	-	-	-	20.5	20.5	20.5	50.0	7.7	-	-	-
Amphibole Run 13	30.7	-	-	-	20.9	20.9	20.9	50.9	5.3	-	-	-
Amphibole Run 14	30.2	-	-	-	20.2	20.2	20.2	50.2	5.4	-	-	-

All masses in mg

## Appendix E: EPMA of Run Products

Table E – EPMA of run products (wt%)

Biotite											Total
SiO <sub>2</sub>	Al <sub>2</sub> O <sub>3</sub>	TiO <sub>2</sub>	FeO	MgO	MnO	CaO	Na <sub>2</sub> O	K <sub>2</sub> O	Cl	In <sub>2</sub> O <sub>3</sub>	
<b>Biotite Run 1</b>											
40.6	14.4	2.9	17.1	14.3	0.60	b.d.	0.22	9.3	0.02	b.d.	99.4
40.9	14.5	2.9	16.7	13.9	0.49	b.d.	0.23	9.4	0.01	b.d.	99.1
40.9	14.5	2.8	17.1	14.6	0.50	b.d.	0.26	9.3	0.04	b.d.	100.0
40.0	13.9	2.4	16.2	14.6	0.35	b.d.	0.24	9.5	0.02	b.d.	97.4
39.1	13.9	2.2	16.4	14.4	0.62	b.d.	0.26	9.5	0.03	b.d.	96.5
39.8	14.7	2.8	16.7	13.7	0.48	b.d.	0.19	9.4	0.02	b.d.	97.9
41.3	14.7	2.8	16.7	14.6	0.44	b.d.	0.23	9.3	b.d.	0.01	100.0
40.3	14.7	2.7	16.7	14.2	0.76	b.d.	0.24	9.4	0.01	b.d.	98.9
40.2	14.4	2.9	16.6	14.4	0.48	b.d.	0.32	9.3	0.02	b.d.	98.6
38.9	13.9	2.7	16.4	14.1	0.52	b.d.	0.25	9.4	0.03	b.d.	96.2
<b>Biotite Run 4</b>											
27.0	10.4	n.a.	6.2	13.0	b.d.	b.d.	0.35	5.4	0.13	0.2	62.8
27.8	10.4	n.a.	6.7	13.7	b.d.	b.d.	0.43	6.1	0.13	0.2	65.5
25.1	9.8	n.a.	6.3	11.7	b.d.	b.d.	0.39	5.4	0.10	0.2	59.0
24.9	9.4	n.a.	6.5	11.9	b.d.	b.d.	0.38	5.6	0.11	0.2	59.1
25.7	9.7	n.a.	6.8	12.4	b.d.	b.d.	0.39	5.7	0.16	0.2	61.1
25.1	9.3	n.a.	6.5	12.0	b.d.	b.d.	0.34	5.7	0.13	0.3	59.4
<b>Biotite Run 8</b>											
37.0	14.2	2.5	14.1	14.4	0.44	b.d.	0.22	9.7	0.05	0.04	92.6
36.1	13.9	2.8	15.0	13.8	0.51	b.d.	0.18	9.6	0.04	0.04	92.1
37.6	14.3	2.8	15.2	13.6	0.49	b.d.	0.14	9.6	0.06	0.1	93.9
37.5	14.3	2.9	15.0	13.3	0.53	b.d.	0.17	9.6	0.07	0.1	93.4
38.1	14.4	2.8	15.1	14.0	0.45	b.d.	0.20	9.8	0.07	0.04	94.9
38.6	14.7	2.4	13.8	14.8	0.39	b.d.	0.22	9.6	0.05	0.1	94.5
38.0	14.5	2.2	14.3	14.8	0.42	b.d.	0.25	9.6	0.05	0.1	94.3
36.8	14.2	2.6	14.7	13.8	0.44	b.d.	0.20	9.7	0.03	0.03	92.4
37.8	14.3	2.8	14.7	13.9	0.45	b.d.	0.17	9.7	0.01	0.05	93.9
37.4	14.2	2.7	14.9	14.2	0.47	b.d.	0.19	9.7	0.05	0.03	93.7

	SiO <sub>2</sub>	Al <sub>2</sub> O <sub>3</sub>	TiO <sub>2</sub>	FeO	MgO	MnO	CaO	Na <sub>2</sub> O	K <sub>2</sub> O	Cl	In <sub>2</sub> O <sub>3</sub>	Total
<b>Biotite Run 11</b>												
	39.6	14.8	1.8	13.3	11.3	0.45	b.d.	0.16	9.5	0.09	0.1	91.1
	39.5	14.9	1.7	13.5	14.0	0.39	b.d.	0.19	9.6	0.12	0.1	94.1
	38.5	14.3	2.0	14.6	14.5	0.52	b.d.	0.19	9.4	0.11	0.3	94.3
	37.7	14.3	1.7	14.0	15.1	0.43	b.d.	0.35	9.1	0.46	0.4	93.4
	39.4	14.5	1.5	12.5	16.9	0.32	b.d.	0.46	8.7	0.38	0.5	95.2
<b>Biotite Run 12</b>												
	36.1	11.4	0.9	8.9	17.9	0.19	b.d.	0.40	8.4	0.12	0.2	84.6
	33.6	10.6	1.1	8.9	18.2	0.16	b.d.	0.50	8.2	0.17	0.3	81.7
	35.2	10.8	0.7	7.6	18.7	b.d.	b.d.	0.37	8.4	0.12	0.2	82.2
<b>Biotite Run 13</b>												
	34.6	12.8	2.5	17.0	13.3	0.57	b.d.	0.07	9.4	0.02	b.d.	90.3
	35.3	13.0	2.7	17.3	13.3	0.60	b.d.	0.12	9.6	0.03	b.d.	92.0
<b>Biotite Run 15.1</b>												
	38.4	14.4	3.1	13.2	16.3	0.17	b.d.	0.42	8.6	0.24	0.7	95.6
	39.5	13.9	2.3	11.0	17.9	0.15	b.d.	0.45	8.6	0.42	0.8	95.1
	38.4	14.8	2.7	11.7	17.1	0.10	b.d.	0.42	8.9	0.20	0.5	94.9
<b>Biotite Run 15.2</b>												
	43.6	12.9	0.6	8.0	22.3	b.d.	b.d.	0.42	8.2	0.12	0.2	96.4
	43.1	12.7	0.8	8.1	21.7	0.13	b.d.	0.41	8.2	0.14	0.2	95.5
	43.6	12.7	0.4	7.7	21.3	b.d.	b.d.	0.44	7.9	0.16	0.4	94.7
	43.7	13.1	0.8	8.2	21.3	b.d.	b.d.	0.36	8.3	0.10	0.2	96.2
<b>Biotite Run 20</b>												
	41.3	12.5	0.3	7.4	21.7	b.d.	b.d.	0.46	7.3	0.10	0.7	91.8
	41.1	12.4	0.3	7.5	22.4	b.d.	b.d.	0.49	7.3	0.13	0.7	92.4
<b>Biotite Run 21</b>												
	36.3	13.7	2.5	15.0	13.1	0.49	b.d.	0.10	9.0	0.02	b.d.	90.2
	37.0	14.5	2.9	15.9	13.1	0.58	b.d.	0.08	9.2	0.03	b.d.	93.3
	38.0	14.2	2.9	16.1	13.6	0.58	b.d.	0.07	9.3	0.02	b.d.	94.8
	36.7	13.7	2.5	16.1	14.4	0.48	b.d.	0.31	9.1	0.04	b.d.	93.2
<b>Biotite Run 23.1</b>												
	38.8	13.9	2.5	15.0	14.1	0.45	b.d.	0.19	8.8	0.06	0.10	93.9
	38.6	13.9	2.6	14.0	14.0	0.47	b.d.	0.25	8.6	0.06	0.29	92.7

	SiO <sub>2</sub>	Al <sub>2</sub> O <sub>3</sub>	TiO <sub>2</sub>	FeO	MgO	MnO	CaO	Na <sub>2</sub> O	K <sub>2</sub> O	Cl	In <sub>2</sub> O <sub>3</sub>	Total
<b>Biotite Run 23.2</b>												
	40.2	13.1	0.9	9.7	19.5	0.20	b.d.	0.42	8.0	0.13	0.26	92.3
	40.6	13.7	1.6	12.0	17.7	0.32	b.d.	0.38	8.3	0.09	0.17	94.9
	40.6	13.5	1.8	12.4	16.9	0.32	b.d.	0.35	8.5	0.09	0.13	94.6
<b>Biotite Run 23.3</b>												
	39.1	14.3	2.4	14.9	13.6	0.46	b.d.	0.23	8.8	0.04	0.02	93.9
	39.5	14.2	2.3	15.1	13.4	0.29	b.d.	0.26	8.8	0.07	0.03	93.9
	39.4	14.4	2.4	15.4	13.7	0.31	b.d.	0.24	8.8	0.04	0.03	94.7
<b>Biotite Run 24</b>												
	36.4	13.4	2.5	14.1	15.1	0.45	b.d.	0.23	9.1	0.04	0.2	91.5
	37.2	13.0	2.2	13.5	16.1	0.38	b.d.	0.30	8.7	0.07	0.05	91.4
	39.0	12.6	1.4	10.9	18.0	0.26	b.d.	0.41	8.4	0.10	0.1	91.1
	37.6	13.0	1.8	12.9	16.6	0.31	b.d.	0.39	8.6	0.15	0.1	91.6
<b>Biotite Run 26</b>												
	41.8	12.7	0.2	7.7	20.1	b.d.	b.d.	0.48	8.3	0.25	0.7	91.8
	42.8	12.9	0.1	7.9	21.6	b.d.	b.d.	0.45	8.4	0.14	0.5	94.3
	41.9	12.6	b.d.	8.0	22.2	b.d.	b.d.	0.45	8.4	0.13	0.4	93.7
	42.4	12.8	0.1	7.8	21.5	b.d.	b.d.	0.41	8.4	0.15	0.4	93.5
<b>Biotite Run 27</b>												
	39.9	11.8	0.2	6.7	22.5	b.d.	b.d.	0.47	8.3	0.10	0.3	90.0
	40.4	11.5	0.2	6.5	23.1	b.d.	b.d.	0.58	8.4	0.10	0.3	90.7
	39.6	11.3	0.2	6.5	22.6	b.d.	b.d.	0.55	8.2	0.13	0.3	89.1
	40.2	11.7	0.2	6.5	22.8	b.d.	b.d.	0.49	8.4	0.11	0.4	90.4
	38.6	11.1	0.3	7.0	23.6	b.d.	b.d.	0.53	8.6	0.11	0.5	89.8
	39.8	11.4	0.3	6.5	21.4	b.d.	b.d.	0.46	8.4	0.12	0.5	88.3

	SiO <sub>2</sub>	Al <sub>2</sub> O <sub>3</sub>	TiO <sub>2</sub>	FeO	MgO	MnO	CaO	Na <sub>2</sub> O	K <sub>2</sub> O	Cl	In <sub>2</sub> O <sub>3</sub>	Total
<b>Biotite Run 28</b>												
	39.5	11.8	0.5	6.8	22.4	b.d.	b.d.	0.48	8.7	0.11	0.34	90.2
	39.3	11.6	0.6	6.9	21.4	b.d.	b.d.	0.43	8.7	0.12	0.34	89.0
	39.6	11.6	0.7	7.1	22.1	b.d.	b.d.	0.45	8.7	0.14	0.31	90.3
	39.4	11.6	0.6	7.0	21.8	0.06	b.d.	0.44	8.8	0.13	0.37	89.8
	42.3	12.4	0.3	6.7	22.6	b.d.	b.d.	0.50	8.6	0.13	0.32	93.5
	43.0	13.0	0.4	7.2	23.0	0.11	b.d.	0.54	8.8	0.12	0.35	96.3
	42.3	12.6	0.4	7.0	23.0	0.06	b.d.	0.51	8.7	0.14	0.37	94.8
	42.3	12.8	0.4	6.8	22.9	b.d.	b.d.	0.49	8.7	0.14	0.36	94.4
	41.3	12.2	0.7	7.4	22.1	b.d.	b.d.	0.47	8.5	0.16	0.46	92.8
	41.4	12.0	0.5	6.5	21.0	b.d.	b.d.	0.43	8.5	0.13	0.69	90.5
	42.1	11.8	0.4	6.9	22.8	b.d.	b.d.	0.49	8.7	0.11	0.31	93.2
<b>Biotite Run 29</b>												
	40.1	13.9	2.7	15.3	12.8	0.57	b.d.	0.16	9.4	0.01	b.d.	94.9
	39.2	14.0	2.8	15.8	13.1	0.56	b.d.	0.18	9.5	0.01	b.d.	95.1
	39.9	14.0	2.8	15.4	13.1	0.59	b.d.	0.19	9.5	0.01	b.d.	95.5
	39.4	14.1	2.7	14.9	12.6	0.59	b.d.	0.11	9.4	b.d.	b.d.	93.8
	39.7	14.1	2.7	14.4	12.3	0.49	b.d.	0.18	9.6	0.02	b.d.	93.5
	40.2	14.1	3.1	15.4	12.1	0.59	b.d.	0.17	9.4	0.01	b.d.	95.1
	37.6	13.9	2.9	15.8	13.1	0.51	b.d.	0.18	9.3	0.04	0.01	93.3
	38.2	13.1	2.9	15.7	13.5	0.55	b.d.	0.17	9.3	0.03	b.d.	93.4
	38.6	13.3	2.8	16.0	13.3	0.49	b.d.	0.19	9.4	0.02	0.01	94.0
<b>Biotite Run 31</b>												
	38.5	13.8	3.0	14.3	15.5	0.39	b.d.	0.30	9.5	0.04	0.04	95.2
	36.8	13.8	3.1	16.0	14.5	0.40	b.d.	0.19	9.8	0.02	0.03	94.6
	37.0	13.9	3.1	14.6	14.8	0.42	b.d.	0.22	9.6	0.04	0.23	93.6
	36.9	13.8	3.0	16.0	14.2	0.41	b.d.	0.16	9.8	0.02	0.02	94.3
	37.3	13.9	3.0	16.5	13.9	0.45	b.d.	0.16	9.7	0.03	b.d.	95.0
	38.0	13.9	3.1	15.6	13.9	0.41	b.d.	0.19	9.5	0.05	0.04	94.6
	38.0	14.1	3.0	16.3	14.6	0.43	b.d.	0.20	9.6	0.02	b.d.	96.2
	38.4	13.9	3.0	15.9	14.3	0.40	b.d.	0.34	9.3	0.05	0.05	95.6
	37.6	14.2	3.1	15.9	14.3	0.43	b.d.	0.19	9.5	0.06	0.13	95.1

<b>SiO<sub>2</sub></b>	<b>Al<sub>2</sub>O<sub>3</sub></b>	<b>TiO<sub>2</sub></b>	<b>FeO</b>	<b>MgO</b>	<b>MnO</b>	<b>CaO</b>	<b>Na<sub>2</sub>O</b>	<b>K<sub>2</sub>O</b>	<b>Cl</b>	<b>In<sub>2</sub>O<sub>3</sub></b>	<b>Total</b>
<b>Biotite Run 32</b>											
39.7	15.3	0.7	13.1	17.8	b.d.	b.d.	0.5	8.8	0.3	0.06	96.2
39.7	15.4	0.7	13.1	17.8	b.d.	b.d.	0.5	8.8	0.3	0.05	96.3
39.7	15.3	0.6	12.7	18.3	b.d.	b.d.	0.5	8.8	0.3	0.04	96.2
39.2	14.9	0.6	12.4	17.9	b.d.	b.d.	0.4	8.8	0.3	0.06	94.6
39.8	14.7	0.5	11.6	19.0	0.07	b.d.	0.5	8.8	0.2	0.07	95.1
39.7	14.7	0.6	12.5	18.7	b.d.	b.d.	0.5	8.7	0.3	0.09	95.5
41.8	16.0	0.4	11.5	19.9	b.d.	b.d.	0.5	8.8	0.2	0.10	99.0
40.7	15.3	0.4	11.5	19.2	b.d.	b.d.	0.5	8.6	0.2	0.12	96.4
39.4	15.3	0.6	12.0	18.7	b.d.	b.d.	0.5	8.7	0.3	0.11	95.4
37.1	14.2	0.5	11.3	18.5	b.d.	b.d.	0.5	8.7	0.3	0.09	91.1

## Glass

	SiO <sub>2</sub>	Al <sub>2</sub> O <sub>3</sub>	TiO <sub>2</sub>	FeO	MgO	MnO	CaO	Na <sub>2</sub> O	K <sub>2</sub> O	Cl	In <sub>2</sub> O <sub>3</sub>	Total
<b>Biotite Run 1</b>												
74.0	11.9	n.a.	0.09	0.02	0.03	b.d.	3.5	4.6	b.d.	0.04	94.3	
75.9	11.0	n.a.	0.09	0.02	b.d.	0.02	3.2	4.3	b.d.	0.05	94.6	
68.3	18.0	n.a.	0.07	b.d.	b.d.	b.d.	4.5	8.0	b.d.	0.05	98.9	
73.9	11.5	n.a.	b.d.	0.03	0.02	b.d.	3.5	4.6	0.01	0.05	93.6	
74.2	11.6	n.a.	b.d.	b.d.	0.07	b.d.	3.5	4.5	b.d.	0.04	93.9	
74.1	11.5	n.a.	b.d.	0.03	0.04	b.d.	3.4	4.4	b.d.	0.04	93.5	
74.4	11.4	n.a.	0.07	b.d.	b.d.	b.d.	3.5	4.5	b.d.	0.04	93.9	
75.9	10.7	n.a.	b.d.	b.d.	b.d.	b.d.	3.2	4.3	0.01	0.05	94.2	
74.9	11.6	n.a.	b.d.	b.d.	b.d.	b.d.	3.5	4.4	b.d.	0.05	94.5	
76.7	10.5	n.a.	b.d.	b.d.	b.d.	b.d.	3.2	4.2	0.01	0.07	94.7	
75.5	10.7	n.a.	0.09	0.02	b.d.	b.d.	3.2	4.2	0.01	0.06	93.8	
75.3	11.0	n.a.	b.d.	b.d.	b.d.	b.d.	3.2	4.3	b.d.	0.06	93.9	
75.5	10.9	n.a.	0.08	b.d.	b.d.	b.d.	3.2	4.3	b.d.	0.05	94.0	
75.0	12.1	n.a.	0.09	b.d.	0.05	b.d.	3.7	4.6	b.d.	0.06	95.6	
74.4	11.5	n.a.	b.d.	0.03	b.d.	b.d.	3.4	4.4	0.01	0.06	94.0	
76.4	10.7	n.a.	b.d.	b.d.	0.03	b.d.	3.2	4.2	b.d.	0.07	94.6	
75.6	10.8	n.a.	b.d.	b.d.	0.03	b.d.	3.3	4.4	0.02	0.07	94.1	
74.8	11.1	n.a.	b.d.	b.d.	0.03	b.d.	3.3	4.4	0.02	0.06	93.7	
75.1	10.8	n.a.	0.12	b.d.	b.d.	b.d.	3.2	4.3	b.d.	0.07	93.6	
74.7	11.8	n.a.	b.d.	b.d.	0.01	b.d.	3.5	4.7	b.d.	0.04	94.8	
73.9	11.1	n.a.	b.d.	b.d.	b.d.	b.d.	3.2	4.3	b.d.	0.04	92.6	
72.8	12.2	n.a.	b.d.	b.d.	b.d.	b.d.	3.5	4.7	b.d.	0.04	93.3	
73.6	13.3	n.a.	0.11	b.d.	0.06	b.d.	4.0	5.2	b.d.	0.04	96.2	
72.0	12.8	n.a.	0.07	0.02	b.d.	b.d.	3.8	4.8	0.02	0.04	93.6	
73.4	12.3	n.a.	b.d.	0.03	b.d.	b.d.	3.7	4.7	b.d.	0.04	94.2	
73.9	12.1	n.a.	b.d.	b.d.	b.d.	b.d.	3.6	4.5	b.d.	0.04	94.2	
73.7	11.5	n.a.	b.d.	b.d.	0.02	b.d.	3.5	4.3	b.d.	0.04	93.2	
75.7	10.9	n.a.	b.d.	b.d.	b.d.	b.d.	3.3	4.3	0.02	0.05	94.2	
69.6	16.1	n.a.	b.d.	0.03	0.02	b.d.	4.4	7.3	b.d.	0.04	97.5	
74.9	11.4	n.a.	b.d.	0.02	b.d.	b.d.	3.3	4.5	b.d.	0.04	94.2	
73.9	11.4	n.a.	b.d.	b.d.	b.d.	0.03	3.4	4.2	0.02	0.03	93.1	
74.6	12.5	n.a.	b.d.	0.02	b.d.	0.02	3.9	4.7	0.01	0.04	95.8	
73.5	11.6	n.a.	b.d.	b.d.	0.05	b.d.	3.4	4.5	b.d.	0.04	93.1	
74.7	11.6	n.a.	b.d.	b.d.	0.02	b.d.	3.5	4.5	b.d.	0.03	94.3	
74.6	11.6	n.a.	0.05	b.d.	0.05	b.d.	3.5	4.4	0.01	0.03	94.4	
74.6	11.6	n.a.	0.08	b.d.	0.05	b.d.	3.4	4.5	b.d.	0.05	94.3	
74.9	11.6	n.a.	0.05	b.d.	0.03	0.03	3.5	4.4	0.01	0.03	94.6	
73.5	10.8	n.a.	b.d.	b.d.	b.d.	0.02	3.1	4.2	0.01	0.04	91.7	
74.4	11.4	n.a.	b.d.	b.d.	b.d.	b.d.	3.5	4.4	0.01	0.03	93.7	

<b>SiO<sub>2</sub></b>	<b>Al<sub>2</sub>O<sub>3</sub></b>	<b>TiO<sub>2</sub></b>	<b>FeO</b>	<b>MgO</b>	<b>MnO</b>	<b>CaO</b>	<b>Na<sub>2</sub>O</b>	<b>K<sub>2</sub>O</b>	<b>Cl</b>	<b>In<sub>2</sub>O<sub>3</sub></b>	<b>Total</b>
<b>Biotite Run 4</b>											
71.0	14.0	n.a.	0.49	0.06	b.d.	0.4	3.3	5.6	0.22	0.07	95.3
70.5	13.7	n.a.	0.59	0.13	b.d.	0.4	3.1	5.5	0.21	0.05	94.3
69.1	13.6	n.a.	0.58	0.20	b.d.	0.4	3.2	5.6	0.22	0.08	93.0
71.1	14.2	n.a.	0.56	0.10	0.1	0.5	3.3	5.6	0.22	0.06	95.7
71.2	13.9	n.a.	0.71	0.11	b.d.	0.4	3.3	5.6	0.25	0.08	95.6
71.2	14.1	n.a.	0.80	0.04	0.1	0.4	2.5	5.6	0.25	0.08	95.1
71.3	13.3	n.a.	0.74	0.11	0.1	0.4	3.3	5.6	0.18	0.05	95.2
71.2	13.8	n.a.	0.68	0.10	b.d.	0.4	3.3	5.6	0.25	0.07	95.4
70.6	13.7	n.a.	0.67	0.08	0.1	0.4	3.3	5.7	0.18	0.04	94.8
71.1	13.7	n.a.	0.68	0.08	0.1	0.4	3.4	5.7	0.23	0.05	95.4
70.2	13.6	n.a.	0.57	0.15	0.1	0.4	3.2	5.7	0.22	0.08	94.2
<b>Biotite Run 8</b>											
69.2	12.6	b.d.	0.71	0.16	b.d.	0.4	3.1	5.9	0.24	0.10	92.3
68.6	13.3	b.d.	0.75	0.04	0.01	0.4	3.2	5.8	0.27	0.08	92.6
68.4	14.0	b.d.	0.42	b.d.	0.09	0.4	3.4	6.0	0.27	0.08	93.1
<b>Biotite Run 11</b>											
69.2	14.6	0.1	0.36	0.12	0.1	0.7	3.5	5.9	0.13	0.05	94.7
70.4	12.9	0.04	0.68	0.09	b.d.	0.3	3.0	5.3	0.10	0.06	93.0
69.3	13.2	b.d.	0.63	0.11	b.d.	0.4	3.1	5.3	0.17	0.07	92.3
68.0	13.3	0.1	0.36	0.10	b.d.	0.6	3.3	5.7	0.16	0.06	91.7
67.9	13.3	0.2	0.35	0.11	b.d.	0.7	3.2	5.8	0.21	0.05	91.8
<b>Biotite Run 12</b>											
68.9	13.3	0.1	0.25	0.05	b.d.	0.7	3.5	5.1	0.13	0.05	92.0
71.1	12.7	b.d.	0.48	0.10	b.d.	0.3	3.2	5.3	0.18	0.05	93.4
69.6	14.1	0.1	0.50	0.14	0.1	0.7	3.5	5.7	0.15	0.05	94.6
71.0	12.2	0.1	0.41	0.14	b.d.	0.4	3.1	5.3	0.19	0.04	92.8
70.1	14.3	0.1	0.39	0.12	0.1	0.7	3.6	5.6	0.17	0.04	95.2
68.3	13.9	b.d.	0.52	0.06	b.d.	0.6	3.4	5.7	0.15	0.04	92.7
70.2	12.3	b.d.	0.35	0.13	b.d.	0.5	3.2	4.9	0.15	0.05	91.8
<b>Biotite Run 13</b>											
71.7	12.3	0.1	0.45	0.07	0.2	0.4	3.5	4.7	0.22	0.06	93.7
70.3	13.5	b.d.	0.40	0.11	b.d.	0.6	3.5	5.1	0.14	0.05	93.8
69.7	13.8	b.d.	0.40	0.18	0.1	0.6	3.4	5.7	0.13	0.05	94.2
70.2	13.1	b.d.	0.30	0.18	0.02	0.6	3.2	5.5	0.14	0.05	93.3

SiO <sub>2</sub>	Al <sub>2</sub> O <sub>3</sub>	TiO <sub>2</sub>	FeO	MgO	MnO	CaO	Na <sub>2</sub> O	K <sub>2</sub> O	Cl	In <sub>2</sub> O <sub>3</sub>	Total
<b>Biotite Run 15</b>											
71.0	13.0	b.d.	0.22	0.10	b.d.	0.5	3.2	5.1	0.12	0.04	93.3
69.1	13.9	0.1	0.64	0.03	0.1	0.6	3.5	5.5	0.10	0.04	93.6
69.1	14.6	0.1	0.69	0.06	b.d.	0.6	3.6	5.6	0.12	0.04	94.5
69.0	14.7	b.d.	0.08	0.04	0.12	0.73	3.7	5.6	0.09	0.03	94.1
<b>Biotite Run 20</b>											
72.0	13.6	b.d.	0.27	0.08	0.03	0.5	3.7	5.2	0.18	0.06	95.6
70.8	12.1	b.d.	0.47	0.05	0.1	0.5	3.3	4.8	0.20	0.07	92.2
70.1	12.4	0.1	0.42	b.d.	0.2	0.6	3.5	4.7	0.19	0.05	92.1
71.3	12.3	0.1	0.67	0.08	b.d.	0.5	3.4	4.7	0.20	0.05	93.4
70.5	13.8	0.1	0.23	0.06	0.1	0.5	3.7	5.6	0.16	0.06	94.7
<b>Biotite Run 21</b>											
70.1	13.9	0.1	0.39	0.04	b.d.	0.7	3.8	5.3	0.16	0.05	94.4
69.6	13.9	b.d.	0.38	0.08	b.d.	0.7	3.8	5.3	0.15	0.04	94.0
72.6	13.3	b.d.	0.48	0.08	b.d.	0.6	3.2	5.5	0.17	0.05	95.8
72.3	12.5	b.d.	0.46	0.07	0.02	0.6	3.2	5.1	0.19	0.05	94.4
70.1	13.2	b.d.	0.50	0.17	b.d.	0.7	3.6	5.3	0.17	0.05	93.8
<b>Biotite Run 23</b>											
71.7	12.8	0.1	0.46	0.07	0.03	0.5	3.2	5.1	0.18	0.05	94.1
71.0	13.2	0.1	0.48	0.11	0.01	0.6	3.4	5.0	0.16	0.04	94.0
72.5	11.8	0.1	0.52	0.10	b.d.	0.4	3.2	4.6	0.21	0.06	93.4
69.3	10.7	b.d.	0.39	0.06	0.04	0.5	3.2	4.1	0.15	n.a.	88.4
69.5	13.2	b.d.	0.48	0.09	0.01	0.6	3.5	5.3	0.16	0.05	92.8
71.3	13.7	b.d.	0.74	0.08	b.d.	0.6	3.6	5.1	0.17	0.04	95.3
71.2	12.5	0.1	0.46	0.07	0.01	0.4	3.3	5.0	0.19	0.05	93.1
70.5	13.2	b.d.	0.50	0.10	0.02	0.5	3.5	5.2	0.16	0.04	93.6
<b>Biotite Run 24</b>											
72.3	11.2	0.04	0.63	0.08	0.1	0.4	2.9	4.5	0.21	0.06	92.3
69.2	13.9	0.1	0.54	0.08	b.d.	0.7	3.7	5.2	0.16	0.05	93.4
70.6	12.5	0.1	0.57	0.07	0.02	0.5	3.2	4.7	0.21	0.05	92.5
69.4	13.7	0.05	0.50	0.08	b.d.	0.6	3.6	5.4	0.15	0.03	93.5
70.5	11.8	0.1	0.54	0.11	b.d.	0.4	2.9	4.6	0.21	0.05	91.0
71.2	11.4	b.d.	0.54	0.07	0.03	0.4	3.0	4.6	0.22	0.05	91.5

<b>SiO<sub>2</sub></b>	<b>Al<sub>2</sub>O<sub>3</sub></b>	<b>TiO<sub>2</sub></b>	<b>FeO</b>	<b>MgO</b>	<b>MnO</b>	<b>CaO</b>	<b>Na<sub>2</sub>O</b>	<b>K<sub>2</sub>O</b>	<b>Cl</b>	<b>In<sub>2</sub>O<sub>3</sub></b>	<b>Total</b>
<b>Biotite Run 26</b>											
70.1	13.3	0.05	0.45	0.05	0.01	0.4	3.7	5.7	0.16	0.03	93.9
68.3	14.2	b.d.	0.41	0.04	b.d.	0.7	4.2	6.0	0.15	0.02	94.0
69.5	13.6	0.04	0.43	0.06	b.d.	0.6	3.9	5.6	0.17	0.02	94.0
71.1	11.6	0.1	0.48	0.08	b.d.	0.4	3.6	4.7	0.18	0.03	92.3
69.3	12.8	0.1	0.41	0.09	0.01	0.5	3.7	5.5	0.17	0.03	92.6
69.2	13.4	0.1	0.35	0.06	b.d.	0.5	3.9	5.7	0.15	0.02	93.5
70.3	12.3	b.d.	0.43	0.07	b.d.	0.5	3.7	5.1	0.18	0.05	92.6
<b>Biotite Run 27</b>											
74.7	14.7	0.1	0.49	0.06	b.d.	0.7	3.8	5.4	0.16	0.06	100.1
74.2	12.9	0.1	0.93	0.12	0.04	0.4	3.2	5.0	0.21	0.05	97.0
73.8	14.0	0.04	0.56	0.03	b.d.	0.7	3.5	5.1	0.17	0.08	98.0
71.7	15.5	0.1	0.83	0.06	b.d.	1.0	4.1	5.0	0.12	0.04	98.4
74.1	13.1	b.d.	0.52	0.07	b.d.	0.6	3.4	4.9	0.20	0.06	96.9
72.6	14.2	0.1	0.63	0.08	0.04	0.8	3.9	4.9	0.17	0.06	97.3
72.3	15.4	b.d.	0.49	0.07	0.01	0.9	4.2	5.4	0.13	0.06	98.8
74.3	12.8	0.1	0.47	0.10	b.d.	0.5	3.1	4.9	0.19	0.05	96.4
<b>Biotite Run 28</b>											
74.7	12.0	0.1	0.56	0.06	0.1	0.4	3.0	5.0	0.19	0.06	95.9
74.4	11.9	b.d.	0.65	0.11	b.d.	0.4	2.9	5.1	0.20	0.07	95.6
73.6	11.5	b.d.	0.43	0.09	0.1	0.4	3.0	5.0	0.26	0.06	94.3
74.3	11.5	b.d.	0.55	0.13	b.d.	0.4	2.8	5.2	0.21	0.07	95.0
73.7	11.8	b.d.	0.66	0.21	0.1	0.4	2.9	5.1	0.24	0.07	95.0
74.3	11.9	b.d.	0.59	0.09	0.04	0.4	3.1	5.0	0.21	0.07	95.5
72.6	13.3	0.1	0.53	0.07	b.d.	0.5	3.3	5.4	0.19	0.05	96.0
71.2	12.8	b.d.	0.51	0.09	b.d.	0.5	3.2	5.2	0.22	0.06	93.7
74.0	12.8	b.d.	0.50	0.08	b.d.	0.5	3.2	5.2	0.21	0.07	96.5
73.0	11.8	b.d.	0.56	0.10	0.04	0.4	3.0	5.0	0.21	0.07	94.2
<b>Biotite Run 29</b>											
67.8	14.0	0.04	0.31	0.07	0.0	0.6	3.3	5.8	0.13	0.04	92.1
67.4	13.4	0.1	0.31	0.03	0.0	0.5	3.3	5.9	0.15	0.05	91.0
68.2	12.9	0.04	0.45	0.07	0.1	0.5	3.2	5.3	0.17	0.05	90.9

<b>SiO<sub>2</sub></b>	<b>Al<sub>2</sub>O<sub>3</sub></b>	<b>TiO<sub>2</sub></b>	<b>FeO</b>	<b>MgO</b>	<b>MnO</b>	<b>CaO</b>	<b>Na<sub>2</sub>O</b>	<b>K<sub>2</sub>O</b>	<b>Cl</b>	<b>In<sub>2</sub>O<sub>3</sub></b>	<b>Total</b>
<b>Biotite Run 31</b>											
70.0	13.0	0.1	0.41	0.09	0.0	0.5	2.9	5.6	0.16	0.04	92.7
71.6	15.0	0.1	0.67	0.04	0.0	0.7	3.8	6.2	0.14	0.01	98.2
72.3	13.9	0.1	0.78	0.08	0.05	0.5	3.5	5.9	0.17	0.03	97.2
73.5	12.4	0.1	0.51	0.08	0.0	0.5	3.3	5.2	0.20	0.04	95.7
73.1	13.8	0.1	0.48	0.07	0.0	0.6	3.5	5.6	0.18	0.02	97.4
72.5	14.1	0.1	0.40	0.08	0.0	0.5	3.5	6.1	0.17	0.03	97.5
<b>Biotite Run 32</b>											
74.8	14.4	0.1	0.45	0.06	0.0	0.8	4.1	5.1	0.16	0.02	100.0
73.8	12.2	0.0	0.61	0.11	0.0	0.4	3.2	4.8	0.20	0.02	95.2
71.1	13.6	0.1	0.42	0.11	0.0	0.4	3.3	5.9	0.16	0.02	95.1
74.7	12.5	0.1	0.58	0.13	0.0	0.4	3.2	4.9	0.22	0.01	96.7
70.7	14.1	0.1	0.35	0.12	0.00	0.6	3.7	5.8	0.16	0.01	95.5
74.6	13.1	0.1	0.42	0.13	0.0	0.4	3.2	5.1	0.19	0.02	97.2
74.7	12.4	0.1	0.5	0.1	0.0	0.3	3.1	4.7	0.2	0.0	96.1

## Amphibole

	SiO <sub>2</sub>	Al <sub>2</sub> O <sub>3</sub>	TiO <sub>2</sub>	FeO	MgO	MnO	CaO	Na <sub>2</sub> O	K <sub>2</sub> O	Cl	In <sub>2</sub> O <sub>3</sub>	Total
<b>Amphibole Run 4</b>												
	47.8	9.8	1.2	8.9	9.0	0.2	8.3	1.1	1.4	0.3	2.1	90.0
	45.8	9.2	1.4	10.8	10.4	0.2	9.6	1.4	1.2	0.2	2.9	93.0
	40.3	9.1	1.2	10.1	12.4	0.3	11.0	1.5	1.1	0.3	2.3	89.6
	49.6	10.3	0.9	8.3	8.5	0.1	7.7	1.7	2.2	0.2	n/a	89.6
<b>Amphibole Run 6.1</b>												
	44.2	5.3	0.6	12.3	14.3	0.6	10.8	1.0	0.5	0.01	0.02	89.7
	45.1	5.2	0.6	12.1	13.6	0.7	10.4	1.0	0.4	0.02	0.01	89.1
	47.4	5.5	0.6	12.1	13.1	0.5	10.6	0.9	0.4	0.03	0.01	91.0
	47.4	5.4	0.7	12.1	13.7	0.6	10.9	0.9	0.4	0.01	0.01	92.2
<b>Amphibole Run 6.2</b>												
	42.9	8.6	1.2	10.7	11.9	0.2	10.1	1.3	0.8	0.2	3.3	87.9
	43.8	9.0	1.5	10.1	14.2	0.4	11.9	1.6	1.1	0.2	3.3	93.7
	40.5	7.9	1.2	8.9	13.9	0.2	12.9	1.5	1.0	0.3	2.0	88.2
	43.7	8.9	1.4	9.8	14.0	0.3	12.1	1.5	1.1	0.3	3.3	93.2
	43.2	8.3	1.2	12.0	12.3	0.3	11.7	1.3	0.8	0.2	3.3	91.1
	42.1	8.5	1.3	10.3	13.5	0.3	11.4	1.4	1.1	0.2	3.3	90.2
	42.4	8.4	1.3	13.4	12.8	0.3	11.3	1.4	0.8	0.2	3.6	92.3
	42.9	8.2	1.2	13.6	9.8	0.3	10.7	1.0	0.8	0.3	3.3	88.8
<b>Amphibole Run 7</b>												
	41.7	8.7	1.3	8.7	14.2	0.3	11.4	1.6	1.1	0.2	3.1	89.1
	42.3	9.3	1.2	9.2	14.5	0.3	11.3	1.6	1.1	0.2	3.0	91.0
	41.0	8.9	1.1	8.8	14.1	0.3	10.8	1.6	1.1	0.6	3.0	88.1
	41.8	9.1	1.1	8.8	14.3	0.2	11.1	1.6	1.1	0.2	2.8	89.3
	42.9	8.6	1.1	8.5	14.0	0.1	10.7	1.4	1.0	0.2	2.5	88.5
	44.4	8.9	1.1	8.4	14.1	0.2	11.9	1.5	1.0	0.2	2.6	91.5
	44.7	9.0	1.2	8.4	14.3	0.5	11.8	1.5	1.0	0.1	2.6	92.4
	44.5	9.1	1.1	8.4	14.0	0.2	11.9	1.4	1.0	0.2	2.7	91.7
<b>Amphibole Run 8</b>												
	45.3	8.6	1.5	13.1	10.7	0.3	11.4	1.4	0.9	0.4	1.6	93.3
	45.3	8.3	1.3	12.8	10.5	0.3	11.2	1.3	1.0	0.4	1.4	92.3
	44.7	8.2	1.3	12.5	9.8	0.2	11.4	1.4	0.9	0.4	1.5	90.6
	44.3	8.1	1.1	11.5	9.2	0.4	11.6	1.3	0.9	0.4	1.2	88.6
	44.6	8.2	1.2	12.1	9.7	0.2	11.6	1.4	0.9	0.4	1.5	90.3
	45.0	8.4	1.3	12.6	10.4	0.3	11.4	1.3	0.9	0.4	1.6	91.8

	SiO <sub>2</sub>	Al <sub>2</sub> O <sub>3</sub>	TiO <sub>2</sub>	FeO	MgO	MnO	CaO	Na <sub>2</sub> O	K <sub>2</sub> O	Cl	In <sub>2</sub> O <sub>3</sub>	Total
<b>Amphibole Run 9</b>												
	41.9	8.4	1.5	10.2	14.7	0.2	12.1	1.6	1.0	0.2	3.5	91.7
	44.4	9.3	1.4	10.2	14.5	0.2	12.1	1.6	1.0	0.2	3.5	94.9
	45.2	9.1	1.3	9.7	14.8	0.2	12.1	1.5	0.9	0.2	3.3	94.9
	44.6	9.3	1.4	9.8	14.5	0.3	12.1	1.5	1.0	0.2	3.4	94.6
	44.7	9.2	1.5	10.0	14.4	0.2	12.2	1.5	1.0	0.2	3.4	94.9
	44.7	9.2	1.5	10.0	14.3	0.2	12.2	1.5	1.0	0.2	3.5	94.8
	44.8	9.5	1.5	10.3	14.1	0.3	12.5	1.6	1.1	0.2	3.7	95.7
<b>Amphibole Run 10</b>												
	44.7	8.7	1.8	12.7	11.9	0.2	11.1	1.5	0.9	0.3	1.0	93.7
	44.9	8.5	1.8	12.9	12.1	0.3	11.2	1.5	0.8	0.3	1.4	94.1
	44.9	8.5	1.8	13.0	11.9	0.3	11.1	1.5	0.8	0.3	1.5	94.0
	45.1	8.1	1.8	12.2	12.1	0.3	11.2	1.4	0.8	0.2	0.9	93.0
	44.8	8.2	1.7	12.3	12.0	0.3	10.9	1.4	0.8	0.2	1.5	92.6
	45.4	8.5	1.7	12.8	12.0	0.3	11.3	1.5	0.8	0.2	1.5	94.5
	46.1	8.5	1.6	12.0	11.2	0.3	10.6	1.4	0.8	0.2	1.4	92.7
<b>Amphibole Run 11.1</b>												
	47.5	5.3	0.7	13.3	14.9	0.6	11.9	0.9	0.4	0.1	0.04	95.6
	48.5	3.5	0.2	11.9	14.2	0.6	11.6	0.7	0.3	0.2	0.04	91.5
	47.6	5.6	0.7	14.1	13.1	0.8	11.7	0.8	0.5	0.0	0.02	95.0
<b>Amphibole Run 11.2</b>												
	43.2	5.4	0.9	13.9	11.6	0.4	11.9	1.0	0.5	0.3	0.6	89.9
	46.5	4.8	0.4	12.9	14.1	0.3	11.1	0.9	0.4	0.2	0.4	92.1
	47.8	6.0	0.7	14.0	13.7	0.5	11.7	1.0	0.5	0.1	0.9	96.8
	48.4	5.6	0.7	14.2	12.7	0.7	11.6	0.8	0.5	0.0	0.4	95.5
	46.0	5.3	0.7	13.8	14.1	0.7	11.5	0.9	0.5	0.1	0.9	94.6
<b>Amphibole Run 11.3</b>												
	43.8	5.0	0.7	13.5	13.0	0.6	11.5	0.8	0.5	0.1	1.6	91.1
<b>Amphibole Run 11.4</b>												
	42.0	7.9	1.4	12.5	13.2	0.3	11.6	1.3	0.8	0.2	3.3	94.4

	SiO <sub>2</sub>	Al <sub>2</sub> O <sub>3</sub>	TiO <sub>2</sub>	FeO	MgO	MnO	CaO	Na <sub>2</sub> O	K <sub>2</sub> O	Cl	In <sub>2</sub> O <sub>3</sub>	Total
<b>Amphibole Run 13</b>												
43.1	9.0	1.7	11.1	11.8	0.2	11.1	1.5	1.0	0.3	4.0	94.7	
43.4	9.0	1.8	11.3	12.0	0.3	11.2	1.4	0.9	0.2	3.8	95.4	
43.6	9.0	1.8	11.2	12.0	0.2	11.4	1.4	0.9	0.2	3.8	95.5	
43.3	9.2	1.9	11.4	11.7	0.3	11.3	1.4	1.0	0.2	3.8	95.5	
43.0	8.7	1.3	10.9	11.3	0.4	10.6	1.3	1.1	0.2	4.2	93.0	
40.8	8.5	1.4	12.5	11.6	0.3	11.1	1.2	0.9	0.2	5.0	93.6	
41.5	8.5	1.5	11.7	12.5	0.3	11.0	1.4	0.9	0.3	4.7	94.2	
41.8	8.5	1.5	11.3	14.3	0.4	11.3	1.7	1.0	0.3	4.6	96.6	
42.7	8.5	1.7	11.5	12.8	0.3	11.2	1.4	0.9	0.3	4.2	95.4	
<b>Amphibole Run 14.1</b>												
43.2	7.4	1.2	12.5	12.7	0.3	10.8	1.3	0.5	0.2	1.9	90.1	
44.8	7.5	1.4	12.9	13.7	0.4	10.8	0.9	0.5	0.2	2.1	93.2	
43.5	7.4	1.4	13.0	12.8	0.3	10.7	1.0	0.5	0.2	2.0	90.7	
44.5	8.0	1.6	13.0	14.4	0.3	11.0	1.3	0.5	0.2	1.8	94.9	
43.8	8.3	1.3	13.3	13.2	0.3	10.9	1.1	0.5	0.2	1.8	92.9	
44.2	7.6	1.5	13.3	13.1	0.3	11.4	1.1	0.5	0.2	2.2	93.1	
<b>Amphibole Run 14.2</b>												
47.3	5.6	0.7	14.0	13.4	0.6	11.7	0.9	0.4	0.0	0.1	94.5	

## Glass

	SiO <sub>2</sub>	Al <sub>2</sub> O <sub>3</sub>	TiO <sub>2</sub>	FeO	MgO	MnO	CaO	Na <sub>2</sub> O	K <sub>2</sub> O	Cl	In <sub>2</sub> O <sub>3</sub>	Total
<b>Amphibole Run 4</b>												
67.2	12.9	0.1	0.7	0.12	b.d.	1.2	2.1	4.9	0.32	0.13		89.5
67.9	12.5	0.1	0.7	0.12	b.d.	1.0	2.5	5.3	0.36	0.14		90.6
68.5	12.3	0.1	0.7	0.13	b.d.	1.0	1.5	5.1	0.31	0.11		89.5
68.7	12.2	0.1	0.8	0.08	0.05	0.9	1.7	5.1	0.30	0.09		89.8
67.4	12.3	0.1	0.6	0.10	b.d.	1.1	2.9	5.0	0.30	0.07		89.7
67.3	12.0	0.1	0.6	0.11	b.d.	0.8	2.6	5.3	0.27	0.07		89.1
66.4	14.4	b.d.	0.6	0.09	b.d.	1.9	3.4	4.5	0.24	0.06		91.7
68.1	12.7	0.1	0.7	0.13	b.d.	1.2	2.8	5.1	0.29	0.07		91.0
67.6	12.2	b.d.	0.6	0.13	b.d.	0.9	2.7	5.3	0.32	0.05		89.8
65.6	14.7	0.2	0.6	0.09	0.08	2.1	3.4	4.3	0.23	0.04		91.3
66.7	12.2	b.d.	0.6	0.13	b.d.	0.9	2.7	5.2	0.29	0.07		88.7
<b>Amphibole Run 6</b>												
67.9	14.8	0.11	0.6	0.10	0.08	2.1	3.9	4.7	0.29	0.11		94.6
68.1	12.7	0.12	0.6	0.12	0.10	0.9	3.2	5.6	0.31	0.09		91.7
69.3	13.2	0.10	0.6	0.08	b.d.	0.9	3.3	5.7	0.30	0.08		93.4
68.9	13.0	0.07	0.5	0.10	b.d.	0.9	3.3	5.6	0.29	0.09		92.6
69.1	12.9	b.d.	0.6	0.09	b.d.	0.9	3.3	5.6	0.33	0.08		92.8
66.4	16.6	0.10	0.6	0.06	b.d.	2.9	4.5	4.1	0.20	0.07		95.5
68.9	12.7	0.16	0.7	0.11	0.06	1.0	3.0	5.6	0.31	0.11		92.4
<b>Amphibole Run 7</b>												
69.9	15.0	0.1	0.68	0.11	b.d.	2.2	3.4	4.9	0.26	0.12		96.4
70.9	13.9	0.1	0.64	0.13	0.09	1.7	3.1	5.3	0.28	0.12		96.0
71.7	12.5	0.1	0.71	0.13	b.d.	0.9	2.8	5.8	0.35	0.11		94.9
71.9	12.4	0.1	0.75	0.14	0.08	1.0	2.8	5.7	0.33	0.10		95.1
71.9	12.2	0.1	0.67	0.12	b.d.	0.9	2.8	5.7	0.29	0.09		94.7
72.8	13.2	0.1	0.68	0.09	b.d.	1.0	2.8	5.7	0.32	0.09		96.5
71.8	13.5	0.1	0.70	0.11	b.d.	1.1	2.9	5.5	0.29	0.10		95.9
71.5	13.9	0.1	0.68	0.12	b.d.	1.3	3.0	5.3	0.30	0.11		96.0
71.6	13.5	0.1	0.68	0.17	b.d.	1.2	2.9	5.5	0.31	0.12		96.1

	SiO <sub>2</sub>	Al <sub>2</sub> O <sub>3</sub>	TiO <sub>2</sub>	FeO	MgO	MnO	CaO	Na <sub>2</sub> O	K <sub>2</sub> O	Cl	In <sub>2</sub> O <sub>3</sub>	Total
<b>Amphibole Run 8</b>												
	72.8	12.8	0.1	0.8	0.1	b.d.	1.2	3.1	5.0	0.3	0.06	96.2
	73.4	12.5	0.1	0.7	0.1	0.07	1.0	3.0	5.1	0.3	0.05	96.2
	72.2	12.2	0.1	0.8	0.1	0.09	1.0	2.7	4.8	0.3	0.05	94.2
	71.8	12.6	0.1	0.7	0.0	0.07	1.1	3.0	5.0	0.3	0.04	94.7
	73.3	12.6	0.1	0.9	0.1	b.d.	1.0	3.1	5.1	0.3	0.05	96.6
	72.6	12.4	0.0	0.9	0.1	b.d.	0.9	2.9	5.1	0.3	0.06	95.2
	71.7	12.3	0.1	0.7	0.1	0.1	1.1	2.9	4.9	0.4	0.06	94.2
<b>Amphibole Run 9</b>												
	71.7	13.3	0.08	0.52	0.10	b.d.	0.9	2.9	5.8	0.32	0.11	95.6
	70.6	15.2	0.08	0.54	0.09	0.09	1.9	3.5	5.1	0.26	0.07	97.3
	71.8	13.3	0.12	0.59	0.11	0.07	1.0	2.9	5.9	0.31	0.09	96.0
	71.9	13.2	0.11	0.60	0.12	0.10	0.9	2.9	5.9	0.33	0.09	96.0
	72.7	13.4	0.06	0.62	0.12	0.08	0.9	2.8	5.8	0.31	0.09	96.7
	73.9	11.5	0.14	0.61	0.09	b.d.	0.6	2.6	5.6	0.27	0.08	95.2
	69.8	14.7	b.d.	0.69	0.09	b.d.	1.8	3.4	5.1	0.25	0.06	95.8
	70.3	13.1	0.06	0.68	0.13	b.d.	0.9	2.9	5.9	0.32	0.10	94.2
	69.2	14.0	0.10	0.68	0.13	b.d.	1.4	3.1	5.5	0.29	0.09	94.4
<b>Amphibole Run 10</b>												
	69.3	11.6	0.1	0.8	0.1	b.d.	0.9	2.7	4.8	0.3	0.03	90.6
	67.6	14.4	0.1	0.6	0.1	b.d.	2.4	3.6	4.0	0.3	0.03	93.0
	68.1	12.2	0.1	0.7	0.1	b.d.	1.3	2.8	4.4	0.3	0.03	90.0
	67.6	13.3	0.1	0.7	0.1	b.d.	1.8	3.1	4.3	0.3	0.02	91.3
	69.5	11.0	0.1	0.8	0.1	b.d.	0.9	2.7	4.8	0.3	0.04	90.2
	69.8	11.9	0.1	0.7	0.1	b.d.	1.1	2.8	4.7	0.3	0.03	91.6
	68.6	11.6	0.1	0.8	0.1	b.d.	0.9	2.7	4.7	0.3	0.04	89.8
	68.0	12.6	0.1	0.7	0.1	b.d.	1.5	3.1	4.5	0.3	0.03	91.0
	67.6	12.8	0.1	0.7	0.1	0.10	1.4	3.1	4.5	0.3	0.04	90.8
<b>Amphibole Run 11</b>												
	69.8	13.3	0.1	0.6	0.1	0.09	1.0	2.8	5.2	0.4	0.10	93.2
	68.0	13.3	0.1	0.5	0.1	b.d.	0.9	2.8	5.3	0.4	0.10	91.3
	67.4	13.1	0.0	0.5	0.1	b.d.	0.9	2.8	5.3	0.3	0.09	90.4
	68.6	13.8	0.1	0.6	0.1	0.06	1.2	2.9	5.0	0.3	0.09	92.7
	68.6	13.0	0.1	0.6	0.1	b.d.	1.0	2.8	5.2	0.4	0.10	91.6
	68.7	12.9	0.1	0.7	0.1	b.d.	1.0	2.7	5.2	0.4	0.11	91.6
	67.2	14.2	0.1	0.6	0.1	b.d.	1.6	3.0	4.9	0.4	0.10	92.1

	SiO <sub>2</sub>	Al <sub>2</sub> O <sub>3</sub>	TiO <sub>2</sub>	FeO	MgO	MnO	CaO	Na <sub>2</sub> O	K <sub>2</sub> O	Cl	In <sub>2</sub> O <sub>3</sub>	Total
<b>Amphibole Run 13</b>												
69.8	12.5	0.1	0.5	0.1	b.d.	0.9	2.4	5.1	0.34	0.08	91.8	
69.3	12.4	0.1	0.6	0.1	b.d.	1.0	2.6	5.0	0.32	0.08	91.4	
68.9	12.4	0.1	0.7	0.1	0.07	0.9	2.6	5.1	0.38	0.09	91.3	
68.8	13.3	0.1	0.6	0.1	b.d.	1.2	2.9	4.9	0.29	0.08	92.1	
68.0	12.7	0.1	0.6	0.1	0.08	1.1	2.6	5.1	0.34	0.07	90.7	
68.8	12.8	0.0	0.7	0.1	b.d.	0.8	2.8	5.0	0.40	0.09	91.5	
68.8	12.6	0.1	0.6	0.0	b.d.	0.9	2.7	5.1	0.31	0.09	90.9	
67.3	13.8	0.0	0.6	0.0	b.d.	1.4	3.1	4.7	0.29	0.08	91.2	
68.2	13.1	0.1	0.5	0.1	b.d.	1.1	2.8	4.9	0.31	0.10	91.0	
<b>Amphibole Run 14</b>												
68.7	13.6	0.1	0.6	0.0	0.12	0.6	3.0	5.4	0.04	0.02	92.2	
67.6	13.5	0.0	0.7	0.0	b.d.	0.6	3.0	5.3	0.05	0.02	90.8	
66.9	13.7	0.0	0.6	0.0	0.07	0.5	2.9	5.4	0.04	0.02	90.1	
66.5	13.7	0.1	0.7	0.1	b.d.	0.6	3.0	5.6	0.05	0.02	90.2	
68.4	13.1	0.1	0.8	0.1	b.d.	0.5	2.9	5.2	0.09	0.02	91.2	

Indium Silicates

	<b>In<sub>2</sub>O<sub>3</sub></b>	<b>FeO</b>	<b>SiO<sub>2</sub></b>	<b>Al<sub>2</sub>O<sub>3</sub></b>	<b>Total</b>
<b>Biotite Run 20</b>					
	65.1	2.3	32.9	0.14	100.4
	64.4	2.6	32.5	0.04	99.5
	64.6	2.3	32.9	0.05	99.8
	64.2	2.8	32.7	0.04	99.7
	63.3	3.2	32.9	0.08	99.5
<b>Biotite Run 23</b>					
	63.1	2.9	32.6	0.1	98.6
	63.9	2.7	32.5	0.1	99.2
	63.2	2.9	33.2	0.1	99.4
	64.8	2.1	32.4	0.2	99.5
<b>Biotite Run 24</b>					
	65.1	2.2	32.2	0.8	100.3
	63.4	2.2	32.8	1.6	100.0
	64.6	2.7	33.3	0.2	100.8
	64.9	2.5	32.6	0.1	100.2
<b>Biotite Run 27</b>					
	64.9	2.9	33.1	0.1	101.0
	64.5	2.7	32.9	0.9	101.0
	64.1	2.8	33.1	0.8	100.7
<b>Amphibole Run 4</b>					
	62.3	2.7	33.3	n.a.	98.3
	62.8	2.6	32.7	n.a.	98.0
	61.9	2.1	33.4	n.a.	97.4
	61.4	2.4	32.2	n.a.	96.0
	62.9	1.9	31.0	n.a.	95.7

## Appendix F: Gauss-Jordan Method for Reduction of Equilibria

Thermodynamic equilibria within a closed system are defined by a given set of phase components and system components. Each phase component can be written as a function of the sum of one or more system components. Phase and system components are thermodynamic components that define the minimum chemical variability in a phase or system, and are independently variable in a phase or system. Phase components define the chemical variability of a phase, i.e. alkali feldspar has the phase components  $\text{KAlSi}_3\text{O}_8$  and  $\text{NaAlSi}_3\text{O}_8$ . The phase component sanidine,  $\text{KAlSi}_3\text{O}_8$ , can be written in terms of its constituent system components  $\text{KAlO}_2 + 3\text{SiO}_2$ ,  $\text{KO}_{0.5} + \text{AlO}_{1.5} + 3\text{SiO}_2$ , or  $\text{K} + \text{Al} + 3\text{Si}$ , and  $4\text{O}_2$ , depending upon the selection of system components. Note that in a system with biotite and potassium feldspar and no other potassium- or aluminum-bearing phases, potassium and aluminum are constituents of the same system component, as they are always found together in the same proportions. Given a set of phase and system components, linearly independent equilibria can be derived to define the state of equilibrium the system.

The Gauss-Jordan reduction method of Thompson (1982) is a method that uses linear algebra to reduce a matrix of system components producing a set of linearly independent equilibria. These equilibria can then be added and subtracted from one another to describe all equilibria within the system. This method requires the use of two matrices; one matrix of system components and one matrix of phase components. The matrix of system components is reduced to a row echelon form,

using row operations. These operations are then performed on the corresponding matrix of phase components to produce a set of equilibria.

The biotite thermodynamic equilibria listed in equations 34 through 40 are derived in this manner. In Table F.1 each column is a phase component, containing 0's with a single 1, where the row containing the 1 corresponds to the row in Table F.2 containing the appropriate system components, thus Table F.1 is equal to Table F.2. The reduction of Table F.2 results in Table F.3 with 7 rows containing all zeros (17 phase components minus 10 system components). These rows correspond to rows in Table F.4 containing the coefficients of the phases in that equilibrium. Thus, the last 7 rows of Table F.4 indicate a set of equilibria that can be added or subtracted to derive the equilibria of interest corresponding to equations 34 through 40. The same procedure is done for table F.5 through F.9 to obtain amphibole equilibria (equations 47 to 54).

Table F.1  
Starting matrix of phase components (Biotite Experiments)

	Phlogopite	Annite	Indium Biotite	K-feldspar	Enstatite	Ferrosilite	Magnetite	Albite	Water	HCl	NaCl	KCl	In	SiO <sub>2</sub>	In <sub>2</sub> O <sub>3</sub>	InCl <sub>3</sub> (aq)	O <sub>2</sub>
1	0	0	0	0	0	0	0	0	0	0	0	0	0	0	0	0	0
0	1	0	0	0	0	0	0	0	0	0	0	0	0	0	0	0	0
0	0	1	0	0	0	0	0	0	0	0	0	0	0	0	0	0	0
0	0	0	1	0	0	0	0	0	0	0	0	0	0	0	0	0	0
0	0	0	0	1	0	0	0	0	0	0	0	0	0	0	0	0	0
0	0	0	0	0	1	0	0	0	0	0	0	0	0	0	0	0	0
0	0	0	0	0	0	1	0	0	0	0	0	0	0	0	0	0	0
0	0	0	0	0	0	0	1	0	0	0	0	0	0	0	0	0	0
0	0	0	0	0	0	0	0	1	0	0	0	0	0	0	0	0	0
0	0	0	0	0	0	0	0	0	1	0	0	0	0	0	0	0	0
0	0	0	0	0	0	0	0	0	0	1	0	0	0	0	0	0	0
0	0	0	0	0	0	0	0	0	0	0	1	0	0	0	0	0	0
0	0	0	0	0	0	0	0	0	0	0	0	1	0	0	0	0	0
0	0	0	0	0	0	0	0	0	0	0	0	0	1	0	0	0	0
0	0	0	0	0	0	0	0	0	0	0	0	0	0	1	0	0	0
0	0	0	0	0	0	0	0	0	0	0	0	0	0	0	1	0	0
0	0	0	0	0	0	0	0	0	0	0	0	0	0	0	0	1	0
0	0	0	0	0	0	0	0	0	0	0	0	0	0	0	0	0	1



Table F.4

Matrix generated after performing row operations used to reduce Table F.1 (Biotite Experiments)

	Phlogopite	Annite	Indium Biotite	K-feldspar	Enstatite	Ferrosilite	Magnetite	Albite	Water	HCl	In	NaCl	KCl	SiO <sub>2</sub>	In <sub>2</sub> O <sub>3</sub>	InCl <sub>3</sub> (aq)	O <sub>2</sub>
1.0	0.0	0.0	1.0	0.0	0.0	0.0	0.0	0.0	0.0	0.0	0.0	0.0	0.0	0.0	0.0	0.0	0.0
0.0	0.0	0.0	0.0	0.0	0.0	0.0	0.0	1.0	-0.5	0.0	0.0	0.0	0.0	0.0	0.0	0.0	0.0
0.3	0.0	-0.3	0.0	0.0	0.0	0.0	0.0	0.0	0.0	0.0	0.0	0.0	0.0	0.0	0.0	0.0	0.0
-0.3	0.0	0.3	0.0	1.0	0.0	0.0	0.0	0.0	0.0	0.0	0.0	0.0	0.0	0.0	0.0	0.0	0.0
0.3	0.0	-0.3	0.0	-1.0	1.0	0.0	0.0	0.0	0.0	0.0	0.0	0.0	0.0	0.0	0.0	0.0	0.0
0.0	0.0	0.0	0.5	-0.5	0.0	0.0	0.0	0.0	0.0	0.0	0.0	0.0	0.0	0.0	0.0	0.0	0.0
0.0	0.0	0.0	-0.5	0.5	0.0	0.0	0.0	0.0	0.0	1.0	0.0	0.0	0.0	0.0	0.0	0.0	0.0
0.0	0.0	0.0	0.5	-0.5	0.0	0.0	0.0	0.0	-0.5	0.0	0.0	0.0	0.0	0.0	0.0	0.0	0.0
0.0	0.0	0.0	0.0	0.0	0.0	0.0	0.0	0.0	0.5	-1.0	1.0	0.0	0.0	0.0	0.0	0.0	0.0
-1.0	0.0	0.0	0.0	1.0	3.0	-3.0	1.0	0.0	1.0	0.0	0.0	0.0	0.0	0.0	0.0	0.0	0.0
-1.0	1.0	0.0	0.0	0.0	3.0	-3.0	0.0	0.0	0.0	0.0	0.0	0.0	0.0	0.0	0.0	0.0	0.0
0.0	0.0	0.0	0.0	-1.0	0.0	0.0	0.0	1.0	0.0	0.0	-1.0	1.0	0.0	0.0	0.0	0.0	0.0
-1.5	0.0	0.0	-0.5	2.0	4.5	-4.5	1.5	0.0	2.0	0.0	0.0	0.0	1.0	0.0	0.0	0.0	0.0
0.3	0.0	0.0	0.0	-0.3	-1.0	0.0	0.0	0.0	-0.3	0.0	0.0	0.0	0.0	1.0	0.0	0.0	0.0
0.0	0.0	0.0	-1.0	1.0	0.0	0.0	0.0	0.0	1.0	0.0	0.0	0.0	0.0	0.0	0.0	0.0	0.0
0.0	0.0	0.0	-0.5	0.5	0.0	0.0	0.0	0.0	2.0	-3.0	0.0	0.0	0.0	0.0	0.0	1.0	0.0
2.0	0.0	0.0	0.0	-2.0	-6.0	6.0	-2.0	0.0	-2.0	0.0	0.0	0.0	0.0	0.0	0.0	0.0	0.0

Table F.5

Starting matrix of phase components (Amphibole Experiments)

		In-Al-																
Mg-Hbl	Tr	Ferro-Tr	Ts	In-Mg-Ts	Ed	Water	HCl	InCl <sub>3</sub> (aq)	In	SiO <sub>2</sub>	In <sub>2</sub> O <sub>3</sub>	Al <sub>2</sub> O <sub>3</sub>	O <sub>2</sub>	MgO	FeO	CaO	Na <sub>2</sub> O	
1	0	0	0	0	0	0	0	0	0	0	0	0	0	0	0	0	0	0
0	1	0	0	0	0	0	0	0	0	0	0	0	0	0	0	0	0	0
0	0	1	0	0	0	0	0	0	0	0	0	0	0	0	0	0	0	0
0	0	0	1	0	0	0	0	0	0	0	0	0	0	0	0	0	0	0
0	0	0	0	1	0	0	0	0	0	0	0	0	0	0	0	0	0	0
0	0	0	0	0	1	0	0	0	0	0	0	0	0	0	0	0	0	0
0	0	0	0	0	0	1	0	0	0	0	0	0	0	0	0	0	0	0
0	0	0	0	0	0	0	1	0	0	0	0	0	0	0	0	0	0	0
0	0	0	0	0	0	0	0	1	0	0	0	0	0	0	0	0	0	0
0	0	0	0	0	0	0	0	0	1	0	0	0	0	0	0	0	0	0
0	0	0	0	0	0	0	0	0	0	1	0	0	0	0	0	0	0	0
0	0	0	0	0	0	0	0	0	0	0	1	0	0	0	0	0	0	0
0	0	0	0	0	0	0	0	0	0	0	0	1	0	0	0	0	0	0
0	0	0	0	0	0	0	0	0	0	0	0	0	1	0	0	0	0	0
0	0	0	0	0	0	0	0	0	0	0	0	0	0	1	0	0	0	0
0	0	0	0	0	0	0	0	0	0	0	0	0	0	0	1	0	0	0
0	0	0	0	0	0	0	0	0	0	0	0	0	0	0	0	1	0	0
0	0	0	0	0	0	0	0	0	0	0	0	0	0	0	0	0	1	0



Table F.8

Matrix generated after performing row operations used to reduce Table F.6 (Amphibole Experiments)

Mg-Hbl	Ferro-		In-Al-Ts		In-Mg-Ts		Ed	Water	HCl	InCl <sub>3</sub>		In	SiO <sub>2</sub>	In <sub>2</sub> O <sub>3</sub>	Al <sub>2</sub> O <sub>3</sub>	O <sub>2</sub>	MgO	FeO	CaO	Na <sub>2</sub> O
	Tr	Tr	In-Al-Ts	Ts	In-Mg-Ts	(aq)				InCl <sub>3</sub>										
0.0	0.0	-1.0	0.0	0.5	1.0	0.0	0.0	0.0	0.0	-9.33	16.0	0.0	0.0	0.0	0.0	0.0	0.0	0.0	0.0	0.0
0.0	0.0	0.0	0.0	0.0	0.0	0.0	0.0	1.0	0.0	0.0	0.0	0.0	0.0	0.0	0.0	0.0	0.0	0.0	0.0	0.0
0.0	0.0	0.5	0.0	0.0	0.0	0.0	0.0	0.0	0.0	-5.33	8.0	0.0	0.0	0.0	0.0	0.0	0.0	0.0	0.0	0.0
0.0	0.0	-0.5	0.5	1.0	0.0	0.0	0.0	0.0	0.0	1.33	0.0	0.0	0.0	0.0	0.0	0.0	0.0	0.0	0.0	0.0
0.0	0.0	0.0	0.5	-0.5	0.0	0.0	0.0	0.0	0.0	0.0	0.0	0.0	0.0	0.0	0.0	0.0	0.0	0.0	0.0	0.0
0.14	0.0	-0.1	-0.14	0.14	0.0	0.0	0.0	0.0	0.0	0.19	0.0	0.0	0.0	0.0	0.0	0.0	0.0	0.0	0.0	0.0
0.5	-0.7	0.2	-0.5	0.5	0.0	0.0	0.0	0.0	0.0	0.67	0.0	0.0	0.0	0.0	0.0	0.0	0.0	0.0	0.0	0.0
0.0	0.0	0.0	0.0	0.0	0.0	0.0	0.5	0.0	0.0	0.0	0.3	0.0	0.0	0.0	0.0	0.0	0.0	0.0	0.0	0.0
0.33	0.33	0.0	0.33	-1.0	0.0	0.0	2.0	-4.0	1.33	1.33	1.3	0.0	0.0	0.0	0.0	0.0	0.0	0.0	0.0	0.0
0.0	0.0	0.0	0.0	0.0	0.0	0.0	1.0	-2.0	0.67	0.67	-0.7	0.0	0.0	0.0	0.0	0.0	0.0	0.0	0.0	0.0
-0.33	-0.33	0.0	-0.33	1.0	0.0	0.0	-2.0	4.0	-1.33	-1.33	0.0	1.0	0.0	0.0	0.0	0.0	0.0	0.0	0.0	0.0
0.0	0.0	0.0	0.0	0.0	0.0	0.0	-3.0	6.0	-2.0	-2.0	0.0	0.0	1.0	0.0	0.0	0.0	0.0	0.0	0.0	0.0
-2.0	1.0	0.0	0.0	1.0	0.0	0.0	-3.0	6.0	-2.0	-2.0	0.0	0.0	0.0	1.0	0.0	0.0	0.0	0.0	0.0	0.0
0.0	0.0	0.0	0.0	0.0	0.0	0.0	-2.0	4.0	-1.33	1.3	0.0	0.0	0.0	0.0	1.0	0.0	0.0	0.0	0.0	0.0
-0.67	0.33	0.0	0.33	0.0	0.0	0.0	-1.0	2.0	-0.67	-0.67	0.0	0.0	0.0	0.0	0.0	0.0	1.0	0.0	0.0	0.0
-0.67	0.5	-0.2	0.33	0.0	0.0	0.0	-1.0	2.0	-0.67	-0.67	0.0	0.0	0.0	0.0	0.0	0.0	0.0	1.0	0.0	0.0
3.0	0.0	0.0	0.5	-4.0	0.0	0.0	11.0	-21.0	7.0	7.0	0.0	0.0	0.0	0.0	0.0	0.0	0.0	0.0	1.0	0.0
1.33	0.33	0.0	-0.67	1.0	-2.0	0.0	-1.0	2.0	-0.67	-0.67	0.0	0.0	0.0	0.0	0.0	0.0	0.0	0.0	0.0	1.0

## Bibliography

### Reference List

- Adam, J., and Green, T., 2006, Trace element partitioning between mica- and amphibole-bearing garnet lherzolite and hydrous basanitic melt: 1. Experimental results and the investigation of controls on partitioning behaviour: *Contributions to Mineralogy and Petrology*, v. 152, no. 1, p. 1-17, doi:10.1007/s00410-006-0085-4.
- Ague, J. J., and Brimhall, G. H., 1988, Magmatic arc asymmetry and distribution of anomalous plutonic belts in the batholiths of California: Effects of assimilation, crustal thickness, and depth of crystallization: *GSA Bulletin*, v. 100, no. 6, p. 912-927, doi:10.1130/0016-7606(1988)100<0912:MAAADO>2.3.CO;2.
- Ahrens, L., and Liebenberg, u. W., 1950, Tin and indium in mica, as determined spectrochemically: *American Mineralogist*, v. 35, no. 7-8, p. 571-578.
- Anderson, J. L., and Bender, E. E., 1989, Nature and origin of Proterozoic A-type granitic magmatism in the southwestern United States of America: *Lithos*, v. 23, no. 1, p. 19-52, doi:10.1016/0024-4937(89)90021-2.
- Annen, C., Blundy, J. D., and Sparks, R. S. J., 2006, The Genesis of Intermediate and Silicic Magmas in Deep Crustal Hot Zones: *Journal of Petrology*, v. 47, no. 3, p. 505-539, doi:10.1093/petrology/egi084.
- Arevalo Jr., R., and McDonough, W. F., 2008, Tungsten geochemistry and implications for understanding the Earth's interior: *Earth and Planetary Science Letters*, v. 272, no. 3-4, p. 656-665, doi:10.1016/j.epsl.2008.05.031.
- Audétat, A., and Li, W., 2017, The genesis of Climax-type porphyry Mo deposits: Insights from fluid inclusions and melt inclusions: *Ore Geology Reviews*, v. 88, p. 436-460, doi:10.1016/j.oregeorev.2017.05.018.
- Barrie, C., and Hannington, M., 1999, Classification of volcanic-associated massive sulfide deposits based on host-rock composition: *Reviews in Economic Geology*, v. 8, p. 1-11.
- Bateman, P. C., 1992, Plutonism in the central part of the Sierra Nevada Batholith, California, U.S Geological Survey Professional Paper 1483, p. 186.
- Blundy, J., and Wood, B., 1994, Prediction of crystal melt partition coefficients from elastic moduli: *Nature*, v. 372, no. 6505, p. 452-454.
- Bohlen, S. R., Peacor, D. R., and Essene, E. J., 1980, Crystal chemistry of a metamorphic biotite and its significance in water barometry: *American Mineralogist*, v. 65, no. 1-2, p. 55-62.
- Bowen, N., 1928, *Evolution of the igneous rocks*, Princeton Univ. Press.
- Bower, W., Head, W., Droop, G. T. R., Zan, R., Patrick, R. A. D., Wincott, P., and Haigh, S. J., 2015, High-resolution imaging of biotite using focal series exit wavefunction restoration and the graphene mechanical exfoliation method: *Mineralogical Magazine*, v. 79, no. 2, p. 337-344, doi:10.1180/minmag.2015.079.2.11.

- Breiter, K., Vasinova\_Galiova, M., Korbelova, Z., Vankova, M., and Kanicky, V., 2015, Obsahy galia, india a thalia v granitoidech Ceskeho masivu a jejich hlavnich horninotvornych mineralech: Zpravy o geologickych vyzkumech, v. 2014, p. 79-84.
- Burt, D. M., Sheridan, M. F., Bikun, J. V., and Christiansen, E. H., 1982, Topaz rhyolites; distribution, origin, and significance for exploration: *Economic Geology*, v. 77, no. 8, p. 1818-1836, doi:10.2113/gsecongeo.77.8.1818.
- Candela, P. A., 1986, Toward a thermodynamic model for the halogens in magmatic systems: An application to melt-vapor-apatite equilibria: *Chemical Geology*, v. 57, no. 3, p. 289-301, doi:10.1016/0009-2541(86)90055-0.
- Candela, P. A., 1989a, Felsic magmas, volatiles, and metallogenesis: *Reviews in Economic Geology*, v. 4, p. 223-233.
- Candela, P. A., 1989b, Magmatic ore-forming fluids: thermodynamic and mass-transfer calculations of metal concentrations. In ore deposition associated with magmas: *Reviews in Economic Geology*, v. 4, p. 203-221.
- Candela, P. A., 1997, A Review of Shallow, Ore-related Granites: Textures, Volatiles, and Ore Metals: *Journal of Petrology*, v. 38, no. 12, p. 1619-1633, doi:10.1093/etroj/38.12.1619.
- Candela, P. A., and Bouton, S. L., 1990, The influence of oxygen fugacity on tungsten and molybdenum partitioning between silicate melts and ilmenite: *Economic Geology*, v. 85, no. 3, p. 633-640, doi:10.2113/gsecongeo.85.3.633.
- Candela, P. A., and Holland, H. D., 1984, The partitioning of copper and molybdenum between silicate melts and aqueous fluids: *Geochimica et Cosmochimica Acta*, v. 48, no. 2, p. 373-380, doi:10.1016/0016-7037(84)90257-6.
- Candela, P. A., and Holland, H. D., 1986, A mass transfer model for copper and molybdenum in magmatic hydrothermal systems; the origin of porphyry-type ore deposits: *Economic Geology*, v. 81, no. 1, p. 1-19, doi:10.2113/gsecongeo.81.1.1.
- Candela, P. A., and Piccoli, P. M., 2005, Magmatic Processes in the Development of Porphyry-type Ore Systems, *in* Hedenquist, J. W., Thompson, J. F. H., Goldfarb, R. J., and Richards, J. P., eds., *Society of Economic Geologists, Volume 100th Anniversary*, p. 25-37.
- Chappell, B. W., and White, A. J. R., 1974, Two contrasting granite types: *Pacific Geology*, v. 8, p. 173-174.
- Chappell, B. W., and White, A. J. R., 2001, Two contrasting granite types: 25 years later: *Australian Journal of Earth Sciences*, v. 48, no. 4, p. 489-499, doi:10.1046/j.1440-0952.2001.00882.x.
- Chou, I. M., 1986, Permeability of precious metals to hydrogen at 2kb total pressure and elevated temperatures: *American Journal of Science*, v. 286, no. 8, p. 638-658.
- Christiansen, E., Bikun, J., and Burt, D., 1980, Petrology and geochemistry of topaz rhyolites, western United States: US Department of Energy Open-File Report GJBX-225 (80), p. 37-122.

- Churakov, S. V., and Gottschalk, M., 2003a, Perturbation theory based equation of state for polar molecular fluids: I. Pure fluids: *Geochimica et Cosmochimica Acta*, v. 67, no. 13, p. 2397-2414, doi:10.1016/S0016-7037(02)01347-9.
- Churakov, S. V., and Gottschalk, M., 2003b, Perturbation theory based equation of state for polar molecular fluids: II. Fluid mixtures: *Geochimica et Cosmochimica Acta*, v. 67, no. 13, p. 2415-2425, doi:10.1016/S0016-7037(02)01348-0.
- Collins, W. J., Beams, S. D., White, A. J. R., and Chappell, B. W., 1982, Nature and origin of A-type granites with particular reference to southeastern Australia: *Contributions to Mineralogy and Petrology*, v. 80, no. 2, p. 189-200, doi:10.1007/bf00374895.
- Cook, N. J., Ciobanu, C. L., Pring, A., Skinner, W., Shimizu, M., Danyushevsky, L., Saini-Eidukat, B., and Melcher, F., 2009, Trace and minor elements in sphalerite: A LA-ICPMS study: *Geochimica et Cosmochimica Acta*, v. 73, no. 16, p. 4761-4791, doi:10.1016/j.gca.2009.05.045.
- Cook, N. J., Sundblad, K., Valkama, M., Nygård, R., Ciobanu, C. L., and Danyushevsky, L., 2011, Indium mineralisation in A-type granites in southeastern Finland: Insights into mineralogy and partitioning between coexisting minerals: *Chemical Geology*, v. 284, no. 1-2, p. 62-73, doi:10.1016/j.chemgeo.2011.02.006.
- Czamanske, G. K., and Wones, D. R., 1973, Oxidation During Magmatic Differentiation, Finnmarka Complex, Oslo Area, Norway: Part 2, The Mafic Silicates: *Journal of Petrology*, v. 14, no. 3, p. 349-380, doi:10.1093/petrology/14.3.349.
- Dailey, S. R., 2016, Geochemistry of the Fluorine- and Beryllium-Rich Spor Mountain Rhyolite, Western Utah [Masters Thesis]: Brigham Young University.
- Dill, H. G., Garrido, M. M., Melcher, F., Gomez, M. C., Weber, B., Luna, L. I., and Bahr, A., 2013, Sulfidic and non-sulfidic indium mineralization of the epithermal Au-Cu-Zn-Pb-Ag deposit San Roque (Provincia Rio Negro, SE Argentina) — with special reference to the “indium window” in zinc sulfide: *Ore Geology Reviews*, v. 51, p. 103-128, doi:10.1016/j.oregeorev.2012.12.005.
- Dingwell, D., Holtz, F., and Behrens, H., 1997, The solubility of H<sub>2</sub>O in peralkaline and peraluminous granitic melts: *American Mineralogist*, v. 82, no. 3, p. 434-437.
- Dingwell, D. B., Harris, D. M., and Scarfe, C. M., 1984, The Solubility of H<sub>2</sub>O in Melts in the System SiO<sub>2</sub>-Al<sub>2</sub>O<sub>3</sub>-Na<sub>2</sub>O-K<sub>2</sub>O at 1 to 2 kbars: *The Journal of Geology*, v. 92, no. 4, p. 387-395.
- Droop, G. T. R., 1987, A general equation for estimating Fe<sup>3+</sup> concentrations in ferromagnesian silicates and oxides from microprobe analyses, using stoichiometric criteria: *Mineralogical magazine*, v. 51, no. 361, p. 431-435.
- Drouin, D., Couture, A. R., Joly, D., Tastet, X., Aimez, V., and Gauvin, R., 2007, CASINO V2. 42—A Fast and Easy-to-use Modeling Tool for Scanning Electron Microscopy and Microanalysis Users: *Scanning*, v. 29, no. 3, p. 92-101.

- Drouin, D., Hovington, P., and Gauvin, R., 1997, CASINO: A new monte carlo code in C language for electron beam interactions—part II: Tabulated values of the mott cross section: *Scanning*, v. 19, no. 1, p. 20-28.
- Dymek, R. F., 1983, Titanium, aluminium and interlayer cation substitutions in biotite from high-grade gneisses, West Greenland: *American Mineralogist*, v. 68, no. 9-10, p. 880-899.
- Eugster, H. P., 1957, Heterogeneous reactions involving oxidation and reduction at high pressures and temperatures: *The Journal of Chemical Physics*, v. 26, no. 6, p. 1760-1761.
- Frank, M. R., 2001, An experimental investigation of ore metals in silicate melt-volatile phase systems [PhD.]: University of Maryland, 244 p.
- Frank, M. R., Simon, A. C., Pettke, T., Candela, P. A., and Piccoli, P. M., 2011, Gold and copper partitioning in magmatic-hydrothermal systems at 800 °C and 100 MPa: *Geochimica et Cosmochimica Acta*, v. 75, no. 9, p. 2470-2482, doi:10.1016/j.gca.2011.02.012.
- Franklin, J. M., Gibson, H., Jonasson, I., and Galley, A., 2005, Volcanogenic massive sulfide deposits: *Economic Geology 100th anniversary volume*, v. 98, p. 523-560.
- Galley, A. G., Hannington, M., and Jonasson, I., 2007, Volcanogenic massive sulphide deposits: *Mineral deposits of Canada: a synthesis of major deposit-types, district Metallogeny, the evolution of geological provinces, and exploration methods: Geological Association of Canada, Mineral Deposits Division, Special Publication*, v. 5, p. 141-161.
- Genkin, A. D., and Murav'eva, I. V., 1963, Indite and dzhaliindite, new indium minerals: *Zapiski Vsesoyuznogo Mineralogicheskogo Obshchestva*, v. 92, p. 445-457.
- Hammouda, T., and Cherniak, D. J., 2000, Diffusion of Sr in fluorophlogopite determined by Rutherford backscattering spectrometry: *Earth and Planetary Science Letters*, v. 178, no. 3, p. 339-349, doi:10.1016/S0012-821X(00)00089-3.
- Hannington, M., Poulsen, K., and Thomsen, J., 1999, Volcanogenic gold in the massive sulfide environment, *in* Barrie, C. T., and Hannington, M. D., eds., *Society of Economic Geologists*, p. 325-356.
- Harrison, W. J., 1981, Partition coefficients for REE between garnets and liquids: implications of non-Henry's Law behaviour for models of basalt origin and evolution: *Geochimica et Cosmochimica Acta*, v. 45, no. 9, p. 1529-1544, doi:10.1016/0016-7037(81)90283-0.
- Harrison, W. J., and Wood, B. J., 1980, An experimental investigation of the partitioning of REE between garnet and liquid with reference to the role of defect equilibria: *Contributions to Mineralogy and Petrology*, v. 72, no. 2, p. 145-155, doi:10.1007/BF00399474.
- Hawthorne, F. C., 1983, The crystal chemistry of the amphiboles; Introduction: *The Canadian Mineralogist*, v. 21, no. 2, p. 21-480.
- Hawthorne, F. C., Oberti, R., Harlow, G. E., Maresch, W. V., Martin, R. F., Schumacher, J. C., and Welch, M. D., 2012, Nomenclature of the amphibole

- supergroup: *American Mineralogist*, v. 97, no. 11-12, p. 2031-2048, doi:10.2138/am.2012.4276.
- Hazen, R. M., and Finger, L. W., 1979, Bulk modulus—volume relationship for cation-anion polyhedra: *Journal of Geophysical Research: Solid Earth*, v. 84, no. B12, p. 6723-6728, doi:10.1029/JB084iB12p06723.
- Hedenquist, J. W., and Lowenstern, J. B., 1994, The role of magmas in the formation of hydrothermal ore deposits: *Nature*, v. 370, no. 6490, p. 519-527.
- Hill, E., Wood, B. J., and Blundy, J. D., 2000, The effect of Ca-Tschermaks component on trace element partitioning between clinopyroxene and silicate melt: *Lithos*, v. 53, no. 3-4, p. 203-215, doi:10.1016/S0024-4937(00)00025-6.
- Hofmann, A., and Giletti, B. J., 1970, Diffusion of geochronologically important nuclides in minerals under hydrothermal conditions: *Eclogae Geologicae Helveticae*, v. 63, p. 141-150.
- Holland, H. D., 1972, Granites, Solutions, and Base Metal Deposits: *Economic Geology*, v. 67, no. 3, p. 281-301, doi:10.2113/gsecongeo.67.3.281.
- Holloway, J., The effect of fluorine on dehydration equilibria, *in Proceedings Geologic Society of America Abstracts with Programs 1977*, Volume 9, p. 1021.
- Holtz, F., Dingwell, D. B., and Behrens, H., 1993, Effects of F, B<sub>2</sub>O<sub>3</sub> and P<sub>2</sub>O<sub>5</sub> on the solubility of water in haplogranite melts compared to natural silicate melts: *Contributions to Mineralogy and Petrology*, v. 113, no. 4, p. 492-501, doi:10.1007/BF00698318.
- Hoover, J., 1978, The distribution of samarium and thulium between plagioclase and liquid in the systems An-Di and Ab-An-Di at 1300 C: *Carnegie Institute Washington Yearbook*, v. 77, p. 703-706.
- Hovington, P., Drouin, D., and Gauvin, R., 1997a, CASINO: A new Monte Carlo code in C language for electron beam interaction—part I: Description of the program: *Scanning*, v. 19, no. 1, p. 1-14.
- Hovington, P., Drouin, D., Gauvin, R., Joy, D. C., and Evans, N., 1997b, CASINO: A new Monte Carlo code in C language for electron beam interactions—part III: Stopping power at low energies: *Scanning*, v. 19, no. 1, p. 29-35.
- Hulen, J. B., Nielson, D. L., Goff, F., Gardner, J. N., and Charles, R. W., 1987, Molybdenum mineralization in an active geothermal system, Valles caldera, New Mexico: *Geology*, v. 15, no. 8, p. 748-752, doi:10.1130/0091-7613(1987)15<748:mmiaag>2.0.co;2.
- Inverno, C. M. C., and Hutchinson, R. W., 2006, Petrochemical discrimination of evolved granitic intrusions associated with Mount Pleasant deposits, New Brunswick, Canada: *Applied Earth Science*, v. 115, no. 1, p. 23-39, doi:10.1179/174327506X113037.
- Ishihara, S., and Endo, Y., 2007, Indium and other trace elements in volcanogenic massive sulfide ores from the Kuroko, Besshi and other types in Japan: *Bull. Geol. Surv. Japan*, v. 58, p. 7-22.
- Ishihara, S., Hoshino, K., Murakami, H., and Endo, Y., 2006, Resource Evaluation and Some Genetic Aspects of Indium in the Japanese Ore Deposits: *Resource Geology*, v. 56, no. 3, p. 347-364, doi:10.1111/j.1751-3928.2006.tb00288.x.

- Ishihara, S., Murakami, H., and Li, X., 2011a, Indium concentration in zinc ores in plutonic and volcanic environments: examples at the Dulong and Dachang mines, South China: *Bulletin of Geologic Survey of Japan*, v. 62, p. 259-272.
- Ishihara, S., Murakami, H., and Marquez-Zavalia, M. F., 2011b, Inferred Indium Resources of the Bolivian Tin-Polymetallic Deposits: *Resource Geology*, v. 61, no. 2, p. 174-191, doi:10.1111/j.1751-3928.2011.00157.x.
- Ito, J., 1968, Synthetic Indium Silicate and Indium Hydrogarnet: *American Mineralogist*, v. 53, no. 9-10, p. 1663-1673.
- Jackson, S., 2008, LAMTRACE data reduction software for LA-ICP-MS: *Laser Ablation-ICP-Mass Spectrometry in the Earth Sciences: Current Practices and Outstanding Issues* (Sylvester, P., Ed.), Mineralogical Association of Canada (MAC) Short Course Series, v. 40, p. 305-307.
- Jaffe, R., Price, J., Ceder, G., Eggert, R., Graedel, T., Gschneidner, K., Hitzman, M., Houle, F., Hurd, A., and Kelley, R., 2011, Energy critical elements: securing materials for emerging technologies, American Physical Society Panel on Public Affairs and the Materials Research Society, Washington, D.C., p. 1 - 26.
- JEOL, 2001, XM-17330/27330 Basic Software/ Quantitative Analysis Program, Japan, JEOL, 101 p.
- Jochum, K. P., Weis, U., Stoll, B., Kuzmin, D., Yang, Q., Raczek, I., Jacob, D. E., Stracke, A., Birbaum, K., Frick, D. A., Günther, D., and Enzweiler, J., 2011, Determination of Reference Values for NIST SRM 610–617 Glasses Following ISO Guidelines: *Geostandards and Geoanalytical Research*, v. 35, no. 4, p. 397-429, doi:10.1111/j.1751-908X.2011.00120.x.
- Jovic, S. M., Guido, D. M., Schalamuk, I. B., Ríos, F. J., Tassinari, C. C. G., and Recio, C., 2011, Pingüino In-bearing polymetallic vein deposit, Deseado Massif, Patagonia, Argentina: characteristics of mineralization and ore-forming fluids: *Mineralium Deposita*, v. 46, no. 3, p. 257-271, doi:10.1007/s00126-010-0324-5.
- Jugo, P. J., Candela, P. A., and Piccoli, P. M., 1999, Magmatic sulfides and Au:Cu ratios in porphyry deposits: an experimental study of copper and gold partitioning at 850°C, 100 MPa in a haplogranitic melt–pyrrhotite–intermediate solid solution–gold metal assemblage, at gas saturation: *Lithos*, v. 46, no. 3, p. 573-589, doi:10.1016/S0024-4937(98)00083-8.
- Karazhanov, S. Z., Ravindran, P., and Grossner, U., 2011, First-principles study on electronic structure, phase stability, and optical properties of  $\text{In}_2\text{X}_2\text{O}_7$  (X=C, Si, Ge or Sn): *Thin Solid Films*, v. 519, no. 19, p. 6561-6567, doi:10.1016/j.tsf.2011.04.221.
- Kayser, S., 2013, Partitioning of Indium Between Pyrrhotite and Silicate Melt, Undergraduate Senior Thesis, University of Maryland-College Park, 1-42, Unpublished, <http://www.geol.umd.edu/undergraduate/seniorthesisarchive.php> - 2010.
- Kooiman, G. J. A., McLeod, M. J., and Sinclair, W. D., 1986, Porphyry tungsten-molybdenum orebodies, polymetallic veins and replacement bodies, and tin-bearing greisen zones in the Fire Tower Zone, Mount Pleasant, New

- Brunswick: Economic Geology, v. 81, no. 6, p. 1356-1373, doi:10.2113/gsecongeo.81.6.1356.
- Large, R. R., McPhie, J., Gemmell, J. B., Herrmann, W., and Davidson, G. J., 2001, The Spectrum of Ore Deposit Types, Volcanic Environments, Alteration Halos, and Related Exploration Vectors in Submarine Volcanic Successions: Some Examples from Australia: Economic Geology, v. 96, no. 5, p. 913-938, doi:10.2113/gsecongeo.96.5.913.
- Mahood, G., and Hildreth, W., 1983, Large partition coefficients for trace elements in high-silica rhyolites: *Geochimica et Cosmochimica Acta*, v. 47, no. 1, p. 11-30, doi:10.1016/0016-7037(83)90087-X.
- Manning, D. A. C., 1981, The effect of fluorine on liquidus phase relationships in the system Qz-Ab-Or with excess water at 1 kb: *Contributions to Mineralogy and Petrology*, v. 76, no. 2, p. 206-215, doi:10.1007/bf00371960.
- Martin, J., 1983, An experimental study on the effects of lithium on the granite system, in Power, G. M., ed., *Research into the geology and geomorphology of S. W. England*, Volume 5, Ussher Society, p. 417-420.
- Matsui, Y., 1977, Crystal structure control in trace element partition between crystal and magma: *Bull. Soc. Fr. Mineral. Cristallogr.*, v. 100, p. 315-324.
- McDonough, W. F., and Sun, S. S., 1995, Chemical Evolution of the Mantle The composition of the Earth: *Chemical Geology*, v. 120, no. 3, p. 223-253, doi:10.1016/0009-2541(94)00140-4.
- Meinert, L. D., 1995, Compositional variation of igneous rocks associated with skarn deposits—chemical evidence for a genetic connection between petrogenesis and mineralization.
- Meinert, L. D., Dipple, G. M., and Nicolescu, S., 2005, World skarn deposits: *Economic Geology*, v. 100, no. 4, p. 299-336.
- Messous, Y., Chambon, B., Dejesus, M., Drain, D., Pastor, C., Garcia, A., Chaminade, J. P., Gaewdang, T., Fouassier, C., Jacquier, B., and Varrel, B., 1995, Indium Disilicate, A New Fast Scintillator: *Nuclear Instruments & Methods in Physics Research Section a-Accelerators Spectrometers Detectors and Associated Equipment*, v. 354, no. 2-3, p. 527-529, doi:10.1016/0168-9002(94)01007-2.
- Moura, M. A., Botelho, N. F., Olivo, G. R., Kyser, K., and Pontes, R. M., 2014, Genesis of the Proterozoic Mangabeira tin–indium mineralization, Central Brazil: Evidence from geology, petrology, fluid inclusion and stable isotope data: *Ore Geology Reviews*, v. 60, no. Supplement C, p. 36-49, doi:10.1016/j.oregeorev.2013.12.010.
- Mueller, R. F., 1972, Stability of biotite—a discussion: *American Mineralogist*, v. 57, no. 1-2, p. 300-316.
- Murakami, H., and Ishihara, S., 2013, Trace elements of Indium-bearing sphalerite from tin-polymetallic deposits in Bolivia, China and Japan: A femto-second LA-ICPMS study: *Ore Geology Reviews*, v. 53, no. Supplement C, p. 223-243, doi:10.1016/j.oregeorev.2013.01.010.
- Mysen, B. O., 1978, Limits of solution of trace elements in minerals according to Henry's law: Review of experimental data: *Geochimica et Cosmochimica Acta*, v. 42, no. 6, p. 871-885, doi:10.1016/0016-7037(78)90099-6.

- Nandedkar, R. H., Hürlimann, N., Ulmer, P., and Müntener, O., 2016, Amphibole–melt trace element partitioning of fractionating calc-alkaline magmas in the lower crust: an experimental study: *Contributions to Mineralogy and Petrology*, v. 171, no. 8, p. 71, doi:10.1007/s00410-016-1278-0.
- Naney, M. T., 1983, Phase equilibria of rock-forming ferromagnesian silicates in granitic systems: *American Journal of Science*, v. 283, no. 10, p. 993-1033, doi:10.2475/ajs.283.10.993.
- Ochs, F. A., and Lange, R. A., 1999, The Density of Hydrous Magmatic Liquids: *Science*, v. 283, no. 5406, p. 1314-1317, doi:10.1126/science.283.5406.1314.
- Ohta, E., 1989, Occurrence and Chemistry of Indium-containing Minerals from the Toyoha Mine, Hokkaido, Japan: *Mining Geology*, v. 39, no. 218, p. 355-372, doi:10.11456/shigenchishitsu1951.39.218\_355.
- Ohta, E., 1991, Polymetallic mineralization at the Toyoha mine, Hokkaido, Japan: *Mining Geology*, v. 41, no. 229, p. 279-295.
- Onuma, N., Higuchi, H., Wakita, H., and Nagasawa, H., 1968, Trace element partition between two pyroxenes and the host lava: *Earth and Planetary Science Letters*, v. 5, p. 47-51, doi:10.1016/S0012-821X(68)80010-X.
- Ottemann, J., 1940, Untersuchungen zur Verteilung von Spurenelementen, insbesondere Zinn, in Tiefengesteinen und einigen gesteinsbildenden Mineralien des Harzes.
- Pan, Y., Dong, P., and Chen, N., 2003, Non-Henry's Law behavior of REE partitioning between fluorapatite and CaF<sub>2</sub>-rich melts: Controls of intrinsic vacancies and implications for natural apatites: *Geochimica et Cosmochimica Acta*, v. 67, no. 10, p. 1889-1900, doi:10.1016/S0016-7037(02)01285-1.
- Papale, P., Moretti, R., and Barbato, D., 2006, The compositional dependence of the saturation surface of H<sub>2</sub>O + CO<sub>2</sub> fluids in silicate melts: *Chemical Geology*, v. 229, no. 1–3, p. 78-95, doi:10.1016/j.chemgeo.2006.01.013.
- Piccoli, P. M., 1992, Apatite chemistry in felsic magmatic systems [Ph.D]:University of Maryland.
- Piccoli, P. M., Knighton, S., Kayser, S., Ash, R., and Candela, P. A., 2015, Indium in magmatic-hydrothermal systems: understanding its behavior today to meet tomorrow's demand: *Geological Society of America Annual Meeting*, Baltimore, MD, v. 47, no. 7.
- Picot, P., and Pierrot, R., 1963, La roquesite, premier minéral d'indium: CuInS<sub>2</sub>: *Bull. Soc. Fr. Miner. Crist.*, v. 86, p. 7-14.
- Price, R. C., 1983, Geochemistry of a peraluminous granitoid suite from North-eastern Victoria, South-eastern Australia: *Geochimica et Cosmochimica Acta*, v. 47, no. 1, p. 31-42, doi:10.1016/0016-7037(83)90088-1.
- Prowatke, S., and Klemme, S., 2005, Effect of melt composition on the partitioning of trace elements between titanite and silicate melt: *Geochimica et Cosmochimica Acta*, v. 69, no. 3, p. 695-709, doi:10.1016/j.gca.2004.06.037.
- Prowatke, S., and Klemme, S., 2006, Rare earth element partitioning between titanite and silicate melts: Henry's law revisited: *Geochimica et Cosmochimica Acta*, v. 70, no. 19, p. 4997-5012, doi:10.1016/j.gca.2006.07.016.

- Rayleigh, L., 1902, LIX. On the distillation of binary mixtures: *Philosophical Magazine Series 6*, v. 4, no. 23, p. 521-537, doi:10.1080/14786440209462876.
- Reid, A. F., Li, C., and Ringwood, A. E., 1977, High-pressure silicate pyrochlores,  $\text{Sc}_2\text{Si}_2\text{O}_7$  and  $\text{In}_2\text{Si}_2\text{O}_7$ : *Journal of Solid State Chemistry*, v. 20, no. 3, p. 219-226, doi:10.1016/0022-4596(77)90157-8.
- Rudnick, R. L., and Gao, S., 2003, 3.01 - Composition of the Continental Crust A2 - Holland, Heinrich D, *in* Turekian, K. K., ed., *Treatise on Geochemistry*: Oxford, Pergamon, p. 1-64.
- Sack, R. O., and Ghiorso, M. S., 1991, An internally consistent model for the thermodynamic properties of Fe–Mg-titanomagnetite-aluminate spinels: *Contributions to Mineralogy and Petrology*, v. 106, no. 4, p. 474-505, doi:10.1007/bf00321989.
- Schwarz-Schampera, U., and Herzig, P. M., 2002, Indium: Geology, mineralogy, and economics, New York, Springer-Verlag Berlin Heidelberg 258 p., 10.1007/978-3-662-05076-7.
- Shannon, R. D. T., 1976, Revised Effective Ionic Radii and Systematic Studies of Interatomic Distances in Halides and Chalcogenides: *Acta crystallographica section A: crystal physics, diffraction, theoretical and general crystallography* v. 32, no. 5, p. 751-767.
- Shaw, D. M., 1952, The geochemistry of indium: *Geochimica et Cosmochimica Acta*, v. 2, no. 3, p. 185-206, doi:10.1016/0016-7037(52)90006-9.
- Shaw, D. M., 1957, The geochemistry of gallium, indium, thallium—a review: *Physics and Chemistry of the Earth*, v. 2, no. Supplement C, p. 164-211, doi:10.1016/0079-1946(57)90009-5.
- Sibson, R. H., 1987, Earthquake rupturing as a mineralizing agent in hydrothermal systems: *Geology*, v. 15, no. 8, p. 701-704, doi:10.1130/0091-7613(1987)15<701:eraama>2.0.co;2.
- Sillitoe, R., 1993, Epithermal models: genetic types, geometrical controls and shallow features: *Mineral Deposit Modeling: Geological Association of Canada Special Paper*, v. 40, p. 403-417.
- Sillitoe, R. H., 2010, Porphyry Copper Systems: *Economic Geology*, v. 105, no. 1, p. 3-41, doi:10.2113/gsecongeo.105.1.3.
- Simmons, S. F., White, N. C., and John, D. A., 2005, Geological characteristics of epithermal precious and base metal deposits: *Economic Geology 100th anniversary volume*, v. 29, p. 485-522.
- Simon, A. C., Frank, M. R., Pettke, T., Candela, P. A., Piccoli, P. M., and Heinrich, C. A., 2005, Gold partitioning in melt-vapor-brine systems: *Geochimica et Cosmochimica Acta*, v. 69, no. 13, p. 3321-3335, doi:10.1016/j.gca.2005.01.028.
- Simon, A. C., Pettke, T., Candela, P. A., Piccoli, P. M., and Heinrich, C. A., 2003, Experimental determination of Au solubility in rhyolite melt and magnetite: Constraints on magmatic Au budgets: *American Mineralogist*, v. 88, no. 11-12, p. 1644-1651, doi:10.2138/am-2003-11-1202.
- Simons, B., Andersen, J. C. Ø., Shail, R. K., and Jenner, F. E., 2017, Fractionation of Li, Be, Ga, Nb, Ta, In, Sn, Sb, W and Bi in the peraluminous Early Permian

- Variscan granites of the Cornubian Batholith: Precursor processes to magmatic-hydrothermal mineralisation: *Lithos*, v. 278-281, no. Supplement C, p. 491-512, doi:10.1016/j.lithos.2017.02.007.
- Sinclair, W., 1994, Tungsten-molybdenum and tin deposits at Mount Pleasant, New Brunswick, Canada: Products of ore-fluid evolution in a highly fractionated granite system: Metallogeny of collisional orogens focussed on the Erzgebirge and comparable metallogenic settings: Czech Geological Survey, Prague, p. 410-417.
- Sinclair, W., 1996, Vein-stockwork tin, tungsten, *in* Eckstrand, O. R., Sinclair, W. D., and Thorpe, R. I., eds., *Geology of Canadian Mineral Deposit Types*, Volume 8, Geological Survey of Canada, p. 409-420.
- Sinclair, W., 2007, Porphyry deposits: Mineral deposits of Canada: A synthesis of major deposit-types, district metallogeny, the evolution of geological provinces, and exploration methods: Geological Association of Canada, Mineral Deposits Division, Special Publication, v. 5, p. 223-243.
- Sinclair, W. D., Kooiman, G. J. A., Martin, D. A., and Kjarsgaard, I. M., 2006, Geology, geochemistry and mineralogy of indium resources at Mount Pleasant, New Brunswick, Canada: *Ore Geology Reviews*, v. 28, no. 1, p. 123-145, doi:10.1016/j.oregeorev.2003.03.001.
- Sinclair, W. D., Kooiman, G. J. A., and Taylor, R. P., 2007, Petrochemical discrimination of evolved granitic intrusions associated with Mount Pleasant deposits, New Brunswick, Canada by C. M. C. Inverno and R. W. Hutchinson: *Applied Earth Science*, v. 116, no. 2, p. 106-111, doi:10.1179/174327507X207447.
- Smales, A. A., Smit, J. V. R., and Irving, H., 1957, Determination of indium in rocks and minerals by radioactivation: *Analyst*, v. 82, no. 977, p. 539-549, doi:10.1039/AN9578200539.
- Stevens, L. G., and White, C. E. R., 1990, Indium and Bismuth, *ASM Handbook, Properties and Selection: Nonferrous Alloys and Special-Purpose Materials, Volume 2: Material Park, Ohio, ASM International*, p. 750-757.
- Strong, D., 1981, Ore deposit models-5. A model for granophile mineral deposits: *Geoscience Canada*, v. 8, no. 4, p. 155-161.
- Sun, S.-S., 1982, Chemical composition and origin of the earth's primitive mantle: *Geochimica et Cosmochimica Acta*, v. 46, no. 2, p. 179-192, doi:10.1016/0016-7037(82)90245-9.
- Tattitch, B. C., Candela, P. A., Piccoli, P. M., and Bodnar, R. J., 2015, Copper partitioning between felsic melt and H<sub>2</sub>O–CO<sub>2</sub> bearing saline fluids: *Geochimica et Cosmochimica Acta*, v. 148, p. 81-99, doi:10.1016/j.gca.2014.08.025.
- Taylor, J. R., and Wall, V. J., 1992, The behavior of tin in granitoid magmas: *Economic Geology*, v. 87, no. 2, p. 403-420, doi:10.2113/gsecongeo.87.2.403.
- Taylor, J. R., Wall, V. J., and Pownceby, M. I., 1992, The calibration and application of accurate redox sensors: *American Mineralogist*, v. 77, p. 284-295.
- Taylor, R., Sinclair, W., and Lutes, G., 1985, Geochemical and isotopic characterization of granites related to W-Sn-Mo mineralization in the Mount Pleasant area, New Brunswick: *Granite-related mineral deposits: Geology*,

- petrogenesis and tectonic setting. Edited by RP Taylor and DF Strong. CIM extended abstracts, p. 265-273.
- Taylor, R. P., 1992, Petrological and geochemical characteristics of the Pleasant Ridge zinnwaldite-topaz granite, southern New Brunswick, and comparisons with other topaz-bearing felsic rocks: *The Canadian Mineralogist*, v. 30, no. 3, p. 895-921.
- Thompson, J. B., 1982, Reaction space; an algebraic and geometric approach: *Reviews in Mineralogy and Geochemistry*, v. 10, no. 1, p. 33-52, doi:10.2138/rmg.1982.10.2.
- Tolcin, A. C., 2016, Indium, *in* United States Geological Survey, ed., Mineral Commodity Summaries, United States Geological Survey.
- Törnebohm, A. E., 1875, Geognostisk beskrifning öfver Persbergets grufvefält, Stockholm, Sveriges geologiska undersökning.
- Tsujimoto, Y., Fukuda, Y., Sugai, S., and Fukai, M., 1975, Tb<sup>3+</sup>-activated In<sub>2</sub>Si<sub>2</sub>O<sub>7</sub> phosphor: *Journal of Luminescence*, v. 9, no. 6, p. 475-482, doi:10.1016/0022-2313(75)90061-7.
- Tuttle, O. F., 1949, Two pressure vessels for silicate-water studies: *Geological Society of America Bulletin*, v. 60, no. 10, p. 1727-1729.
- U.S. Geological Survey, 2010, Mineral commodity summaries 2010, U.S. Geological Survey.
- U.S. Geological Survey, 2016, Mineral commodity summaries 2016, U.S. Geological Survey, 10.3133/70140094.
- U.S. Geological Survey, 2017a, Indium statistics through 2015; last modified January 19, 2017, *in* Kelly, T. D., and Matos, G.R., ed., Historical statistics for mineral and material commodities in the United States: U.S. Geological Survey Data Series 140: <http://minerals.usgs.gov/minerals/pubs/historical-statistics/> (accessed June 2017).
- U.S. Geological Survey, 2017b, Mineral commodity summaries 2017, U.S. Geological Survey, 202 p., 10.3133/70180197.
- Usuki, T., 2002, Anisotropic Fe-Mg diffusion in biotite: *American Mineralogist*, v. 87, no. 7, p. 1014.
- Valkama, M., Sundblad, K., Nygård, R., and Cook, N., 2016, Mineralogy and geochemistry of indium-bearing polymetallic veins in the Sarvlaxviken area, Lovisa, Finland: *Ore Geology Reviews*, v. 75, p. 206-219, doi:10.1016/j.oregeorev.2015.12.001.
- Wager, L. R., Smit, J. v. R., and Irving, H., 1958, Indium content of rocks and minerals from the Skaergaard intrusion, East Greenland: *Geochimica et Cosmochimica Acta*, v. 13, no. 2, p. 81-86, doi:10.1016/0016-7037(58)90041-3.
- Waldbaum, D. R., and Thompson, J. B., 1969, Mixing Properties Of Sanidine Crystalline Solutions. 4. Phase Diagrams From Equations Of State: *American Mineralogist*, v. 54, no. 9-10, p. 1274-1298.
- Watson, E. B., 1985, Henry's law behavior in simple systems and in magmas: Criteria for discerning concentration-dependent partition coefficients in nature: *Geochimica et Cosmochimica Acta*, v. 49, no. 4, p. 917-923, doi:10.1016/0016-7037(85)90307-2.

- Webster, J. D., 1990, Partitioning of F between H<sub>2</sub>O and CO<sub>2</sub> fluids and topaz rhyolite melt: *Contributions to Mineralogy and Petrology*, v. 104, no. 4, p. 424-438, doi:10.1007/bf01575620.
- Webster, J. D., 2004, The exsolution of magmatic hydrosaline chloride liquids: *Chemical Geology*, v. 210, no. 1-4, p. 33-48, doi:10.1016/j.chemgeo.2004.06.003.
- Webster, J. D., and Holloway, J. R., 1988, Experimental constraints on the partitioning of Cl between topaz rhyolite melt and H<sub>2</sub>O and H<sub>2</sub>O + CO<sub>2</sub> fluids: New implications for granitic differentiation and ore deposition: *Geochimica et Cosmochimica Acta*, v. 52, no. 8, p. 2091-2105, doi:10.1016/0016-7037(88)90189-5.
- Webster, J. D., Holloway, J. R., and Hervig, R. L., 1987, Phase equilibria of a Be, U and F-enriched vitrophyre from Spor Mountain, Utah: *Geochimica et Cosmochimica Acta*, v. 51, no. 3, p. 389-402, doi:10.1016/0016-7037(87)90057-3.
- Webster, J. D., Kinzler, R. J., and Mathez, E. A., 1999, Chloride and water solubility in basalt and andesite melts and implications for magmatic degassing: *Geochimica et Cosmochimica Acta*, v. 63, no. 5, p. 729-738, doi:10.1016/S0016-7037(99)00043-5.
- Westra, G., and Keith, S. B., 1981, Classification and genesis of stockwork molybdenum deposits: *Economic Geology*, v. 76, no. 4, p. 844-873, doi:10.2113/gsecongeo.76.4.844.
- Westrenen, W. V., Blundy, J., and Wood, B., 1999, Crystal-chemical controls on trace element partitioning between garnet and anhydrous silicate melt: *American Mineralogist*, v. 84, no. 5-6, p. 838-847.
- Whalen, J. B., Currie, K. L., and Chappell, B. W., 1987, A-type granites: geochemical characteristics, discrimination and petrogenesis: *Contributions to Mineralogy and Petrology*, v. 95, no. 4, p. 407-419, doi:10.1007/bf00402202.
- White, W., Bookstrom, A., Kamilli, R., Ganster, M., Smith, R., Ranta, D., and Steininger, R., 1981, Character and origin of Climax-type molybdenum deposits: *Economic Geology*, v. 75, p. 270-316.
- Wones, D. R., 1972, Stability of biotite—a reply: *American Mineralogist*, v. 57, no. 1-2, p. 316-317.
- Wones, D. R., and Eugster, H. P., 1965, Stability of biotite—experiment theory and application: *American Mineralogist*, v. 50, no. 9, p. 1228-1272.
- Yajima, J., and Ohta, E., 1979, Two-stage mineralization and formation process of the Toyoha deposits: *Mining Geology*, v. 29, no. 157, p. 291-306.
- Yamashita, S., 1999, Experimental Study of the Effect of Temperature on Water Solubility in Natural Rhyolite Melt to 100 MPa: *Journal of Petrology*, v. 40, no. 10, p. 1497-1507, doi:10.1093/etroj/40.10.1497.
- Yang, X.-M., and Lentz, D. R., 2005, Chemical composition of rock-forming minerals in gold-related granitoid intrusions, southwestern New Brunswick, Canada: implications for crystallization conditions, volatile exsolution, and fluorine-chlorine activity: *Contributions to Mineralogy and Petrology*, v. 150, no. 3, p. 287-305, doi:10.1007/s00410-005-0018-7.

- Zajacz, Z., Seo, J. H., Candela, P. A., Piccoli, P. M., and Tossell, J. A., 2011, The solubility of copper in high-temperature magmatic vapors: A quest for the significance of various chloride and sulfide complexes: *Geochimica et Cosmochimica Acta*, v. 75, no. 10, p. 2811-2827, doi:10.1016/j.gca.2011.02.029.
- Zhang, Q., Zhu, X., He, Y., Jiang, J., and Wang, D., 2006, Indium Enrichment in the Meng'entaolegai Ag-Pb-Zn Deposit, Inner Mongolia, China: *Resource Geology*, v. 56, no. 3, p. 337-346, doi:10.1111/j.1751-3928.2006.tb00287.x.